2015

Spatiotemporally Periodic Driven System with Long-Range Interactions

Owen Dale Myers
University of Vermont

Spatiotemporally Periodic Driven System with Long-Range Interactions

A Dissertation Presented

by

Owen Myers

to

The Faculty of the Graduate College

of

The University of Vermont

In Partial Fullfillment of the Requirements
for the Degree of Doctor of Philosophy
Specializing in Materials Science

May, 2015

Defense Date: March 27, 2015
Dissertation Examination Committee:

Junru Wu, Ph.D., Advisor
Christopher M. Danforth, Ph.D., Chairperson
Jeffrey S. Marshall, Ph.D.
Dennis P. Clougherty Ph.D.
Cynthia J. Forehand, Ph.D., Dean of the Graduate College

Abstract

It is well known that some driven systems undergo transitions when a system parameter is changed adiabatically around a critical value. This transition can be the result of a fundamental change in the structure of the phase space, called a bifurcation. Most of these transitions are well classified in the theory of bifurcations. Among the driven systems, spatiotemporally periodic (STP) potentials are noteworthy due to the intimate coupling between their time and spatial components. A paradigmatic example of such a system is the Kapitza pendulum, which is a pendulum with an oscillating suspension point. The Kapitza pendulum has the strange property that it will stand stably in the inverted position for certain driving frequencies and amplitudes. A particularly interesting and useful STP system is an array of parallel electrodes driven with an AC electrical potential such that adjacent electrodes are 180 degrees out of phase. Such an electrode array embedded in a surface is called an Electric Curtain (EC). As we will show, by using two ECs and a quadrupole trap it is posible to produce an electric potential simular in form to that of the Kapitza pendulum.

Here I will present the results of four related pieces of work, each focused on understanding the behaviors STP systems, long-range interacting particles, and long-range interacting particles in STP systems. I will begin with a discussion on the experimental results of the EC as applied to the cleaning of solar panels in extraterrestrial environments, and as a way to produce a novel one-dimensional multiparticle STP potential. Then I will present a numerical investigation and dynamical systems analysis of the dynamics that may be possible in an EC. Moving to a simpler model in order to explore the rudimentary physics of coulomb interactions in a STP potential, I will show that the tools of statistical mechanics may be important to the study of such systems to understand transitions that fall outside of bifurcation theory. Though the Coulomb and, similarly, gravitational interactions of particles are prevalent in nature, these long-range interactions are not well understood from a statistical mechanics perspective because they are not extensive or additive. Finally, I will present a simple model for understanding long-range interacting pendula, finding interesting non-equilibrium behavior of the pendula angles. Namely, that a quasistationary clustered state can exist when the angles are initially ordered by their index.

Acknowledgements

This work was partially funded by NASA Space Grant Consortium, NNX10AK67H and NNX08AZ07A. I would like to acknowledge the Vermont Advanced Computing Core which is supported by NASA (NNX 06AC88G), at the University of Vermont for providing High Performance Computing resources that have contributed to the research results reported within this thesis.

Table of Contents

List of Figures

List of Tables

Chapter 1

Motivation

1.1 Spatiotemporally Periodic Driven Systems

Studies of nonlinear periodically driven systems are important to understanding the fundamental physics of many useful and interesting phenomena in applications of lasers (1), driven ratchets (2), hydrophilic particles on the surface of water waves (3; 4; 5), driven Josephson junctions (6), and a variety of other interesting systems. At a more fundamental level, driving a system can change its properties through effects like dynamical stabilization, e.g. high frequency electromagnetic driving increasing the stability of electron orbitals (7; 8; 9; 10). If bodies moving in periodically-driven systems are allowed to interact, they can display a wealth of interesting physical phenomena associated with complex systems (11; 12; 13). Studies of the interaction among oscillators, particles, nodes (in network), etc., in periodic systems, and of how the behaviors of such systems collectively react, can also be valuable in a variety of

fields from neuroscience (14) to driven Josephson junction arrays (15), to increasing the critical temperature of superconductors (16).

In this work we are interested in forms of driving that depend both on the time and the location of particles in the system, specifically cases where the spatial and temporal dependence of the driving is periodic. We classify forms of driving that are periodic in space and time as "spatiotemporally periodic" (STP), though this type of driving may also be referred to as "Kapitza like", or the Kapitza class of driving (17). STP driven systems are sometimes also categorized as parametrically driven, though this is a nonspecific classification insofar as the spatial periodicity. We believe the distinction is necessary because STP driven systems have several interesting features that are not necessarily intrinsic to the more general class of parametrically driven systems. Primarily, in multiple particle systems, when a spatially periodic potential is present the dynamics will depend heavily on the concentration of the particles, as we will show in chapter 5. The concentration referred to here is the number of particles per spatial period of the potential.

The particle interactions in which we are interested are long-range. In the most conventional sense, long-range interactions are ones that decay as $1/r^{\alpha}$, where $\alpha \leq d$, d being the dimension of the space in which the system is embedded. When considering long-range driven systems in a general context, it is possible to imagine interactions that depend on position in a more exotic way than $1/r^{\alpha}$; however, these more exotic cases are beyond the scope of this work. For some time, the primary motivation behind the study of long-range interactions was to understand galaxies, galaxy clusters and the general thermodynamic properties of self-gravitating systems. Aside from mean field models, interest has further built since the observation of mod-

ified scattering lengths in Bose-Einstein Condensates (BEC) through the use of Feshbach resonances (18). Using Feshbach resonances, a BEC can be made to be almost non-interacting by tuning the scattering length to zero. One could even tune the scattering length to a negative value, making the BEC collapse. More recently, O'dell et al. (19) has shown that it may be possible to produce an attractive $1/r$ potential between atoms in a BEC by applying an "extremely off resonant" electromagnetic field. This has opened the possibility of creating table-top experiments which physically model aspects of cosmological behavior on a laboratory scale, as well as the possible development of entirely new dynamics in BEC. Also, these studies suggest that a particularly interesting playground for STP driven long-range interacting systems is going to be cold atoms in optical lattices.

We illustrate the possible unique behaviors of a STP driven system with long-range interactions using a simple example. Imagine a two-dimensional static egg crate potential with two particles per valley of the potential, i.e. a concentration of two. If particles have kinetic energies that are small compared to the height of the periodic potential and their interactions are attractive, with interaction strengths that are also small compared to the height of the periodic potential, then they will likely settle into paired orbits in the valleys of the egg crate. Now, imagine slowly inverting the egg crate potential so that the peaks become valleys and the valleys become peaks. If the paired particle orbits are somewhat symmetric about the lowest points in the valleys, then as the potential inverts they might break their pairings and form new pairs with particles previously located one spatial period away. This cycle can continue to repeat itself as the egg crate potential periodically inverts itself. Depending on the frequency of the egg crate inversions, the particle pairings could be random or occur in a regular

and predictable way. The continuous re-paring of particles occurs because of both the periodic time dependence and the spatial periodicity of the potential. By modulating the spacial periodicity one can tune the concentration, and by modulating the driving frequency one can tune the duration and regularity interacting groups of particles. If the particles are long-range interacting one might find that they couple to collective oscillations is the system leading to interesting nonequilibrium behaviors.

Let's consider in more detail long-range interacting particles in our toy example but choose the physical realization of the system to be an optical lattice of cold atoms. In chapter 2, section 3, we discuss the interesting properties of long-range interacting systems in more detail, but for now let us simply state that these interactions can produce what is known as a "core-halo" distribution in phase space. The core continues to cool as the halo becomes hotter, sapping energy from the core by coupling to its collective oscillations. By tuning the scattering of a BEC to produce effective long-range interactions using the application off resonant fields (19), we speculate that evaporative cooling could be highly accelerated.

It is possible to go into great depth about the history of driven systems since they span a variety of fields, like the ones mentioned in the first paragraph. As the focus of this work is only on a particular type of driving, we will share a brief overview of the nucleation of interest in STP driven systems. We mentioned that STP driven systems are also classified as the Kapitza class of driving. Let us now introduce the Kapitza pendulum and its significance to this work. In 1951 Kapitza published two papers (20; 21) on a planar pendulum with an oscillating suspension point. The most interesting feature of this simple system is that under certain conditions, the pendulum stands stably in the inverted position. The change in stability of the

inverted position through the oscillation of the suspension point is an example of dynamic stabilization, in which an inherently unstable system or unstable point in a system can be stabilized by periodic forcing. The Kapitza pendulum will play a central role in the following work since it is the most paradigmatic STP system. Dynamical stabilization was known about on some level since we discovered that flailing your arms can help you keep your balance, but the Kapitza pendulum was a notable development in the fascination with dynamical stabilization because of its simplicity and strangeness.

It is well known that a static electric potential can not contain even a single ion, but a time dependent field can do this through dynamical stabilization. It was only two years after Kapitza's publications that the quadrupole ion (Paul) trap was patented (22). This is not to say that Kapitza's papers directly motivated the Paul trap, as this was not the case. The quadrupole trap is an arguably more important application of dynamic stabilization but it does not contain the spacial periodicity we have chosen to focused on. We will discuss both the introductory theory of the Kapitza pendulum and the quadrupole trap in chapter 2. In chapter 3 we will show how a quadrupol trap with a periodic array of electrodes on either side can be used to create a longitudinal standing wave along the axis of the trap, a system which *is* STP.

An important system to the study of classical long-range interacting particles under STP driving involves charged particles driven by a device known as the electric curtain (EC). The electric curtain will be introduced in more detail in chapter 2, section 2.4, but in its simplest form it is an array of electrodes each being driven by an AC potential. The particles interact through their charges which, to first order,

is the Coulomb interaction; a long-range interaction. Due to the simplicity of the EC and the numerous possible configurations and dynamics, it has been proposed as a method of particle control and mitigation in a variety of applications, especially in cleaning applications, where a particles charge can make for a large electrostatic sticking force. The larger the charge on a particle, the larger the interaction with an EC, making it a convenient candidate for cleaning charged particles from surfaces (23).

1.2 Objectives

Using the above brief motivation, we can outline the main objectives of our work on STP driven systems and long-range interactions. To attack such a large problem, we strive to understand it from several different fronts. First, we will present an experimental study on the dynamics and statistical properties of charged particles in an EC field. This work was originally motivated by NASA to improve the EC as a technology for cleaning solar panels in extraterrestrial environments. Since the work done under this original motivation we have also found its value as a tunable source of STP driving and in helping to understand the general class of STP systems. Second, we present a numerical study of the single particle dynamics in a model EC field. The purpose of this numerical investigation was to fill in some of the gaps in understanding the dynamics that we found experimentally. The numerical study also served as a way to quickly search for new dynamical features of particles driven by an EC. Third, we present a numerical study of the multiple particle dynamics and kinetic energy fluctuations in an exemplary STP field. This numerical study is the heart of

this work as it is based on one of the simplest and most fundamental long-range interacting STP models. Fourth, we develop a deeper understanding of long-range interactions and the behaviors of long-range interacting pedulua. In this body of the work, we do not consider any driving but simply push to broaden comprehension of long-range interactions for a relevant system; multiple pendula with interacting bobs, which if driven correctly would be multiple interacting Kapitza pendula. We analytically examine the long-range interacting pendula in equilibrium by solving for the canonical partition function, and study the nonequilibrium behaviors numerically.

Chapter 2

Review of Pertinent Systems and Literature

2.1 Important Models

2.1.1 The Parametrically Driven Harmonic Oscillator

The motion of a single particle in a STP potential, e.g. the motion of the Kapitza pendulum, may be solved analytically around certain angles. In the case of the Kapitza pendulum the most obvious approximation would be the small angle approximation. For a one-dimensional STP potential, with spacial coordinate (angle) x, if we work at positions where the potential can be expressed as a harmonic oscillator potential then the equations of motion can be solved using Floquet theory (24). This type of driven harmonic oscillator is known as the parametric harmonic oscillator, and it is a

prevalent model in the literature of driven systems. The Hill equation is the equaiton of motion for the parametric harmonic oscillator with arbitrary driving, and can be written as $\ddot{x} + g(t)x = 0$, where $g(t)$ is periodic in t. If $g(t) = \cos(\omega t)$, the Hill equation reduces to the Mathieu equation (25). Both the Hill and Mathieu equations have been studied extensively due to their interesting properties, their many applications to different systems, and straight-forward analytical treatment. Their solutions apply to the approximation of the Kapitza pendulum, the quantum pendulum (26), ion traps (27), and oscillations of a floating mass in a liquid (28). Through a simple mapping which we will discuss in chapter 4 subsection 4.4.1, one can even include dissipation in the Mathieu equation.

The solutions to the parametrically driven harmonic oscillator were originally found in an altogether different physical context. In 1868 Mathieu worked to solve for the leading terms in the series solution of the vibration modes of an elliptically vibrating drum head (29). To do this he developed the special functions now known as the elliptic cosine and sine functions. By taking a linear combination of the elliptic cosine and sine functions, the vibrational modes of an elliptical membrane can be described. A good discussion of the solutions to the Mathieu equation is by Gutierrez et al. (30), who also show nice graphical representations of the solutions.

The canonical form of the Mathieu equation is

$$\frac{d^2x}{dt^2} + [a - 2q\cos(2t)]x = 0. \tag{2.1}$$

Mclachlan (25) has written a book on the Mathieu equation, the various forms of its solutions, and a variety of its applications. One particularly convenient form of the

solution discussed by Mclachlan (25) is

$$x(t) = Ae^{\mu t} \sum_{n=-\infty}^{\infty} C_{2n} e^{i2nt} + Be^{-\mu t} \sum_{n=-\infty}^{\infty} C_{2n} e^{-i2nt}, \tag{2.2}$$

where A and B are constants that are chosen to satisfy the appropriate boundary conditions and μ can be any complex number. The μ is sometimes referred to as the characteristic exponent since it determines the stability of $x(t)$. Stability is defined in the following way: $x(t)$ is unstable if

$$\lim_{t\to\infty} x(t) = \pm\infty, \tag{2.3}$$

and stable if $x(t)$ remains bounded for all t. The term bounded does not necessarily imply periodic. If a solution is periodic it is a special case of the stable solution and is sometimes called "neutral".

Let's investigate a couple of particular cases for the solutions shown in Eq. 2.2 for different μ. If μ is real and positive (negative) then the first (second) term in Eq. 2.2 goes to ∞ as $t \to \infty$. Clearly μ must be imaginary if we are looking for stable solutions. Let's say $\mu = i\beta$, where β is real. We can choose to write β as a fraction of two numbers, call them p and s, that are prime to each other (sharing no common factors besides 1), so $\beta = p/s$. If p/s is a rational fraction then β is a rational number and each term on the RHS of Eq. 2.2 is periodic with period $2s\pi$. In the irrational case, the solution is not periodic but it is bounded.

After setting $\mu = i\beta$ we can take Eq. 2.2 and insert it back into the Mathieu equation (Eq. 2.1) in order to find a recursion relation between the coefficients C_{2n},

C_{2n+2}, and C_{2n-2}. If we define

$$D_{2n} \equiv [a - (2n + \beta)^2]/q, \tag{2.4}$$

then we can write the recursion relation as

$$C_{2n+2} - D_{2n}C_{2n} + C_{2n-2} = 0. \tag{2.5}$$

The recursion relation is useful since it only takes a little algebra to write any C_{2n} as a continued fraction of D_{2n}.

$$C_{2n+2} = \cfrac{C_{2n}}{D_{2n} - \cfrac{1}{D_{2n+2} - \cfrac{1}{\cdots}}}, \tag{2.6}$$

and

$$C_{2n} = \cfrac{C_{2n-2}}{D_{2n} - \cfrac{1}{D_{2n-2} - \cfrac{1}{\cdots}}}. \tag{2.7}$$

With this expression we can find the coefficients to arbitrary precision by truncating the continued fraction when the desired precision is reached. With boundary conditions and the above expressions of the coefficients C_{2n}, one obtains the solution to the Mathieu equation (to arbitrary precision).

Some applications of the Mathieu equation are also covered by Mclachlan (25),

but another more concise review of the Mathieu equation, its solutions, and applications is given by Lawrenc Ruby (28). Since driven systems exhibit the property of dynamical stabilization, it is not surprising that one of the primary applications of driven systems is in the trapping of ions which cannot be contained in a static field in three dimensions. The lack of a static minima in three dimensions is easy to see if we define a three dimensional static electric potential

$$\Phi(x, y, z) = \frac{1}{2}(ax^2 + by^2 + cz^2), \tag{2.8}$$

and using the Laplace equation $\nabla^2\Phi = 0$ show that $a + b + c = 0$. Clearly no minimum in three dimensions is possible because a, b, c cannot all have the same sign and satisfy the Laplace equation. By introducing time dependence to the potential, we can produce an effective three-dimensional minima at the $x = 0$, $y = 0$, $z = 0$ point. We will discuss a detailed version of dynamic stabilization which creates an effective potential minima for the case of the Kapitza pendulum.

2.1.2 The Kapitza Pendulum

Due to the importance of the Kapitza Pendulum to this work, we will now describe it and dynamical stabilization in more detail. The Kapitza pendulum is one with a vertically oscillating suspension point, oscillating parallel to the force of gravity. The gravitational field is perpendicular to the horizontal axis. We will call the horizontal axis the x-axis, and the vertical axes the y-axis as shown in Fig. 2.1. The Lagrangian

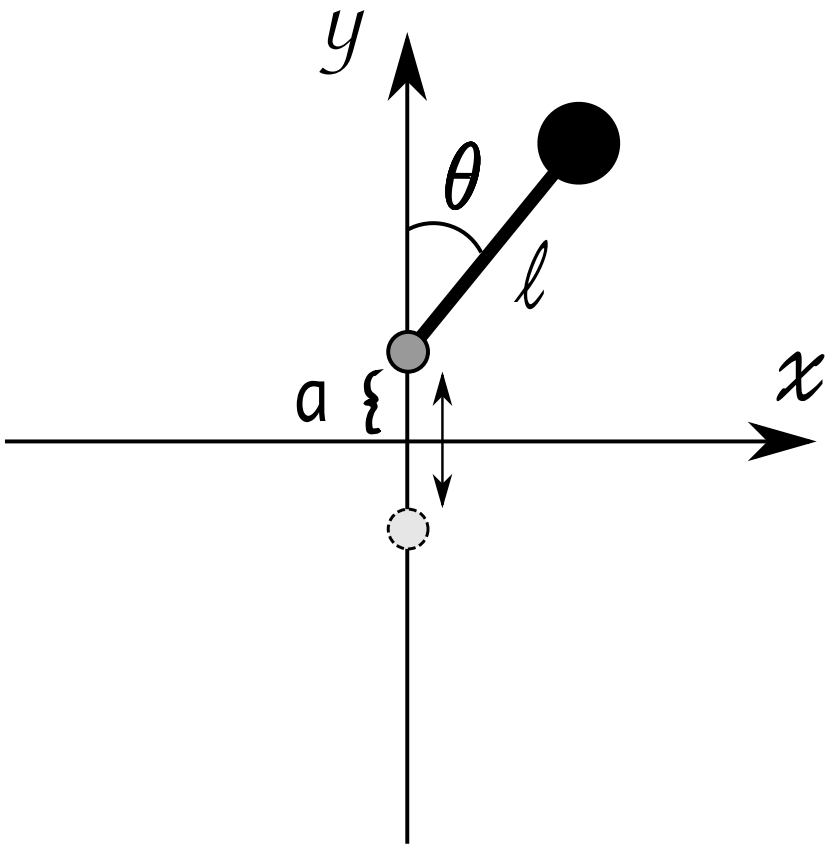

Figure 2.1: A cartoon of the Kapitza pendulum. The amplitude of the oscillation of the suspension point is a. The length of the pendulum is ℓ. The angle from vertical is θ

of the system can be written as

$$\mathscr{L} = T - U = \frac{m}{2}\left(\dot{x}^2 + \dot{y}^2\right) - mgy. \tag{2.9}$$

We can replace x and y with the following relationships

$$x = \ell \sin\theta \tag{2.10}$$

$$y = a\sin\omega t - \ell\cos\theta, \tag{2.11}$$

resulting in

$$\mathscr{L} = \frac{m}{2}\left(\ell^2\dot{\theta}^2\cos^2\theta + a^2\omega^2\cos^2(\omega t) + \ell^2\dot{\theta^2}\sin^2\theta - 2a\ell\omega\dot{\theta}\cos\omega t\sin\theta\right) - mg(a\sin\omega t - \ell\cos\theta). \tag{2.12}$$

Collecting the squared cosine and sine terms we get

$$\mathscr{L} = \frac{m}{2}\ell^2\dot{\theta}^2 + \frac{m}{2}a^2\omega^2\cos^2(\omega t) - ma\ell\omega\dot{\theta}\cos\omega t\sin\theta - mga\sin(\omega t) + mg\ell\cos\theta, \tag{2.13}$$

but we can throw away the terms having no θ or $\dot{\theta}$ dependence since they do not appear in the equations of motion. We are left with

$$\mathscr{L} = \frac{m}{2}\ell^2\dot{\theta}^2 - ma\ell\omega\dot{\theta}\cos(\omega t)\sin\theta + mg\ell\cos\theta. \tag{2.14}$$

The equations of motion follow from the Euler-Lagrange equation,

$$m\ell^2\ddot{\theta} = ma\ell\omega^2\cos\omega t\sin\theta - \ell mg\sin\theta. \tag{2.15}$$

It is easiest to jump to the Hamiltonian by imagining a stationary pendulum, about which a rotating field produces the force that generates the equations of motion shown in Eq. 2.15. The potential

$$V = m\ell a\omega^2 \cos\omega t \cos\theta - mg\ell\cos\theta \tag{2.16}$$

produces the same equations of motion and allows us to write the Hamiltonian in the simplest possible form with the kinetic energy term $p^2/2m\ell^2$ plus V. The Hamiltonian is

$$H = \frac{p^2}{2m\ell^2} + m\ell a\omega^2 \cos\omega t \cos\theta - mg\ell\cos\theta. \tag{2.17}$$

Now that we have a nice expression for the Hamiltonian of the Kapitza pendulum, we are going to use a powerful tool known as the Magnus expansion to show that the pendulum becomes stable in the inverted position. Originally, the Magnus Expansion was developed as a way to approximate a non-autonomous linear first-order differential equation, but it is now often used in a clever way to produce the effective Hamiltonian of a driven system. The usefulness of the expansion resides in several different properties. At the most superficial level, it is useful because each order of the expansion often exhibits some qualitative behavior of the actual system. For example, the stabilization of the inverted position of the Kapitza pendulum is evident in the form of approximated Hamiltonian. At a deeper level the approximation of any operator found through the Magnus expansion will belong to the same Lie algebra of the original operator at any order of the expansion. For a detailed review of the Magnus expansion and confrontation of some of the known issues surrounding it, including issues of existence and convergence, see Blanes et al. (31).

The use of the Magnus expansion is most convenient in the quantum language. Imagine preparing the system in some initial state $|\psi\rangle$ which evolves under the periodic Hamiltonian of interest, having period T. This evolution from some time t_0 to some later time t can be achieved by $U(t,t_0)|\psi\rangle$ where $U(t,t_0)$ is the time dependent evolution operator

$$U(t,t_0) = \mathcal{T} e^{\frac{i}{\hbar}\int_{t_0}^{t} dt' H(t')}, \tag{2.18}$$

and $\mathcal{T}$ is the time ordering operator. To evolve by one period, $|\psi(nT)\rangle = U(T)^n|\psi_0\rangle$, we can write $U(t,t_0)$ as

$$U(T) = \mathcal{T} e^{\frac{i}{\hbar}\int_{0}^{T} dt H(t)}, \tag{2.19}$$

so that $U(T)$ evolves the system by one period. Since U is known to be unitary it can be written as the exponential of a Hermitian operator which we will call H_{eff}, or the effective Hamiltonian. In this way we write

$$U(T) = e^{-iH_{eff}T/\hbar}. \tag{2.20}$$

We can now solve

$$\mathcal{T} e^{-\frac{i}{\hbar}\int_{0}^{T} H(t)dt} = e^{iH_{eff}T/\hbar} \tag{2.21}$$

for H_{eff} resulting in

$$H_{eff} = \frac{i\hbar}{T} \log\left(\mathcal{T} e^{-\frac{i}{\hbar}\int_{0}^{T} H(t)dt}\right). \tag{2.22}$$

For most Hamiltonians of interest the above expression for H_{eff} cannot be exactly solved, which is why we have called the LHS an effective Hamiltonian. The Magnus expansion is the short period (high temperature) expansion of the RHS of Eq. 2.22. We will omit the details of finding the standard expression of the expansion and

simply state the first three terms, which will suffice for our discussion.

$$H^1_{eff} = \frac{1}{T}\int_0^T dt H(t) \tag{2.23}$$

$$\tag{2.24}$$

$$H^2_{eff} = \frac{1}{2T(i\hbar)}\int_0^T dt_1 \int_0^{t_1} dt_2 \left[H(t_1), H(t_2)\right] \tag{2.25}$$

$$\tag{2.26}$$

$$H^3_{eff} = \frac{1}{6T(i\hbar)^2}\int_0^T dt_1 \int_0^{t_1} dt_2 \int_0^{t_2} dt_3 \left(\left[H(t_1), \left[H(t_2), H(t_3)\right]\right] + \left[H(t_3), \left[H(t_2), H(t_1)\right]\right]\right). \tag{2.27}$$

Evaluating the commutators and the integrals results in

$$H^1_{eff} = \frac{p^2}{2m} - m\omega_0^2 \cos\theta \tag{2.28}$$

$$H^2_{eff} = 0 \tag{2.29}$$

$$H^3_{eff} = \frac{a}{4m\ell}\left(p^2\cos\theta + 2p\cos\theta p + \cos\theta p^2\right) + \left(\frac{ma^2\omega^2}{4\ell^2} - \frac{a\omega_0}{\ell}\sin^2\theta\right). \tag{2.30}$$

Up to third-order the classical solution can be found by simply replacing the operators with the classical variables (32). This is not generally true, but it can be shown that the quantum corrections to replacing the quantum commutators with the Poisson brackets are small when considering this third order Magnus expansion. Proving that the quantum corrections are small is done by using the Moyal Bracket of Weyl symbols of the relevant operators. For a discussion on the details of the phase space representation of quantum dynamics see Polkovnikov (33) and D'Alessio et al. Appendix A. (32).

Now we can consider the classical effective Hamiltonian

$$H_{eff} = \frac{p^2}{2m} - m\omega_0^2 \cos\theta + \frac{a}{m\ell}\left(p^2 \cos\theta\right) + \left(\frac{ma^2\omega^2}{4\ell^2} - \frac{a\omega_0}{\ell}\sin^2\theta\right). \tag{2.31}$$

Looking at the terms that only depend on θ, we can extract an effective external potential

$$V_{eff\ ext} = m\left(\left(\frac{a^2\omega^2}{4\ell^2} - \frac{a\omega_0^2}{\ell}\right)\sin^2\theta - \omega_0^2\cos\theta\right). \tag{2.32}$$

Differentiating twice, we find that the condition for a minima to be located at $\theta = \pi$ is

$$2\left(\frac{a^2\omega^2}{4\ell^2} - \frac{a\omega_0^2}{\ell}\right) > \omega_0^2, \tag{2.33}$$

which is the condition for stability of the pendulum in the inverted position.

We have now a clear mathematical picture of how the Kapitza pendulum can stand in the inverted position. With fast driving one can satisfy the condition in Eq. 2.33 (large ω), which is the same condition for the use of the Magnus expansion to begin with. Driving the pivot of the pendulum creates an effective potential which changes depending on the parameters of the system. One other way that the stability of the inverted position can be shown is by separating out the fast and slow degrees of freedom and making the assumption that the fast degrees of freedom are irrelevant. In some sense the Magnus Expansion can give you the effective Hamiltonian without having to debate the importance of the fast or slow degrees of freedom. This particular tuning of the effective potential is know as dynamic stabilization.

2.1.3 The Kicked Rotator and the Standard Map

Here we introduce an important model known as the kicked rotor model. This model is of significance in physics for many reasons, one of these reasons being that the kicked rotator is one of the simplest Hamiltonians that exhibits chaotic dynamics. Arguably, the most important feature of this model is that it is integrable, the solution is the well known (Chirikov) standard map. The standard map approximately describes the dynamics of a system near a sepratrix of a nonlinear resonance, an incredibly prevalent feature in many driven nonlinear systems.

The Hamiltonian of the kicked rotor can be written as

$$H = \frac{L^2}{2I} - K\cos(\theta)\delta(t - nT) \tag{2.34}$$

where L is the angular momentum of the rotor, I is its moment of inertia, K is the kicking amplitude, θ its angular position, T is the period of the kicking, and n is an integer. We can find the equations of motion by using Hamilton's equations, resulting in

$$\dot{L} = -\frac{\partial H}{\partial \theta} = p/m, \tag{2.35}$$

and

$$\dot{\theta} = \frac{\partial H}{\partial L} = -K\sin(\theta)\delta(t - nT). \tag{2.36}$$

These are integrable over the periods of time between kicks and therefore a simple recursion relation can describe the dynamics. This recursion relation is known as a discrete map, and this particular one is known as the standard (Chirikov) map. The

recursion relations are

$$\theta_{n+1} = \theta_n + TL_{n+1} \tag{2.37}$$

$$L_{n+1} = L_n - K\sin(\theta_n) \tag{2.38}$$

Which give us the angles and positions at any point in time because between kicks we know that $\theta_n(t) = \theta_n + (t \mod (T))L_n/m$.

In order to develop our intuitive understanding of the standard map (its behavior may not be completely transparent in the form of the recursion relation) we will look at the model under a couple of limits. We follow the pedagogical discussion of the standard map by Anatoli Polkovnikov in his notes (34). First we choose a unit mass and period ($m = T = 1$) through the rescaling of K and time. Second we choose to look in the limit of $K \ll 1$ and $p_0 \ll 1$, where p_0 is the initial momentum. This allows us to take the continuum limit with respect to the period. Now we have the approximate relationships

$$\frac{\partial\theta}{\partial n} \approx p, \ \frac{\partial p}{\partial n} \approx -K\sin(\theta), \tag{2.39}$$

or in the form of a second order differential equation

$$\frac{\partial^2\theta}{\partial n^2} \approx K\sin\theta. \tag{2.40}$$

We see that Eq. 2.40 is just the equation of motion for a pendulum.

Just as in the case of fast driving for the Kapitza pendulum, we find that under certain limits of the system parameters the equations of motion can take on a new form. Part of the point in discussing the details of the kicked rotor and the Kapitza

pendulum is that the STP driving can be used to renormalise the potential of a given system. One can imagine the usefulness of being able to tune a system's properties simply by adjusting the frequency or amplitude of the driving. These models are important to a decent foundation in understanding STP systems.

2.2 Nonlinear Dynamics of Driven Systems

One might begin discussion of nonlinear dynamics at many different points in time, although a convenient starting point might be Newton's dynamics of celestial bodies, coinciding as it does with the beginning of calculus, and therefore is one of the first applications of the differential equations that we use to mathematically represent many physical systems. From this foundation, the understanding of nonlinear dynamics grew significantly out of Poincaré's work in the qualitative, aka geometric, understanding of differential equations. This is not only a wonderful way to understand the possible behaviors of a nonlinear differential equation, but it is pedagogically valuable due to its simple elegance. Poincaré's work also started one of the most important and fundamental ideas in nonlinear systems, which is a way to classify them via the topological structure of their phase space (35)

If we are interested in time-dependent systems, we can restrict ourselves to solving *sets* of first-order ordinary differential equations. In general, one can always express a system of differential equations of arbitrary order with a set of first-order differential equations. We can understand the flow of any first-order equation $\dot{x} = f(x)$, by using Poincaré's qualitative method. This method consists of sketching $\dot{x} = f(x)$ and using

the sketch to draw a vector field, where the vector field describes the flow on the x axis. Let's take a simple example to understand this concept in more detail. Consider the function $f(x) = x^2 - 1$, for which we can plot the velocity $\dot{x}$ as a function of x as shown in Fig. 2.2. Fixed points of a flow along x will be the solutions to $f(x) = 0$,

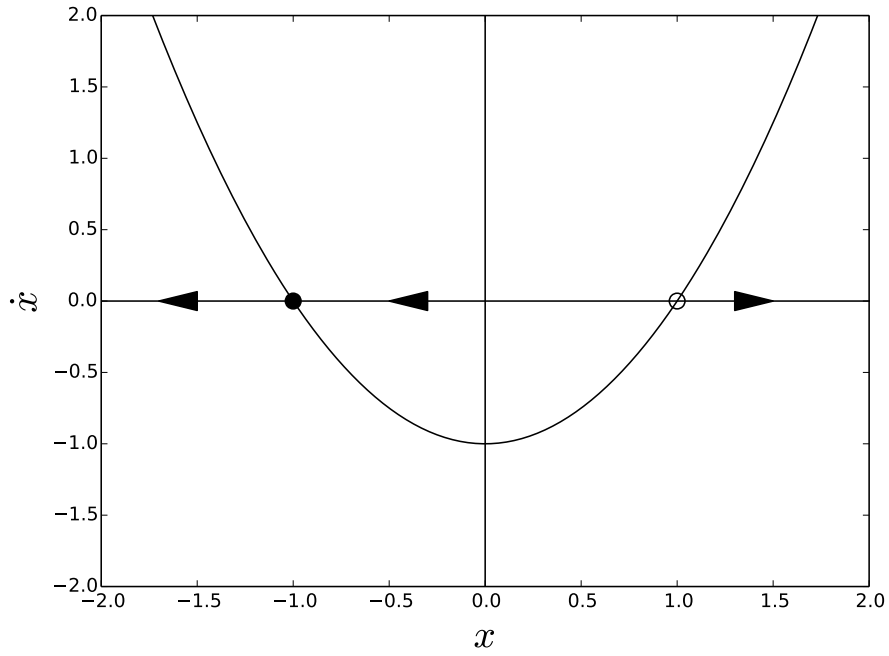

Figure 2.2: A phase portrait of $\dot{x} = x^2 - 1$. The filled circle represents a stable fixed point and the unfilled circle represents the unstable fixed point.

call them x_{fp1} and x_{fp2}. The stability of the fixed point will be given by $f'(x)|_{x_{fpn}}$, x_{fpn} being the n^{th} fixed point.

2.2.1 Bifurcations

By including a little more flexibility in our example function $f(x)$, we can change the phase portrait. Let's make the height of our parabola adjustable by including a

parameter h, so $f(x) = x^2 - h$. When $h = 1$, we have the phase portrait shown in Fig. 2.2. Let's say now that we set $h < 0$, so that now there are no more fixed points and the flow along x is fundamentally different. If we tune h from a negative value, to a positive value we cross between these two regimes. The fundamental transition between the two types of flows is known as a bifurcation, and this particular type of bifurcation is called a saddle node bifurcation, which can be thought of as two fixed points annihilating one another (h going from negative to positive) or as two fixed points being spontaneously created about the origin (h going from positive to negative). This is also sometimes called the blue sky bifurcation because the fixed points seem to appear out of nowhere.

In our simple example, no periodic trajectories are possible. There is clearly no room for them in the phase space. They either zoom off to infinity or sink into an attractive fixed point. We need to move to a higher dimensional phase space to see periodic and chaotic trajectories. As we saw in the one dimensional case $f'(x = x_{fpn})$ told us the stability of the fixed point. We can generalize this to higher dimensions by taking the Jacobian of a system of n equations

$$\dot{x}_1 = f_1(x_1, x_2, \ldots, x_n) \tag{2.41}$$

$$\dot{x}_2 = f_2(x_1, x_2, \ldots, x_n) \tag{2.42}$$

$$\vdots \tag{2.43}$$

$$\dot{x}_n = f_n(x_1, x_2, \ldots, x_n), \tag{2.44}$$

where each $f_n(x_1, x_2, \ldots, x_n)$ is an arbitrary function, resulting in

$$\boldsymbol{J} = \begin{pmatrix} \frac{\partial f_1}{\partial x_1} & \frac{\partial f_1}{\partial x_2} & \cdots & \frac{\partial f_1}{\partial x_n} \\ \frac{\partial f_2}{\partial x_1} & \frac{\partial f_2}{\partial x_2} & \cdots & \frac{\partial f_2}{\partial x_n} \\ \vdots & \vdots & \ddots & \vdots \\ \frac{\partial f_m}{\partial x_1} & \frac{\partial f_m}{\partial x_2} & \cdots & \frac{\partial f_m}{\partial x_n} \end{pmatrix}. \tag{2.45}$$

In the case of a discrete map (like the Chirkov map), the eigenvalues of the map evaluated at a fixed point are called the Lyapunov spectrum or the stability multipliers, which tell you the stability of a trajectory along the directions given by the eigenvectors of the Jacobian, a.k.a. the stable/unstable manifolds. For equations of motion which require numerical solutions, the Jacobian at any given point still tells you about the stability but a more careful treatment is required to extract the stability multipliers. Observing the stability of the fixed points as one varies a control parameter, such as K in the standard map, can tell you the type of bifurcation that occurs. Depending on the system there are many different types of bifurcations. A good discussion of stability and bifurcations can be found in Thompson and Stewart's book (36), which lists some of the common bifurcations and shows what happens to the stability multipliers as specific bifurcations occurs.

2.2.2 Floquet Stability Analysis

Here we explicitly discuss the details of analyzing the stability of periodic trajectories which require numerical solutions. This is a more complicated process than the case of a discrete map because we can no longer simply find the eigenvalues of the Jacobian at a given location to determine the stability of a trajectory that periodically passes

through it.

In the dynamical systems jargon, periodic trajectories are often called limit cycles, henceforth we will refer to them in this way. We expect the limit cycles to be periodic with a period that is either the frequency of the driving or some sub-harmonic of the driving frequency. If the period of the driving is T, then the period of a limit cycle can be written as pT, where p is a positive integer. Here, we must also define some additional notation. Let $\boldsymbol{T}$ be the time map which advances the operand by the period T. The time map is the same concept as the time evolution operator discussed in subsection 2.1.2 and, as we have defined it, produces a stroboscopic picture of the system. We will show later that the stroboscopic picture is equivalent to a specific, and popular, choice of Poincaré section.

Let us assume we are working only with two first-order equations, which could also be the first-order representation of a second-order differential equation of a single variable. Generally we write

$$\dot{x}_1 = f(x_1, x_2) \tag{2.46}$$

$$\dot{x}_2 = g(x_1, x_2). \tag{2.47}$$

The extension to more degrees of freedom is simple if one understands this example. We will define the location of a fixed point in the $2D$ phase space to be $\boldsymbol{r}_{fp} = (x_{fp1}, x_{fp2})$, where x_1 and x_2 might correspond to the positions and velocities of some particle, respectively.

In order to quantify the stability of a period-p limit cycle we use the Floquet stability analysis (37). A period-p fixed point under the time map $\boldsymbol{T}$ located at

$\boldsymbol{r}_{fp}$ remains invariant under $\boldsymbol{T}^p$. For the rest of this discussion, we work with the non-autonomous expressions of the equations of motion and therefore we will refer to $\{\boldsymbol{r}_{fp}\}$ as $\boldsymbol{r}_{fp}(t)$, so that we remember its explicit dependence on the independent variable t.

We want to find the linearized mapping under which the trajectory is invariant, which is defined as the linearized-map matrix $\boldsymbol{DT}^p$. Explicitly, it acts on the period-p fixed point $\boldsymbol{r}_{fp}$ in the expected way i.e. $\boldsymbol{DT}^p\boldsymbol{r}_{fp} = \boldsymbol{r}_{fp}$. If we can obtain the linearized mapping then the stability of $\boldsymbol{r}_{fp}$ is found by finding the eigenvalues of $\boldsymbol{DT}^p$.

To find $\boldsymbol{DT}^p$ we must integrate the linearized differential equations of motion for a trajectory close to $\boldsymbol{r}_{fp}(t)$. Call the perturbation of $\boldsymbol{r}_{fp}(t)$, $\boldsymbol{\alpha}(t) \equiv (x_{\alpha 1}, x_{\alpha 2})$. An infinitesimal perturbation to the initial conditions of $\boldsymbol{r}_{fp}$ results in a slightly perturbed trajectory which we call $\boldsymbol{\alpha}(t)$. In practice, $\boldsymbol{\alpha}(t)$ is all we have access to because the numerical solution is, in most cases, only an approximation of the true trajectory. The time-dependent equations of motion for $\boldsymbol{\alpha}(t)$ may be expressed as

$$\begin{pmatrix} \dot{x}_{1\alpha} \\ \dot{x}_{2\alpha} \end{pmatrix} = \boldsymbol{J} \begin{pmatrix} x_{1\alpha} \\ x_{2\alpha} \end{pmatrix}, \tag{2.48}$$

where we remind the reader that $\boldsymbol{J}(t)$ is the Jacobean matrix for $\boldsymbol{r}_{fp}(t)$

In general the solution to $\boldsymbol{\alpha}(t)$ may be expressed as

$$\begin{pmatrix} x_{1\alpha}(t) \\ x_{2\alpha}(t) \end{pmatrix} = x_{1\alpha}(0)\boldsymbol{w}^1(t) + x_{2\alpha}(0)\boldsymbol{w}^2(t), \tag{2.49}$$

where $\boldsymbol{w}^1(t)$ and $\boldsymbol{w}^2(t)$ are the two linearly independent solutions which can be written together as

$$\boldsymbol{W}(t) = \begin{pmatrix} w_1^1(t) & w_2^1(t) \\ w_1^2(t) & w_2^2(t) \end{pmatrix}. \tag{2.50}$$

The matrix $\boldsymbol{W}(t)$ is called the solution matrix because is allows us to express express Eq. (2.49) as

$$\begin{pmatrix} x_{1\alpha}(t) \\ x_{2\alpha}(t) \end{pmatrix} = \boldsymbol{W}(t) \begin{pmatrix} x_{1\alpha}(0) \\ x_{2\alpha}(0) \end{pmatrix}, \tag{2.51}$$

where $\boldsymbol{W}(0)$ is necessarily the identity matrix. Now we see that $\boldsymbol{W}(t)$ is the linearized flow $\boldsymbol{DT}^t$ and by substituting Eq. (2.51) into Eq. (2.48) we obtain the initial value problem

$$\dot{\boldsymbol{W}}(t) = \boldsymbol{J}(t)\boldsymbol{W}(t), \tag{2.52}$$

which we can solve for $\boldsymbol{W}(t)$. For the desired period-p, namely the one associated with $\boldsymbol{r}_{fp}(t)$, we numerically integrate Eq. (2.52) from $t = 0$ to $2\pi p$. This integration gives us the linearized map matrix $\boldsymbol{DT}^p$ from which it is easy to find the eigenvalues, or the Floquet stability multipliers of $\boldsymbol{r}_{fp}(t)$ under the time map (Poincaré map).

2.3 Long-Range Interactions

2.3.1 Extensivity and Additivity

Systems with long-range interactions are a source of unique problems in the field of statistical mechanics and thermodynamics. This is due to several properties of long-range systems which fall outside of the conditions normally needing to be satisfied

when applying the methodologies of thermodynamics. Simply from the words "long-range" the first infringement can be deduced, that long-range systems are not additive. If two systems with short-range interactions are brought together to form a larger system, then the energy difference between the conglomerate system and the sum of its constituents is the new potential energy from the boundary between them. In the thermodynamic limit, the potential energy of the boundary is small compared to the bulk and can be neglected, making short-range systems additive. In the case of long-range interactions, one particle will feel a significant potential created by every other particle, so the additional potential energy of two systems added together does not scale as the boundary but in a more complicated way that depends on the specific nature of the interactions (38). Directly related to the lack of additivity is the fact that systems with long-range interactions are not extensive because their energy diverges in the thermodynamic limit (39). Although these characteristics compel cautious use of the usual tools of statistical mechanics, they are also the source of many interesting dynamical and statistical features. Depending on the system of interest, such features include canonical and microcanonical ensemble inequivalence and relatedly negative specific heat (40), quasistationary states (different than metastable states which lie on local extrema of equilibrium potentials) whose lifetimes increase with the number of particles (41), and spontaneous creation of macroscopic structures in nonequilibrium states (42). In some cases, long-range interactions can greatly simplify problems. For instance, mean field models depend on one of two premises: (i) interactions are short-range but the system is embedded in a space of infinite dimension so that all bodies in the system are nearest neighbors, or (ii) interactions are infinitely long.

2.3.2 The Kac Prescription and the Core-Halo Distribution

Extensivity in a model with long-range interactions can be ensured by scaling the potential energy between two particles by factor of $1/N$, where N is the number of particles in the system. This scaling is referred to as the Kac prescription (43), and it lacks any physical justification aside from the prevention of a diverging energy in the thermodynamic limit. Though the Kac prescription solves (brushes aside) the problem of extensivity, it also reduces the pairwise interactions between particles to a vanishing value for large systems. Therefore, in the thermodynamic limit a particle's dynamics will primarily depend on its interaction with the collective excitations of the system (mean field). Teles et al. state that the phase diagrams for long-range systems, calculated using Boltzmann-Gibbs statistics, are not always equivalent in the microcanonical and canonical ensembles and that "The inapplicability of BG statistics to systems with long-range forces in the thermodynamic limit is a consequence of the ergodicity breaking" (44). The ergodicity breaking can be inferred simply through the nature of the Kac prescription. Infinitesimal interparticle interactions mean very small correlations (vanishing in thermodynamic limit) between particles, therefore the process of equilibration is quite far form the collisional process usually responsible for equilibrating systems with short-range interactions (obeying BG statistics). (44; 45).

Depending on the initial configuration of a long-range system, collective oscillations can develop. These collective oscillations often end up transferring energy to some particles which are located at the opportune points in the phase space to absorb the energy from them. As these particular particles absorb energy, becoming hot, the

rest of the system is cooled, resulting in a state that is fundamentally non-ergodic. Ergodicity is broken because as the collective oscillations die out in the heating of a subset of the system. The cold and hot regions can no longer couple to one another creating a divide in the phase space. A phase space in which particles are divided is not ergodic. A cold particle cannot enter the hot region of the phase space and the hot particles cannot enter the cool region of the phase space. These hot and cold regions form what is known as the "core halo" distribution. The increase of entropy remains satisfied though. The system can continuously increase its entropy through the spreading of the halo (hot region), but to do so as an isolated system the core must indefinitely collapse to conserve energy (46).

2.3.3 The Vlasov Equation

For short-range interactions the Boltzam equation describes the evolution of a distribution of particles in the phase space. Given that the correlations between particles in a long-range interacting system are vanishing in the thermodynamic limit, the collision term in the Boltzman equation would go to zero in the thermodynamic limit. The collisionless Boltzman equation is also known as the Vlasov equation. The famous Maxwell-Boltzmann distribution is the stationary solution to the Boltzman equation, but the Vlasov equation has an infinite number of stationary solutions depending on the initial distribution of particles in the phase space. In spite of the infinite number of solutions to the Vlasov equation, it is used to describe a variety of long-range interacting models (47; 48; 49). An additional issue in working with the Vlasov equation is that a solution is usually quite complicated. Between the difficulty in finding a solution and knowing that each initial distribution gives rise to a different stationary

solution one might be inclined to think that its study does not give rise to universal insights. However, Teles et al. have made great progress regarding these concerns (50). They work with the gravitational sheet model (1D self gravitation model). By proposing an ansatz solution to the Vlasov equation which is based on the physical limitations of the collapsing core (of the core-halo) in the phase space, they restrict the collapse of the core to a fully degenerate Fermi gas. Using the ansatz distribution function, they find the phase space density function and plug it into Poisson's equation. In this case, they must solve Poisson's equation numerically. With an expression for the (pseudo) static potential as a function of time, their ansatz solution to the Vlasov equation, and the constraints of conserved mass and energy, they find the full solution to the one-particle distribution function. They compare these findings to results for numerical simulations of the model and the fit is remarkable. We believe this is an extremely important step to understanding long-range systems especially through the use of the Valsov equation.

2.4 The Electric Curtain

The electric curtain (EC) is a device consisting of a series of parallel electrodes embedded in a dielectric surface. Alternating electric potentials are applied to these electrodes such that neighboring electrodes have a prescribed phase difference. An illustration of a two-phase EC is shown in Fig. 2.3. Different EC geometry and control parameters make it possible to create a variety of electric fields, which can generate a wealth of physical phenomena for charged particles. An EC configuration whose adjacent electrodes are driven by electric potentials with less than 180 degrees

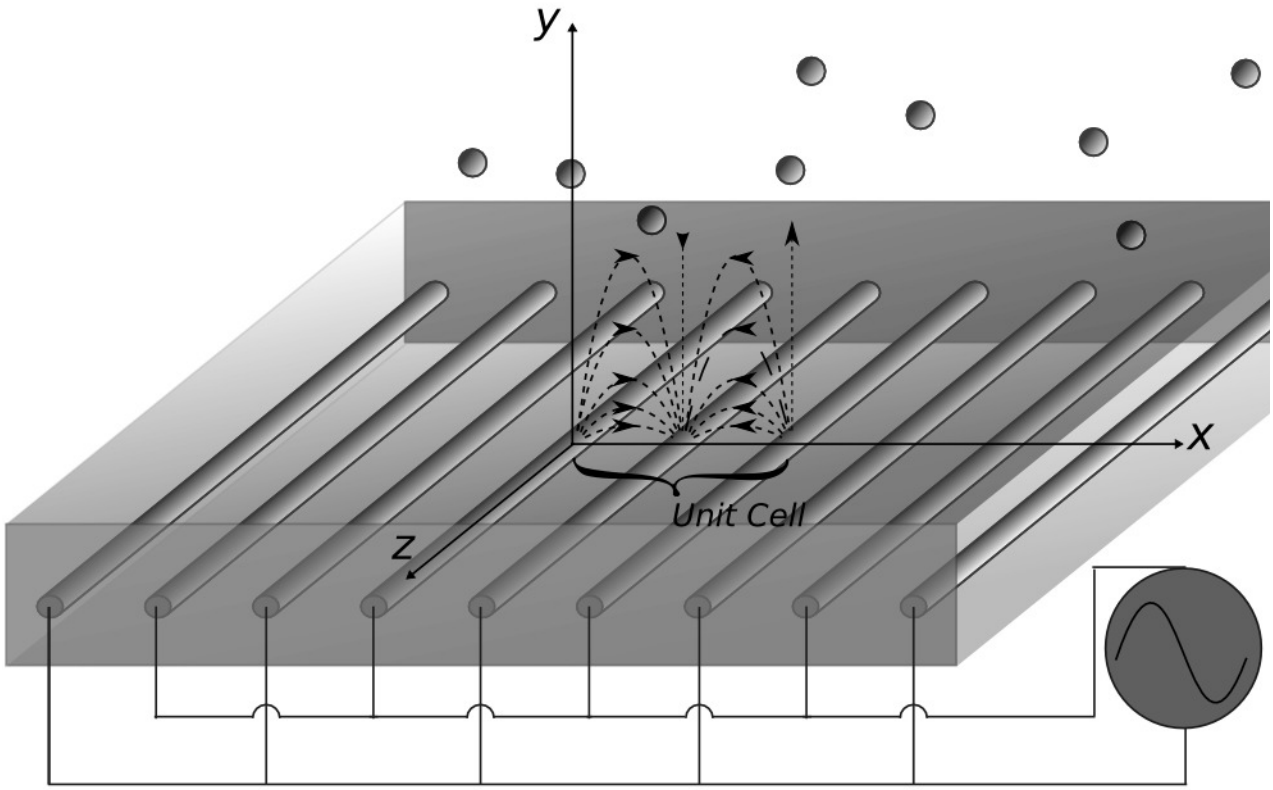

Figure 2.3: Transparent view of a 2-phase EC with our choice of axes are super imposed. The dashed lines represent the electric field lines in the positive y plane. The 2-phase EC is periodic over the set of electrodes marked as the "unit cell".

of phase difference will produce a traveling-wave electric field above the surface. Particle motions in these types of fields have been found to have several different modes of transport, which are commonly fited into three categories; surfing mode, hopping mode, and curtain mode (51). In the surfing mode, particles travel synchronously with the wave front, whereas in the hopping mode particles will stick to the surface and hop stochastically when freed by a sufficiently strong electrostatic force or collision with another particle. In the curtain mode, high frequency electric field

oscillations drive particles to be levitated above the electrode surface and travel in a spiraling trajectory with considerably slower average speed than the propagation velocity of the traveling wave.

Due to the variety of possible dynamics in an EC it has been proposed for manipulation and control of particles in many different applications. Patented in 1974 by Senichi Masuda, the EC was originally invented for particle control in an electrostatic powder-painting booth (52). Other proposed applications include separation of cells in the aqueous solution (53), separation of by-products from agricultural processes (54), transport of toner particles in photocopying machines (55), mitigation of charged dust build-up for extra-terrestrial exploration of dusty planets and moons (23), and separation of charged particles with different charge-to-mass ratios (56).

Despite those proposed applications of ECs, few commercial applications are reported. This may be in part due to the fact that particle dynamics induced by an EC are complex and still not well understood. The motion of particles in EC fields has been studied both experimentally and computationally by a number of investigators (57; 58; 59; 60; 61; 51; 62; 63). These investigations have shown a variety of different propagating and stationary modes, including the recent report of intermittent changes of many-body particle motion discovered by Chesnutt and Marshall (64) in a discrete-element simulation of transport on inclined ECs. In this work, we will contribute to the understanding of the complicated behaviors found for charged particles driven by a EC though an experimental investigation of the particle dynamics and statistics, as well as an in-depth dynamical systems study of a simple model system.

Chapter 3

Experimental Study of the Electric Curtain

3.1 Electric Curtain Experiments Relevant to the NASA Dust Mitigation Project

Lunar and Martin exploration and habitation is a long-term project for NASA (65). Its success requires availability of *in situ* reliable renewable sources of electrical power. As it stands, solar power is one of the few sources of energy available off planet and keeping solar panels clean is necessary in keeping them efficient. Fine lunar and Martian particles (66) on the solar panel surface can make the solar panel dysfunctional, therefore periodic cleaning of the surface is necessary. Limited power and payload restrictions require surface cleaning devices to be as light weight as possible. It has

been shown that the electric curtain (EC) is an excellent candidate for dislodging fine particles from a solar panel surface. The electrodes can be made to be translucent and only cover a small percentage of the solar panels entire surface area. The goal of the work presented in this section of chapter 3 is to understand the physical principles of this promising contrivance and refine its characteristics to satisfy future NASA applications.

One problem with microscopic regolith is that removing it from a surface can be surprisingly difficult due to the strong van der Waals adhesion and electrostatic force. Dust particles in the extremely dry Martian environment are often electrically charged and they may maintain an acquired charge for a long time. Simple removal techniques such as rubbing or wiping can abrade the surface. Even small amounts of abrasion on a solar panel will diffuse and disperse the incident light decreasing the power output. The EC may be able to remove most if not all the dust efficiently without any abrasion to the surface.

In order to better understand the use of an electric curtain (EC) for dust mitigation applications in extraterrestrial environments, we investigate the motion of charged Martian regolith simulant (JSC Mars-1A) in an EC field. An important aspect of this work was the method with which we charged the regolith simulant. In the next section, we will discuss this method and the details of charging and measuring the charge of many fine particulates. After the discussion of charging the regolith, we present our study of particles in the EC field, which consists of velocity distributions for different EC driving frequencies and different particle charges. We had two primary objectives in measuring the velocities of particles in an EC field. (i) To determine if there was "resonance" with the EC field in which particles, on average, developed

comparatively large velocities. (ii) To determine if charging particles influenced the interactions with the EC field in normal atmospheric conditions, or if the EC charged the particles sufficiently, making additional charging procedures extraneous.

3.1.1 Experimental Setup

Charging Dust

There are several difficulties in creating and confining even a small number of small (approximately $500\mu m$ diameter) particles with large electrostatic charges. The most ubiquitous issue is the coulomb repulsion between like charges, which can make a non-neutral cluster of particles difficult to contain. The second challenge is the electrostatic sticking of particles to a container's surface. Once you have succeeded in confining them, getting them back out of the container in a controlled fashion is likely the next obstacle. Also, the interaction of charged particles with the container will change the particles charge to some degree. The charge transfer between the container and the particles can be partially controlled though the choice of container material.

For the experiments described in section 3.1, we worked exclusively with the Martin regolith simulant, JSC Mars-1A. Through the use of a sieve, we restricted particle sizes to diameters less than $53\mu m$. In practice, some of the complications involving electrostatic interactions of the particles with each other and the container can be lessened with simple procedures, making it possible to charge and collect relatively consistent charge-to-mass ratio samples. We have found that the most important tool, when facing the challenges of herding charged particles, is having a container of the appropriate material. Aside from the requirement that it must be insulat-

ing, the determination of this material will largely depend on the electrochemical potential of the particles. The triboelectric series can be used to loosely predict the electrostatic charges of different materials coming in contact with one another, but the reality is that the understanding of the electrostatic charging of insulators, and the charge transfer between them, is still under some debate (67). Recently Zhang et al. (67) provided convincing evidence that small amounts of water on the surface of the insulators plays a critical role in these issues. We found that even with an understanding of the tribo-charging mechanisms, experimentation is required to find a suitable container for charged martin regolith, especially since the regolith consists of a mixture of different materials. Detailed information on the regolith simulant, including composition, grain size, etc., can be found at http://www.orbitec.com/store/JSC_Mars_1_Characterization.pdf. Through several trials we found that a plastic box found in the lab had the smallest interaction with the charged regolith.

We will now describe the method of particle charging used with the martin regolith simulant. It consisted of an air stream into which a sample of dust was injected, which carried the particulates over a sharp electrode to which a large electric potential was applied. To measure the charge of a dust sample, we used a Faraday cup. The charging setup that we have described is a piece of electrostatic powder coating equipment. We used an electrostatic powder coater made by Nihon Parkerizing co. ltd. (Subdivision: Parker Ionics Cx355Z, model GX7000S). The large electric potential applied to the aforementioned electrode and its sharp curvature creates a strong electric field, so that the particles become charged as they pass over it. Through some experimentation, we found the equipment parameters that consistently produced samples of similar

charge-to-mass ratios. The consistency of the method allowed us to predict a sample's charge by measuring its mass, an important capability since measuring the charge with the Faraday cup required putting the dust in contact with a conductor, drastically reducing the charge on the sample.

It is also important to discuss the charging of particles by the EC field. The EC's effect on the charge of particles makes it very challenging to know charge-to-mass ratios during an experiment. We need to distinguish between the samples that are charged only from the EC field and those that we charged using the electrostatic powder coating method *and* the EC field. We will refer to "uncharged dust" as regolith simulant which was not deliberately charged with the electrostatic powder coating equipment, and "charged dust" as the simulant which was deliberately charged with the equipment. Not only can the large electric field of the EC charge the particles, but so can interparticle collisions and collisions of particles with the surface of the EC. The question of whether or not the dust charged with the charging equipment is more charged during an experiment will be discussed in the results section.

We think it is necessary to inform readers about a particular strategy which can be used to measure the charge-to-mass ratio of dust as it comes off of the EC. Though we did not implement this method in the present experiments, it should be discussed because of its usefulness to anyone interested in continuing these experiments. Kawamoto (57) developed a method which consists of a box having parallel conducting plates on two of the inside surfaces, and a slit in the covered top. The slit is made to be only marginally wider than the average size of a particle. The box is placed so that its top surface is in the same plane as the EC's surface. The slit on top of the box restricts the entry point of particles coming off the EC into the box,

making the initial position of an entering particle known to the accuracy of the width of the slit. An electric potential difference between the conducting walls is applied so that as a particle falls its trajectory is governed by the electric field between the conducting plates and the particle's charge to mass ratio. By measuring the location and diameters of the particles on the bottom of the box, it is possible to determine their charge-to-mass ratios at the time they came off the EC.

Electric Curtain and Data Collection Setup

As mentioned in section section 2.4, ECs can be relatively easy to manufacture. One of the simplest ways to make one is by chemically etching a printed circuit board. A variety of electrode geometries and EC phases can be made this way. We used this method to make a 2-phase EC with flat rectangular electrodes of width $1mm$ and spacings of $1mm$. We define the axis that is in the plane of the electrodes (but running perpendicular to them) to be the x-axis, the axis that is perpendicular to the plane of the electrodes to be the y-axis, and the axis in the plane of the electrodes and running parallel to them as the z-axis, as shown in Fig. 2.3. In the following experiments, we use an EC with length $18cm$ and width $9cm$, measured in the x and z directions, respectively. The surface of the electric curtain was spray-coated with a dielectric material having a large breakdown voltage.

Alternating electrodes are attached to the AC power source such that adjacent electrodes are driven with a phase difference of π radians between them, creating a standing wave EC field, the potential of which is shown in Fig. 3.1 for a time when the field is non-zero. The peak-to-peak voltage, V_{pp}, applied to the electrodes was predetermined primarily by the maximum applied voltage before a discharge

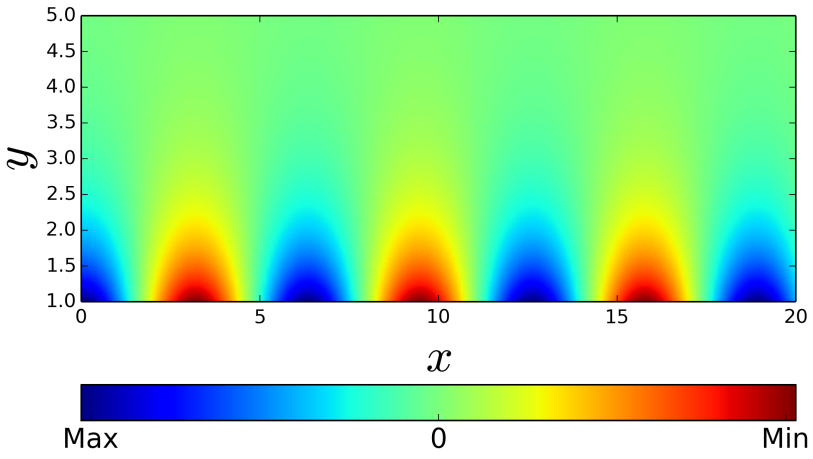

Figure 3.1: An approximation of the of the electric potential over two spacial periods of an EC for a time when the field is non-zero. The x-axis has been scaled so that spacial periodicity of x is 2π.

would occur. Though the dielectric had a large breakdown voltage, moisture on the surface of the EC could act as a conductor, effectively shortening the distance between electrodes. For humid conditions, the dielectric could not withstand more than $V_{pp} = 2000$, so we used $V_{pp} = 1500$ to be cautious. If a discharge occurred, the EC had to be resurfaced or even remade in some situations.

A single particle in an EC field will travel in the $x - y$ plane unless a source different from the EC pushes it in the z direction. Electrostatic interactions and collisions with other particles and the surface can do just that, producing non-trivial three-dimensional motion. Though in a dilute system, with a strong EC field the particle trajectories are relatively constrained to a small $x - y$ section of the volume above the EC. In order to observe particle motion in a narrow $x - y$ plane, we sent a laser through a cylindrical lens who's axis was parallel to the z-axis. This created an illuminating plane coincident with a particular chosen $x - y$ plane. The diameter of the laser beam was $2.3mm$ but by the time the beam passed thought the optical setup the width of the illuminating plane ended up being about $4mm$. A high speed camera was then placed so that its line of sight was parallel to the z axis, perpendicular to the illuminated plane, to record the particle motions.

3.1.2 Results

Charging Dust

In Fig. 3.2 we show the charge and mass measurements of martin regolith simulant samples that were charged using a variety of settings on the electrostatic powder coater described in section 3.1.1. For each choice of settings, six different samples

were charged. Then their charge and mass were measured in that order. The variation of the equipment settings consisted primarily of tuning the air flow and the potential across the electrode of the charging device. Though the temperature and the humidity also played a role in the results, we had little control over them in these experiments. The different settings are delineated with the acronym MCMR and then a number, where MCMR stands for *Mass-to-Charge Measure Ratio*. The specifics, including the humidity temperature, and settings of the electrostatic powder coater, of each measurement can be found in table 3.1.

Table 3.1: Charging Equipment Parameters

Settings	MCMR3 day1	MCMR3 day2	MCMR4	MCMR5
$V_{electrode}$ (KV)	80	80	80	80
Temperature (∘F)	78	70	69	69
Humidity (%)	34.0	32.5	32.5	32.5
sub air (MPa)	0.1	0.1	0.1	0.1
main air (MPa)	0.4	0.4	0.2	0.1
Settings	MCMR6	MCMR7	MCMR8	
$V_{electrode}$ (KV)	100	100	80	
Temperature (∘F)	68	69	69	
Humidity (%)	40	45	45	
sub air (MPa)	0.1	0.1	0.1	
main air (MPa)	0.4	0.1	0.8	

By examining Fig. 3.2, we see that the most linear relationship between a sample's charge and its mass comes from method MCMR7. From here on, when we refer to a sample as "charged" we mean that it was charged using the MCMR7 method since it produced the most consistent charge-to-mass ratios.

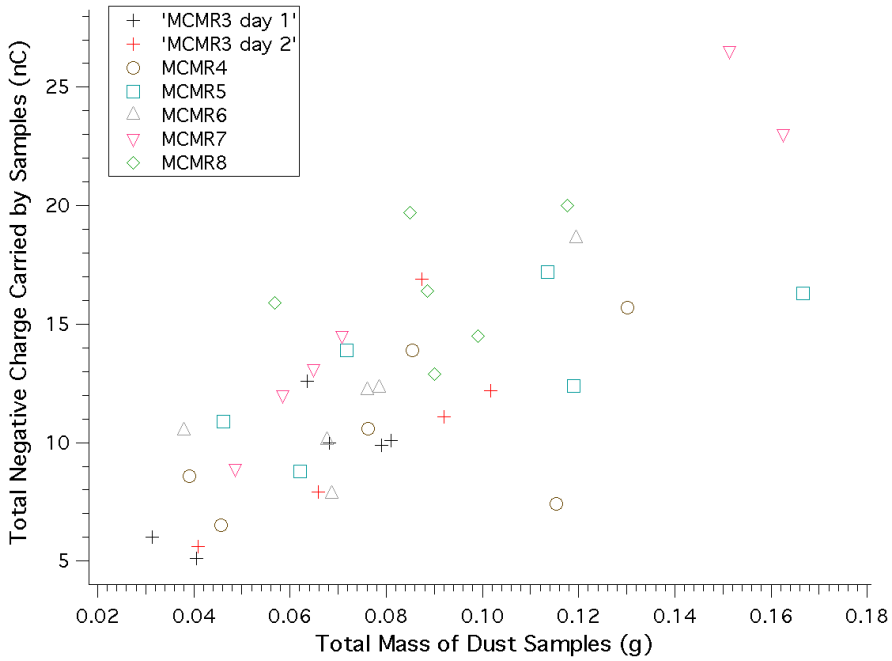

Figure 3.2: Charge of dust sample vs. the samples mass. The charge was measured with a Faraday cup. See table 3.1 for the details of each dust measurement method (MCMR).

Particle Velocities in an EC Field

We remind the reader of our two primary objectives in measuring the velocities of particles in an EC field. (i) To determine if there are certain system parameters with which the particles, on average, developed large velocities. (ii) To determine if charging particles influenced the interactions with the EC field in normal atmospheric conditions, or if the EC itself determined the charge of the particles while it was active.

Objective (i), stated in terms of the current application, involves finding the optimal driving frequency at which a certain size distribution of particles would clear from the area of the EC by measuring the velocity distributions. This approach relies on the assumption that large velocities are associated with good clearing efficiency. In some cases this is not true, for instance small particles in a large 2-phase EC field may

oscillate very quickly by following the field lines but not traversing the EC because they are stuck at a node of the field. By observing the particle trajectories, we have qualitatively confirmed that the driving frequencies in the experiment presented here are sufficiently small such that these types of trajectory are avoided.

Objective (ii) was originally thought to serve as a simple comparison but it turned out that objective (i) could only be studied with the charged dust. We found very few statistically significant differences in the average velocities of the uncharged dust for different driving parameters. Prior to the work that we present here, it was unclear whether the charging methods described above were necessary for experimenting in normal atmospheric conditions. Comparing the charged and uncharged particle velocities helped us determine the impact of this additional step in performing mitigation experiments.

In Fig. 3.3 we show the average velocity of the particles as a function of the driving frequency. For a given driving frequency, the average velocity of the particles was calculated using the following steps:

- Take a high speed video of the particles in the illuminated plane.
- Using a computer, track the particles in the video.
- With the particle tracks and the known frame rate of the camera, find the velocities of the particles from frame to frame.
- Find the average velocity of each individual particle that was tracked.
- Plot the average of the set of average particle velocities. We define this to be $\langle \|\vec{v}\| \rangle$, with a standard deviation s. The quantity s is the standard deviation of the mean values of trajectories velocity.

- Assuming each particle's average velocity is not correlated to the others and belongs to some unknown distribution, the error in the mean velocity, σ_v, is known to be approximated by $\sigma_v \approx s/\sqrt{N}$, where N is the number of particles tracked (68)

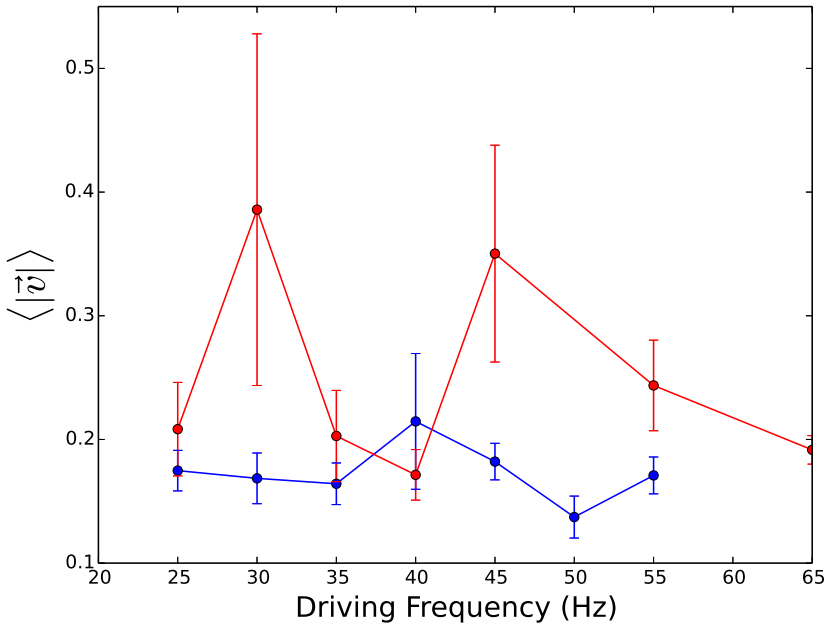

Figure 3.3: Each data point is the average of the mean particle velocity for a given driving frequency.

In Fig. 3.3 the uncharged data (blue) does not show any clear frequency dependence since the peaks and valleys of the curve are not larger than the error. The dip at 50Hz might warrant further investigation, but with the current data nothing can be said about it definitively. In the charged particle case, however, there is a clear peak at 45Hz. The average particle velocity of the charged particles goes from a small value, comparable to the uncharged case at 40 Hz, to a definitively larger value at 45Hz before slowly shrinking back down as the frequency is changed from 45Hz to

55Hz and again from 55Hz to 65Hz. Fig. 3.3 also shows that there are clear differences between the charged and uncharged data for certain values of the frequency. These frequencies are 30Hz, 45Hz, and 55Hz, which might be promising driving frequencies for charged dust mitigation applications.

3.1.3 Conclusions

In conclusion we have determined a simple procedure to charge martin regolith simulant for experimentation in an EC field. By using an electrostatic powder coater configured with the settings described in method MCMR7 in table 3.1, we can produce a relatively consistent charge-to-mass ratio on any given regolith sample containing particles with diameters less than $53\mu m$.

Using the charged martin regoloth simulant in a 2-phase EC field, we have shown a clear peak in the average particle velocity at the driving frequency 45Hz, shown in Fig. 3.3. This peak might be useful when trying to improve the mitigation of small particles which are generally the most difficult to clear because of their large electrostatic adhesion to some surfaces. The proclaimed usefulness of our velocity measurements assumes that a large average velocity corresponds to good clearing efficiencies. We believe that this is a reasonable assumption since the frequency range and field strength under investigation do not promote trajectories that oscillate quickly about one location. The Kapitza pendulum helps us understand that too high a driving frequency can lead to dynamical stabilization and that with too low a driving frequency the driving imparts little energy to the particles. If there is dissipation from air resistance or inelastic collisions, a driving frequency must be found that increases the average kinetic energy faster than the rate energy is leaving through dissipation.

It is reasonable to assume there should be a driving frequency where the field most productivity increases the kinetic energy of the system which we think is the peak found at 45Hz for our experimental setup.

3.2 One Dimensional Electric Curtain

The one-dimensional (1D) EC is a very simple to way to create a novel 1D electric field, one which is a longitudinal pseudostatic standing wave. Charged particles in a one-dimensional EC experience a time dependent potential that is very similar to the potential experienced by the bob of a Kapitza pendulum if the plane of rotation was perpendicular to the force of gravity. As discussed in section subsection 2.1.2, much work has been done on understanding the Kapitza pendulum from experimental, analytical, and numerical fronts; however, the 1D EC offerers a way to study these phenomena with interacting particles confined to the same STP potential. Here we will discuss the design of the 1D EC as well as some of the single and multiple particle dynamics that we have experimentally investigated.

3.2.1 Experimental Setup

To confine particles to one dimensional motion, a quadrapole trap is used. The quadrapole trap was made with 4 cylinders of length 21.5cm and diameter 2.5mm. Their central axes sit on a square of edge length 6.4mm. Each cylinder of the trap was driven with with an AC power source so that cylinders at opposite corers of the square are in phase, while neighboring cylinders are π radians out of phase. See Fig. 3.4 for a diagram of the quadrapole and EC setup. With Fig. 3.4 as a reference,

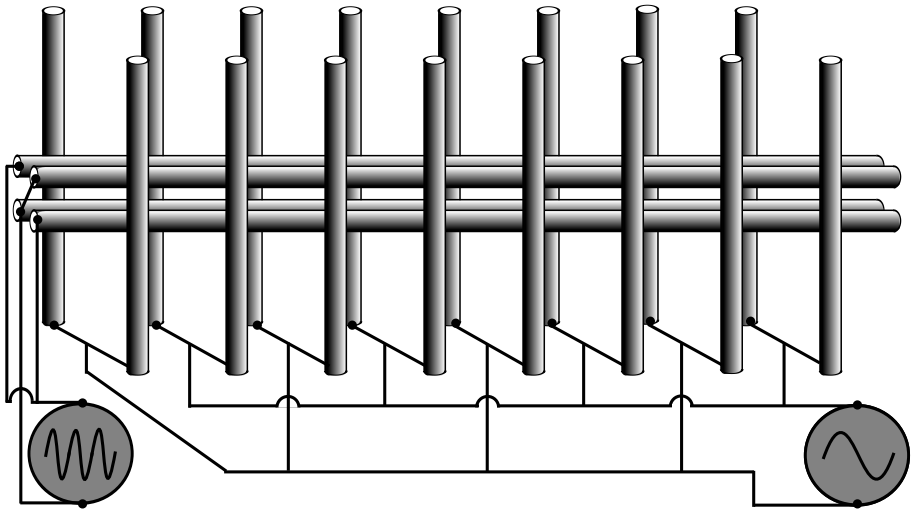

Figure 3.4: A high frequency quadrapole trap confines particles to one dimensional motion along the axis. The electrode arrays (2-phase ECs) on either side create a longitudinal standing wave for particles in the quadrapole trap.

we define the following coordinate frame: the x-axis is parallel to the quadrapole axis, the y-axis is parallel to the EC electrodes (vertical), the z-axis is perpendicular to the quadrapole axes and the faces of the ECs.

With the particles confined to the quadrapole, the two ECs on either side were configured so that their fields perpendicular to the axis of the quadrapole canceled as nearly as possible. This required careful positioning of the two EC so that their electrodes were at the same points on the x-axis making the system symmetric about the vertical plane running parallel to, and through, the quadrapole axis. To achieve this symmetry, one EC was mounted on a platform which could be adjusted in the x direction and the other EC was mounted on a platform which could be adjusted in the z direction. By removing the quadrapole trap, the EC adjustable in the z direction could be pushed directly up against the one that was adjustable in the x

direction. Then, by adjusting the appropriate EC in the x direction, the electrodes of the two could be carefully aligned. When the desired symmetry was achieved the space between them could be opened and the quadrapole placed back in its original position, resulting in the configuration shown in Fig. 3.4.

The specifications of the two ECs are as follows.

- Electrode diameter: $0.5mm$
- Electrode spacing: $5.0mm$
- Electrode length: $7.8cm$
- Electrode material: Copper

The two electric curtains were then driven with a square wave, making the potential roughly $\Phi(x,t) = \cos(kx)f(t)$, where $f(t)$ is a square wave with frequency ω. For our configuration $k = 2\pi/5.0mm^{-1}$.

These experiments were performed with glass beads having an advertised mean diameter of $35\mu m$. We show a histogram of the diameters as measured by us in Fig. 3.5. The glass beads were a desirable material because their geometries were relatively spherical and they also picked up a large enough static charge in the quadrapole trap to be captured by it. A bead's charge was also sufficiently large to feel the field created the ECs as well.

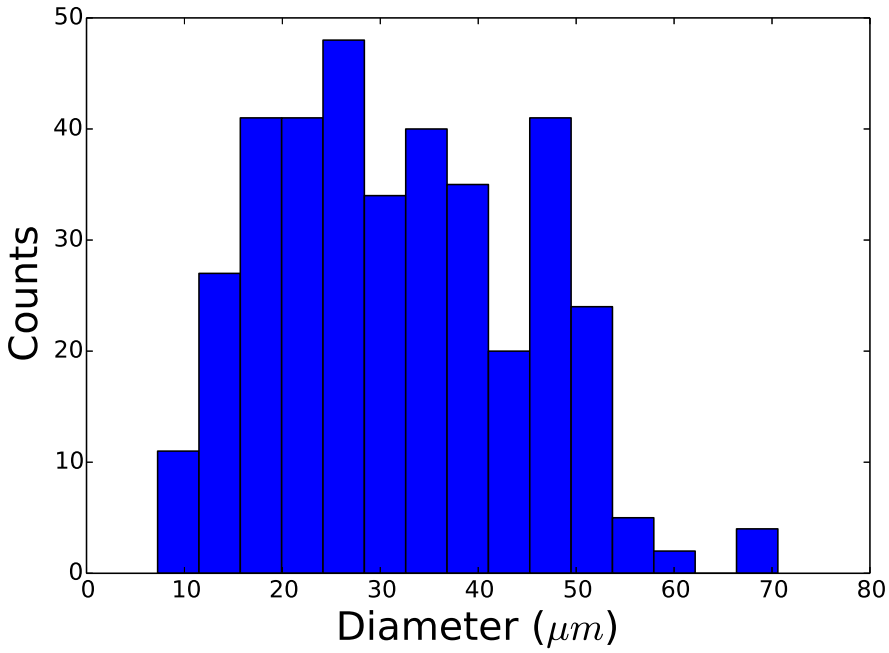

Figure 3.5: A histogram of the diameter of the glass beads used in the 1D EC experiments.

3.2.2 Results

Single Particle Dynamics

Due to the similarity between the form of the potential experienced by a particle in the one-dimensional electric curtain and the form of the potential experienced by the bob of a horizontal Kapitza pendulum, we set out to experimentally find a series of bifurcations as the driving amplitude of the ECs was tuned. See chapter 5 for numerical results of a similar STP driving. By observing the phase space of a single glass bead, we did not find the expected bifurcation sequence, but we did find interesting transitions in the particle dynamics as the field strength was increased.

The phase space for a single bead is shown in Fig. 3.6 as the twin EC driving

amplitude, A, was increased from $0 - 2KV_{pp}$. For $A = 0KV_{pp}$ the bead, initially

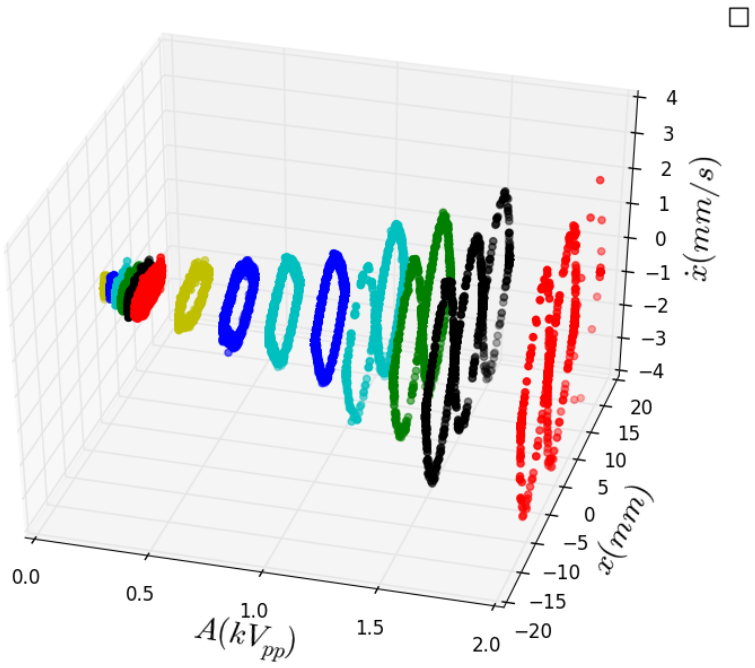

Figure 3.6: The phase plane of a 35μm glass bead in the one-dimensional EC (x vs $\dot{x}$) plotted for different values of driving amplitude, A.

placed near the location of an electrode in x (the antinode of the electric field), is stationary in x. As A is increased to $0.01KV_{pp}$ the particle remains stationary because the frequency of the driving is fast compared to the frequency of the natural oscillations. In this case, the natural oscillation frequency is the undamped particle oscillation frequency at the minimum of the static potential with amplitude A. In this regime (particle is stationary for non-zero field), the time-average force describes the dynamics. This is similar to the Bjerknes force in acoustics which pushes a particle to the nodes or antinodes (depending on the density of the particle) of a standing wave acoustic field.

Between $A = 0.01KV_{pp}$ and $A = 0.04KV_{pp}$ a bifurcation occurs changing the

previously stable stationary particle at the location of the electric field's antinode to a limit cycle. This behavior, and the increasing size of the limit cycle as A is increased from $0.04KV_{pp}$ to $1.00KV_{pp}$, is predicted by numerics, which will be discussed in chapter 5. At some point in the range $0.04KV_{pp} \geq A \leq 1.00KV_{pp}$, the experimental behaviors diverge from the numerical ones. We find no period-doubling bifurcations, and at $A = 1.00KV_{pp}$ the limit cycle is covering one full spatial period of the EC. The only time a particle covers and entire spatial period of the system in the numerics is in a chaotic regime or in a propagating state.

The second major transition in the dynamics occurs when A is increased from $1.00KV_{pp}$ to $1.20KV_{pp}$. At $A = 1.20KV_{pp}$, the particle dynamics change from oscillating about an electrode to hopping between three different electrodes. To clarify what we mean by "hopping" we use an example. Start the particle at an antinode of the field which occurs at the x positions of the electrodes. Call the node at which the particle is initially located E_0, and call the electrodes in the positive and negative x directions from E_0, E_1 and E_{-1} respectively. With the square wave driving applied to the electrodes, the particle feels attracted to the point E_0 (given the proper choice of phase) for the first half of the driving period. After a half period of driving, the sign of the potential on the electrodes flips and the particle is repulsed from E_0; simultaneously attracted to E_1 and E_{-1}. If the particle is located a small distance in the positive (negative) direction from E_0, then during the next half period it will travel to E_1 (E_{-1}). Shortly after it reaches $E_{\pm 1}$, the sign of the potential changes again. Unless A is sufficiently large (around $1.50KV_{pp}$), the particle does not ever move past $E_{\pm 1}$ and simply moves back to E_0 when it becomes attractive. On average, it appears to overshoot E_0 by a small amount, so that if the particle was at $E_{\pm 1}$, a temporal

period later it is at $E_{\mp 1}$.

Given the dynamics described above for $1.20KV_{pp} \geq A < 1.50KV_{pp}$, it is safe to assume there is some spatial asymmetry in the setup. Otherwise, the particle would do one of two things, either randomly hop from antinode to antinode of the electric field as it changes sign, or enter a propagating trajectory where it consistently overshoots the antinode it is attracted to before that electrode becomes repulsive. The repetition of the described process resulted in the particle's propagation. The localization to E_0 implies asymmetry within the experimental set-up. As one might expect, when A is increased past some critical value between $1.20KV_{pp}$ and $1.50KV_{pp}$, we find that the particle now hops relatively randomly between three different electrodes.

Multiple Particle Dynamics

We were also able to place multiple glass beads into the one-dimensional EC. In most cases all of the glass beads developed a positive charge and appeared to interact though a repulsive coulomb-like interaction. The choice of words "coulomb-like" is because the beads were clearly repulsive at short distances, but they would only separate finite distances in the quadrapole trap, indicating the possibility of higher-order moments in their interactions.

Under most choices of the driving frequency and amplitude, the interactions of multiple particles would cause them to spread out so that they were separated by at least several spatial periods of the potential. At these spacings, the interactions of the particles were not qualitatively noticeable and each particle would appear to undergo single particle motion. We did observe one particularly interesting case though, where the interactions played a critical role in the dynamics. What we found was that the

particles would pair up at the antinodes of the field while they were attractive, then when the antinode became repulsive the particle pairs would split. As each particle fell into the potential valley created by the newly attractive antinode, it would meet its new pair coming from the other side. This is exactly like the example we used in the introduction to illustrate possible STP behaviors. This pairing process would repeat itself so that a chain of particles would oscillate. Every particle would be π radians out of phase with its neighbors. We show the two different pairings that each particle experiences in a period of the driving in Fig. 3.7.

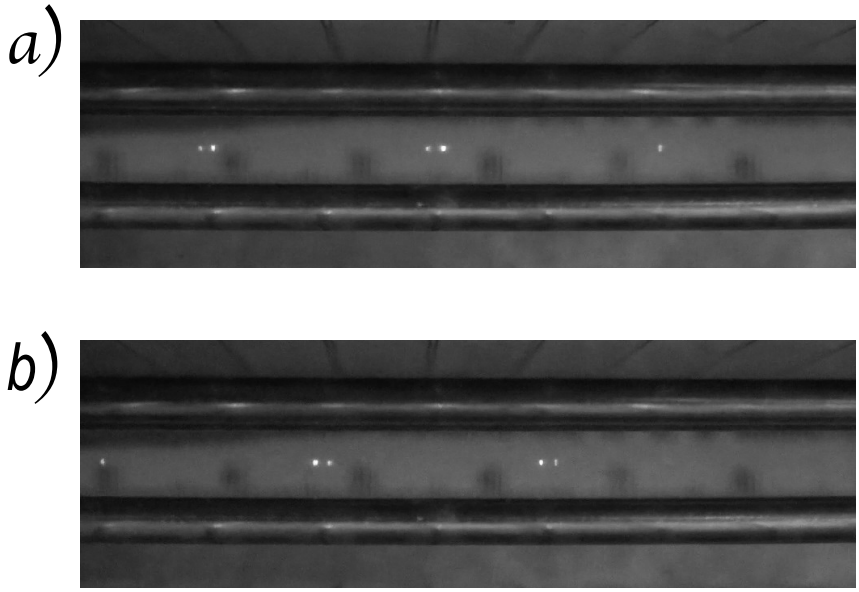

Figure 3.7: Five particles at two different points in their oscillations shown in parts a) and b) respectively. Parts a) and b) are separated in time by half a driving period.

3.2.3 Conclusions

Our primary results are threefold. Fist, we have shown that by using an electrostatic powder coater it is possible to charge martin dust simulant with consistent charge-to-mass ratios (See MCMR7 table 3.1). Second, we have shown that using the charged dust simulant and the method described in 3.1.1, it is possible to determine statistically significant peaks in the average velocity of the particles in an EC field. These results are relevant to the dust mitigation applications which use a 2-phase EC because the peaks correspond to driving frequency that the EC field maximally increases the kinetic energy of the particles. Third, we have shown that by using a quadrapole and two electric curtains, it is possible to create a one-dimensional STP electric potential where the particles experience a novel longitudinal electric field. We have also shown interesting results of the single and multiple particle dynamics in this one-dimensional STP potential.

Chapter 4

Nonlinear Dynamics of Single Particle in Electric Curtain Field

4.1 Introduction

In this chapter we discuss particles nonlinear motion in an electric field generated by a 2-phase EC. The 2-phase EC is also called a "standing wave" (52; 23) EC and for some time it was believed that this type of EC would have poor transport properties (52; 23). However, recently both experiments (69; 70) and numerical computations (59) have demonstrated that 2-phase ECs can be very effective at transporting particles, and in fact may exhibit two very distinct modes of transport under different conditions. The relative simplicity of the 2-phase EC makes it an attractive candidate for many of the proposed applications (see chapter 3).

A significant amount of work has been reported on ECs, but the nonlinear dynamics of the particles within an EC field have not been studied in detail from a dynamical systems point of view. Using simple mathematical models we have discovered a rich

variety of behaviors of charged particles in a two-phase oscillating EC electric field. A detailed understanding of the rudimentary particle motions might help us better interpret the complex phenomenon often observed in real EC experiments.

To simplify the mathematical presentation, we have only considered $1D$ and $2D$ motion of a single charged particle. While this is a very simple system, it is nevertheless sufficient to exhibit a interesting dynamical behaviors. Using a similar method to that outlined by Masuda and Kamimura (71) for 3-phase ECs, an approximate analytical equation has been derived for the motion of a charged particle in the 2-phase EC electric field. In general, motion of a single charged particle in the field of the 2-phase EC is two-dimensional, provided that no initial motion in the direction along the electrodes is introduced. However, a special case of one-dimensional particle motion, in which the electric field magnitude is insufficient to lift a particle initially located on the dielectric surface of the EC, is found to generate interesting particle behavior.

The equations of motion contain a time-dependent potential quite similar to the Kapitza pendulum as previously discussed (72; 73; 74). Our derived equations of motion are solved numerically and the behaviors of the particle motions induced by the oscillating electric field are examined. We obtain limit cycles which are fixed points in the appropriate Poincaré sections of the phase space, and bifurcations of these fixed points that lead to chaotic motions for a range of "interaction amplitude" values (a dimensionless parameter containing the amplitude of electrode linear charge density and the charge carried by a particle). Linear stability for very small interaction amplitude can be analyzed using a special case of the Mathieu equation (75; 28; 76; 25). As we increase the interaction amplitude, we show a variety of interesting

trajectory types in the $1D$ case and several predominant trajectories for the $2D$ cases.

4.2 Methods

4.2.1 Model Equations

Our model uses the so-called centerline charge approximation, in which a set of parallel electrodes in the x, z plane of the Cartesian axes are considered to be line filaments of infinite length oriented along the z-direction (71).The x-y plane is chosen to be orthogonal to the electrode axes (z-axis) as shown in fig. 2.3, where the x and y-axes are parallel and perpendicular to the dielectric surface, respectively. To find the electric potential and electric field above the plane of the electrodes produced by the set of equally spaced 2-phase electrodes, we adopt the conformal transformation used by Masuda and Kamimura (71):

$$e^{(-y+ix)2\pi/\lambda} = u + iv. \tag{4.1}$$

This transformation maps the x, y ($y > 0$) half-plane containing infinite numbers of periodic electrodes into a unit circle in the u, v complex plane containing just two electrodes. Therefore, the electric potential can be easily computed in the u, v plane. The inverse conformal transform is then performed to map the expression back to $x - y$ coordinates. The detailed derivation is given in Appendix A. Based on the derivation, the electric potential can be simply expressed as:

$$\Phi(x, y) = \frac{-Q}{4\pi\epsilon_0} \cos\omega t \ln \frac{\cosh ky + \cos kx}{\cosh ky - \cos kx}$$

.

Using $\boldsymbol{E} = -\nabla\Phi$ the electric field in the x and y directions is found to be

$$E'_x = \frac{kQ}{2\pi\epsilon_0}\sin(kx')\cos(\omega t')\frac{\cosh(ky')}{\cosh^2(ky') - \cos^2(kx')}, \tag{4.2}$$

$$E'_y = \frac{kQ}{2\pi\epsilon_0}\sinh(ky')\cos(\omega t')\frac{\cos(kx')}{\cosh^2(ky') - \cos^2(kx')}, \tag{4.3}$$

where Q is the linear charge density amplitude of an electrode, m and q are the mass and electric charge carried by a particle, respectively, k is the wave number, and ω is the angular driving frequency of the driving electric fields. It is noted that we use the primed variables here to save unprimed variables for their dimensionless counterparts, which are defined below. For the centerline charge approximation to be valid it is required that the dielectric surface be located a minimal distance above the electrodes (71). However, if the surface is far from the electrodes, the cosh-term on the right-hand side of Eq. (4.2) and Eq. (4.3) diminishes as $1/\cosh y' \sim e^{-y'}$ and consequently the electric field magnitude rapidly approaches zero.

The dimensionless time, horizontal and vertical positions are defined by $t = \omega t'$, $x = kx'$, and $y = ky'$. A dimensionless interaction amplitude (A), gravitational acceleration (g) and damping coefficient (β) are, respectively, defined by $A = \frac{k^2 qQ}{4\pi\epsilon_0 m\omega^2}$, $g = g'k/\omega^2$, and $\beta = \beta'/m\omega$, where β' is the damping coefficient, and g' is the gravitational acceleration. The dimensionless form of the differential equations governing the particle motion are:

$$\frac{d^2x}{dt^2} + \beta\frac{dx}{dt} = A\sin x\cos t\frac{2\cosh y}{\cosh^2 y - \cos^2 x}, \tag{4.4}$$

$$\frac{d^2y}{dt^2} + \beta\frac{dy}{dt} = A\sinh y\cos t\frac{2\cos x}{\cosh^2 y - \cos^2 x} - g. \tag{4.5}$$

Letting the dimensionless spacing of the distance between neighboring electrodes be π, the system is periodic over a distance $\lambda = 2\pi$ in x. We choose the dielectric surface to be at $y = 1$, i.e. $y' = 1/k = \lambda/2\pi$, for which the centerline charge approximation holds.

4.2.2 Distinction of One and Two Dimensional Regimes

Two distinct regimes are considered: (1) A one-dimensional regime where the particle is constrained to roll or slide back and forth on the dielectric surface; (2) a two-dimensional regime where the particle moves in the x-y plane, either being levitated above the surface or bouncing off of it. Dissipative forces are included in the model for both regimes. For the $1D$ regime, dissipative forces may arise both from rolling resistance between the particle and the surface and from the viscous fluid force (Stokes drag) between the particle and the surrounding air. Both of these dissipative forces are proportional to the particle velocity (77). In the $2D$ case, the particle is assumed to have elastic collisions with the dielectric surface, so the only dissipation is from fluid drag force. The transition from motion on the surface ($1D$) to the $2D$ regime occurs when the maximum vertical force imposed on a particle immediately above an electrode exceeds the gravitational force on the particle. For a charged particle attached to the dielectric surface, the electric field is evaluated at a value of y' equal to the particle centroid position. Letting the gravitational force balance the maximum

electrostatic force, the maximum value of the interaction amplitude A for which the particle remains on the surface can be obtained by setting the left-hand side of Eq. (4.5) to zero, giving

$$\frac{A}{g} \leq \frac{cosh^2 y - 1}{2 \sinh y} \tag{4.6}$$

With the location of the surface at $y = 1$, the critical value of this ratio for which the $1D$ approximation applies is obtained as $A/g \leq 0.588$. In order to further simplify this system, we neglect the adhesive van der Waals force. This simple system is used to examine the nonlinear dynamics for small variations over a range of A with constant values of β.

4.3 Time Maps

We classify different trajectories by the periodicity of their limit cycles in the full phase space. The interaction amplitude, damping, and initial conditions determine the periodicity of the particle trajectory. We compare the temporal length of a limit cycle to the inverse of the driving frequency of the electric field by using time maps. Time maps are used to represent the advancement of an orbit in phase space by some amount of time. In general, a particle's position and velocity determine its position in phase space, which can be represented as a vector function $\boldsymbol{r}(\boldsymbol{r}_0, t)$, where $\boldsymbol{r}_0$ is the initial position in the phase space. We choose the time maps to be represented in the form $\boldsymbol{f}(\boldsymbol{r}_0, t = 2\pi n)$. The time mapping gives a stroboscopic view of the parametric function $\boldsymbol{r}$ when n is a positive integer ($\mathbb{Z}^+$). For $n \in \mathbb{Z}^+$ the time mapping highlights the relationship between the period of a trajectory and the driving frequency. We

define an operator $\boldsymbol{T}$ that maps the system forward in time by 2π, so that the function $\boldsymbol{f}(\boldsymbol{r}_0, t = 2\pi n)$ may be written as $\boldsymbol{T}^n\boldsymbol{r}$.

The $2D$ EC has five degrees of freedom x, y, $\dot{x}$, $\dot{y}$, t. The periodicity of the system in x and t implores the use of a toroidal phase space. We use this notion of a toroidal phase space to fashion our Poincaré sections. We defer to the $1D$ EC in order to visualize the toroidal phase space (fig. 4.1). For the $2D$ EC we cannot graphically depict the full phase space but we use the same periodic geometries to fashion Poincaré sections. A Poincaré section includes any point where a continuous trajectory or flow transversely intersects a subspace of the space the trajectory occupies(37). Strobing a periodically driven system will produce Poincaré sections of $d-1$ dimension, where d is the dimension of the full phase space. This is equivalent to observing time maps $\boldsymbol{T}^n$ acting on a point in phase space. It becomes apparent that this method of strobing or time mapping produces Poincaré sections when we look at a particle's trajectory as a function of time t passing through a $x, \dot{x}$ phase plane at a particular time t. The particles path is always transverse to the $x, \dot{x}$ plane and therefore a point of intersection of the trajectory with this plane is a convenient sub space that satisfies the criterion necessary to be a Poincaré section. It is also true that time maps generate Poincaré sections for the $2D$ EC, but in this case the mappings represent intersections of a trajectory with a non-planar subspace. This is still a Poincaré section because the flow through the subspace is guarantied to be transverse to it due to the positive rate of change of time.

By filling a plane in phase space with an array of initial conditions, a large number of possible trajectories can be obtained for given values of β and A. For instance, in $1D$ simulations initial conditions are prescribed in the $x - \dot{x}$ plane at $t = 0$. For

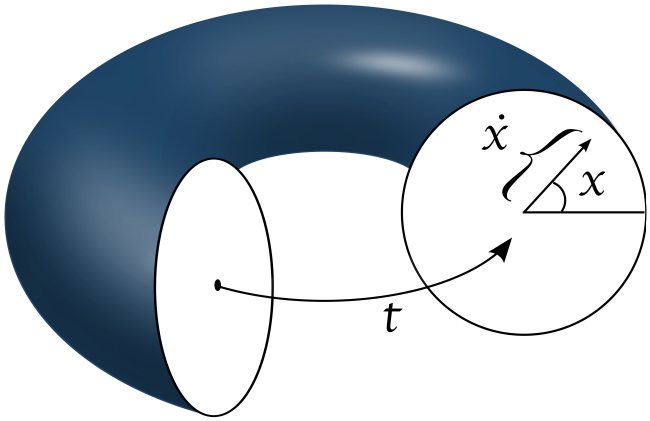

Figure 4.1: Due to the periodicity of the EC in the x-direction, and the periodic fluctuations of the electric field with time, it is useful to use toroidal geometry to describe the $1D$ EC phase space. We define the t-axis as the line at the major radius when the minor radius is zero. The position and velocity at a given time may then be represented as a point in the plane orthogonal to the time axis described by an angle (x) and radius ($\dot{x}$). The origin of this plane is located at the intersection with the t-axis.

$2D$ simulations, initial conditions are prescribed on a planar section of the four-dimensional phase space at $t = 0$. Different initial planes are used to explore different regions of the phase space. We define a region of phase space filled with an array of initial conditions as a *block*. A group of positions in the phase space at a given time is represented by a $2 \times N$ dimensional matrix $\boldsymbol{B}$, where the first index (2) is the dimensionality of the block and the second index (N) is the number of different initial conditions in the block. The advancement of these initial conditions in phase space by intervals of the driving period can be represented with time maps by $\boldsymbol{T}^n\boldsymbol{B}$. The different attractors in the system can be found by taking $\boldsymbol{T}^n\boldsymbol{B}$ as $n \to \infty$. As discussed above, a series of time maps can be used to generate a Poincaré sections of $\boldsymbol{B}$ in the phase space.

4.4 Results

4.4.1 One Dimensional Regime

For small A and finite β, a particle on the dielectric surface will drift toward the nearest electrodes. For an electrode located at $x = 0$, an analytical solution can be obtained for particles at small distances $|x|$ from the electrode. Using the leading-order Taylor series approximations $\sin x \approx x$ and $\cos x \approx 1$, the multiplying factor in Eq. (4.4) can be approximated as

$$\frac{2\cosh y}{\cosh^2 y - \cos^2 x} \approx \frac{2\cosh y}{\cosh^2 y - 1} \equiv C, \tag{4.7}$$

where C is a constant for $y = 1$. The equations of motion then become

$$\frac{d^2x}{dt^2} = ACx\cos t - \beta\frac{dx}{dt}. \tag{4.8}$$

Under the transformation $x(t) = e^{(-\beta t/2)}u(t)$ and $t = 2\theta$ it takes the form (25)

$$\frac{d^2u}{d\theta^2} = u(a - 2q\cos 2\theta), \tag{4.9}$$

where $q = AC/8$ and $a = -\beta^2$. Equation (4.9) is the canonical form of the Mathieu equation. There are infinite sets of alternating stable (periodic) and unstable solutions for variation of the parameters a, q (78). Here we are only interested in the bound solutions because unstable trajectories force the consideration of larger $|x|$ for which this approximation breaks down. The function $u(t)$ may be expressed as a linear combination of the cosine and sine type elliptic functions. It is well known that the

stability of the elliptic functions depends on the parameters a and q. The stability boundary may be expressed as a function $q(a)$. Gunderson et al. (79) derive a condition for asymptotic stability based the relationship between the two parameters. The inequality found by Gunderson et al. that needs to be satisfied for asymptotic stability in the EC takes the form $A < 2\beta^2/C$. This relationship only holds for small a and q, but so does the analytical treatment of the EC. We refer the reader to McLachlan(25) for a thorough description of elliptic functions and their different representations.

For larger values of A, particles are not necessarily confined above the electrodes. In order to analyze this system and highlight the dimensionality of the full phase space, it is convenient to express Eq. (4.4), with $y = 1$ denoting the dielectric surface, as a set of first-order autonomous differential equations.

$$\begin{aligned} \dot{x}_1 &= x_2 \\ \dot{x}_2 &= A \sin x_1 \cos x_3 \frac{2 \cosh 1}{\cosh^2 1 - \cos^2 x_1} - \beta x_2 \\ \dot{x}_3 &= 1 \end{aligned} \tag{4.10}$$

The following transformations used in Eq. 4.4 give us Eq. 4.10: $x \to x_1$, $\dot{x} \to x_2$, and $t \to x_3$. We know from the previous discussion of time maps that a period-p fixed point in the Poincaré sections, located at $\boldsymbol{r}_{fp}$ in the phase plane x_1 x_2 is defined by $\boldsymbol{T}^{pn}\boldsymbol{r}_{fp} = \boldsymbol{r}_{fp}$, where $n \in \mathbb{Z}^+$. A period-p orbit (i.e limit cycle) is one which repeats itself after p driving cycles. All Poincaré sections obtained by sequential time maps have two fixed points within the toroidal phase space (see fig. 4.1) located at $x_1 = 0$

and $x_1 = \pi$. These fixed points are representative of limit cycles of period-1 in the phase space. These two limit cycles are the only invariant sets in the full parameter and phase space which exist for all values of A and β. For definiteness, we define $\boldsymbol{r}_{fp1}$ to be the $x_1 = \pi$, $x_2 = 0$ fixed point in the PoincarĂŠ sections. To distinguish between the fixed point in the Poincaré section and the corresponding limit cycle in the phase space, we define the full invariant set composing the limit cycle as $\{\boldsymbol{r}_{fp1}\}$, where the curly brackets denote a set.

In general, the stability of a fixed point in the Poincaré section can be analyzed using Floquet theory (24), details of which are provided in Appendix B. By integrating the linearized equations of motion about a periodic orbit with periodicity p, a solution for small perturbations of the fixed-point solution lying on the closed orbit is obtained. A similar approach is illustrated in (72) for Floquet theory applied to the parametrically driven pendulum which is mathematically similar to the $1D$ EC. The eigenvalues (Floquet stability multipliers) λ_1, λ_2 are generally complex, where a fixed point in the Poincaré section is unstable when the magnitude of λ_1 or λ_2 is greater than unity. In cases where there is no analytical expression for a fixed point as a function of A, a polynomial curve fit is used to estimate the fixed point as a function of A.

We initially focus attention on the $\beta = 0.1$ case because this value is typical of a variety of realistic EC configurations. A bifurcation diagram for this case is shown in fig. 4.2. The points corresponding to each value of A in this bifurcation diagram are obtained by plotting the positions of a block of 1830 different initial conditions covering the region $0 \leq x_1 < 2\pi$ and $-1.5 \leq x_2 \leq 1.5$, plotted after 637 time maps. This process is repeated for different A values ranging from 0 to 0.4, in steps of

0.0008. In order to indicate the number of initial conditions corresponding to each point in this diagram, a hexagonal histogram was formed in which the x_1-position is discretized into 400 bins. The color bar in fig. 4.2 represents the logarithm of the number of points in the corresponding bin.

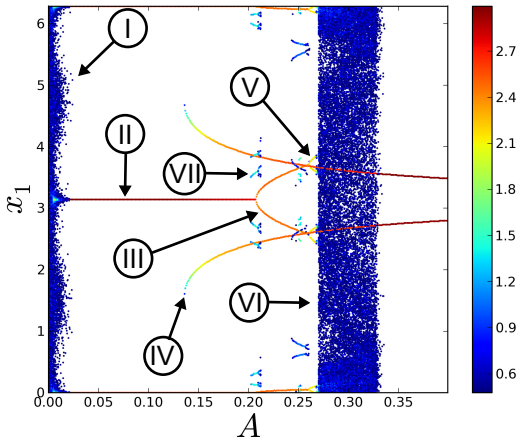

Figure 4.2: A bifurcation diagram made by taking a two dimensional histogram of the final Poincaré section of 1830 different initial conditions for 500 different values of A. β is set to 0.1*. Roman numerals denote the individual features focused on in this work; Region I: With A being close to zero transients take a long time to die out. Region II: A stable fixed point above the electrode representing a sink where particles are stationary. Region III: A period-2 orbit oscillating about the electrode. Region IV: Stable propagating trajectories with comparatively high speeds. Region V: Four fixed points in the digram representing two period-2 trajectories born out of a cyclic fold bifurcation. Region VI: Period doubling leads to chaotic motion. Region VII: A period-4 fixed point in the Poincaré sections that discontinuously appears and disappears over variations of A.*

For very small values of A, denoted by region I in fig. 4.2, the x_1 position of the points in this figure are widely dispersed. This scattering occurs because the transients are very slow to die out for small values of A, and therefore the block of initial conditions has not yet reached its final state. As we increase A, a single line is observed in the fig. 4.2, denoted by region II, representing the $\boldsymbol{r}_{fp1}$ attractor. For these values of A, this attractor is an asymptotically stable fixed point in the

Poincaré sections, so that initial conditions in a small neighborhood about $\boldsymbol{r}_{fp1}$ map to $\boldsymbol{r}_{fp1}$. In regimes I and II, the direction of the time-averaged force on the particle points to locations of constant electrostatic potential. This condition is similar to the well-known Bjerknes force in acoustics (80), wherein the acoustic radiation force on a particle points to either the nodes or antinodes of a standing acoustic field. The fixed point $\boldsymbol{r}_{fp1}$ remains asymptotically stable for values of A in the interval $0 < A < A_{c1}$, where $A_c1 \equiv 0.20761 \pm .00001$.

At $A = A_{c1}$, a bifurcation of the $\boldsymbol{r}_{fp1}$ fixed point is observed, beyond which the single line splits into two period-2 curves, which are symmetric about the $x_1 = \pi$ line as indicated in region III in fig. 4.2. The real and imaginary parts of the two Floquet stability multipliers, λ_1 and λ_2, for $\boldsymbol{r}_{fp1}$ including values of A close to A_{c1} are shown in fig. 4.3. The discontinuity in fig. 4.3, where the imaginary parts go to zero, represents the transition of the fixed point from an attracting focus to an attracting node. The point at which λ_2 decreases below -1 in fig. 4.3 corresponds to the bifurcation, where $\boldsymbol{r}_{fp1}$ becomes a period-1 saddle. Beyond this bifurcation, the fixed point becomes linearly unstable in what is called a supercritical flip bifurcation. The instability of the period-1 saddle creates a stable limit cycle of period-2 about $\boldsymbol{r}_{fp1}$. It may be surprising that the first oscillations are not period-1. This is because period-1 oscillations are not a harmonic of $\boldsymbol{r}(t)$ (73). There are, however, two period-1 fixed points apparent in fig. 4.2 seen for $A > 0.13$ (one on either side of $x = \pi$) denoted by region IV which represent propagating trajectories. These propagating trajectories travel once through the toroidal phase space per driving cycle making them period-1 fixed points in fig. 4.2 but they are not periodic oscillations because they are constantly traveling in one direction.

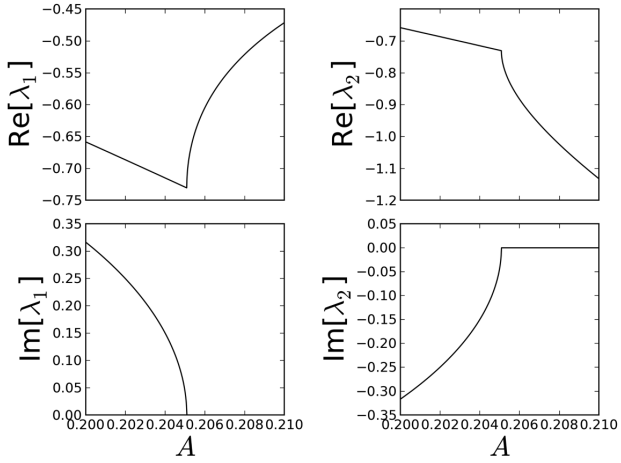

Figure 4.3: Floquet stability multipliers of the $(x = \pi, \dot{x} = 0)$ *fixed point for a range of* A *in which the first bifurcation occurs. The discontinuity is the transition from an attracting focus to an attracting node. The supercritical flip bifurcation happens as* $RE[\lambda_2]$ *becomes smaller that* -1*.*

We call the uppermost region III curve $\boldsymbol{r}_{fp2}$. $\boldsymbol{r}_{fp2}$ is an attracting focus for values of $A \leq 0.234$. Just as in the first bifurcation, the attractor $\boldsymbol{r}_{fp2}$ transitions to an attracting node shortly preceding the second bifurcation, which occurs at $A = A_{c2}$, where $A_{c2} \equiv 0.26077 \pm 0.00001$. A close-up view showing this bifurcation is given in fig. 4.2b. This bifurcation is of the type known as a cyclic fold bifurcation, where the fixed point becomes unstable and the symmetry of the trajectory corresponding to the fixed point is broken at the bifurcation point. As A is increased through A_{c2} two new possible trajectories are spontaneously created denoted by region V in fig. 4.2. The initial conditions determine which of the new possible trajectories a particle will settle into. As the particle trajectory is known to be highly sensitive to small changes in initial condition, this type of bifurcation is known to produce hysteresis for processes in which A is varied about A_{c2} (36). An alternative viewpoint of this bifurcation sequence is given by plotting projections along the x_3 (t) axis of the phase

space onto the x_1, x_2 plane for some particular values of A in fig. 4.4a. This figure shows the fixed point $\boldsymbol{r}_{fp1}$ bifurcating into a sequence of limit cycles, denoted in the Poincaré section by $\boldsymbol{r}_{fp2}(A)$, as A is increased past $A = A_{c1}$. These curves are point symmetric about $(x_1 = \pi, x_2 = 0)$ in the interval $A_{c1} < A < A_{c2}$. For $A > A_{c2}$, two families of trajectories are observed, one of which shifts in the positive x-direction and the other shifts in the negative x-direction, breaking the point symmetry. We only show one of the two possible trajectories for $A > A_{c2}$ in figure 4.4a for clarity. Sample trajectories for each of these intervals are plotted on the x_1, x_2 plane in fig. 4.4b to highlight the symmetry breaking. The first bifurcation at $A = A_{c0}$ looks geometrically similar to a Hopf-bifurcation in fig. 4.4a, but this is an artifact of the projection process along x_3, where in fact the $\{\boldsymbol{r}_{fp1}\}$ set that gives rise to the $\boldsymbol{r}_{fp1}$ fixed point in fig. 4.4a is a limit cycle rather than an equilibrium point in time.

Table 4.1: Period Doubling Bifurcations

A_{cn}	Bifurcation	A	Period of New Limit Cycle
A_{c1}	Supercritical Flip	0.20761 ± 0.00001	2
A_{c2}	Cyclic Fold	0.26077 ± 0.00001	2
A_{c3}	Supercritical Flip	0.26798 ± 0.00001	4
A_{c4}	Supercritical Flip	0.26903 ± 0.00001	8
A_{c5}	Supercritical Flip	0.26928 ± 0.00001	16
A_{c6}	Supercritical Flip	0.269336 ± 0.000002	32

Following this second bifurcation (region V), a series of period-doubling bifurcations occurs, with the first of these bifurcations happening at $A = A_{c3}$, where $A_{c3} \equiv 0.26798 \pm 0.00001$. Table 5.1 shows the values of A at which each period-doubling bifurcation occurs, the period of the limit cycle after the bifurcation and the type of bifurcation. It can be seen in fig. 4.2 that the period doubling cascade initial occurs in a very small range of x; in fact, it occurs in a very small volume of the full

phase space. The density of the higher period trajectories, even after the period-32 bifurcation, make if extremely difficult to distinguish periodicities. Using A_{c3}, A_{c4}, and A_{c5} we calculate the Feigenbaum constant δ to be 4.2000. Using A_{c4}, A_{c5}, and A_{c6} we calculate the Feigenbaum constant to be 4.4643. This progression looks as though it might lead to the universal value of $\delta \approx 4.6692$ (81). The Feigenbaum constant δ s be evaluated with

$$\delta = \lim_{n\to\infty} \frac{A_{cn-1} - A_{cn-2}}{A_{cn} - A_{cn-1}}. \tag{4.11}$$

A_{cn} are the values of A for which a period-doubling bifurcation occurs, A_{cn} being the n^{th} bifurcation. As A is increased, the period-doubling cascade leads to a chaotic regime, identified by the scattered points denoted by region VI in fig. 4.2. This chaotic state exhibits a strange attractor, which consists of a region in phase space with fractal geometry to which particle trajectories approach as $t \to \infty$. A Poincaré section of the strange attractor for this system is plotted in fig. 4.5. As shown in fig. 4.6f, this chaotic state exists simultaneously with the two stable period-1 limit cycles (region IV), where the latter have substantial higher velocity magnitude than the points in the chaotic state. The basins of attraction for the strange attractor and the stable limit cycles are plotted in fig. 4.6 for $A = 0.3$, along with plots showing the evolution of these basins in time as they approach their respective attractors. We have found the largest Lyapunov exponent for this chaotic attractor to be 0.165 ± 0.001. In general The largest positive Lyapunov exponent is a way of quantifying the strength of chaos. More specifically it is the measure of the rate with which two infinitesimally close initial conditions in phase space will separate. We have calculated the largest Lyapunov exponent by comparing a fiducial trajectory to a

neighbor placed infinitesimally close. After a small period of time we re-orient the perturbed trajectory along the vector for which there was maximal separation. By continuing this process for many iterations and throwing away the transients we find the maximum separation of the perturbed trajectory from the fiducial trajectory. With these data it is straight forward to calculate the Lyapunov exponent(36).

The last feature we focus on in fig. 4.2 are the stable limit cycles that appear and disappear discontinuously for small variations in A. We have chosen one of these limit cycles (denote as region VII in fig. 4.2a) to analysis the stability in order determine the nature of its creation and disappearance. In fig. 4.2 four fixed points appear as A is increased through 0.20182 ± 0.00001. These fixed points correspond to a period-4 limit cycle shown in fig. 4.7 for $A = 0.2086$ projected on the x_1, x_2 plane. This limit cycle is point-symmetric about $(x_1 = \pi, x_2 = 0)$ but as A is increased further the limit cycle breaks its point symmetry in a cyclic fold bifurcation before undergoing a period doubling cascade.

A comparative study was performed for this system for different values of the damping coefficient β. Bifurcation plots showing particle positions in the Poincaré sections versus the interaction amplitude A are given in fig. 4.8 for $\beta = 0.01$, 0.05, and 0.2, which are indicative of systems with very little damping, moderate damping and heavy damping, respectively. All of these plots exhibit the region IV stable propagating period-1 limit cycles and initial stability of the $\boldsymbol{r}_{fp1}$ fixed point at $x_1 = \pi$. In the cases of $\beta = 0.05$ and 0.2, the $\boldsymbol{r}_{fp1}$ attractor exhibits a period-doubling bifurcation, similar to that discussed above for the $\beta = 0.1$ case, followed by a sequence of bifurcations to a chaotic state. The $\beta = 0.01$ case, by contrast, does not appear to have a clear bifurcation of the $\boldsymbol{r}_{fp1}$ attractor. The next most evident difference

between the bifurcation diagrams is the number of trajectories that discontinuously appear and disappear as A is increased. For $\beta = 0.2$ we see fewer of these disconnected fixed points, one set being very similar to the fixed points associated with the limit cycles shown in fig. 4.7. Clearly the bifurcation sequence to the chaotic attractor, the chaotic state itself, and the higher velocity propagating trajectories are the dominate features in the larger β phase space.

We briefly continue our investigation past the first chaotic regime. We find that as we continue to increase A there are alternating arrangements of chaotic and non-chaotic solutions. In fig. 4.9a we show the next stable regime and its transition to chaos in a bifurcation diagram. In fig. 4.9b we show the chaotic attractor for $A = 1.7$ and the largest Lyapunov exponent for this value of the interaction amplitude is found to be $0.187 \pm .003$.

4.4.2 Two Dimensional Regime

In the $2D$ EC the additional force of gravity in the equations of motion make the system codimension 3. For the rest of this discussion we set $g = 0.1$ because for certain values of A and β it is found to produce results on a convenient dimensionless timescale that are similar to those discussed in the literature (69; 82; 83; 62; 84; 70; 23). It is worth clarifying this choice of g because it may seem that $g = 0.1$ and our choice of A values in the $1D$ EC section violate the inequality in Eq. (4.6). This issue is rectified by choosing the appropriate k and ω for the $1D$ EC where the ratio k/ω is quadratic in A and linear in g making it possible to balance A/g so that Eq. (4.6) is satisfied. We focus primarily on particle motion in the x, y plane for ease of comparison to previous and future experimental work

To begin the study of the two dimensional regime we fix the damping at $\beta = 0.1$ and then sweep through the interaction amplitude from $A = 0.1$ to $A = 25$. We use the same methods in making the bifurcation diagrams as those used in making the $1D$ EC bifurcation diagrams. Even when no bifurcating fixed points are found this methodology is an informative way to explore the $2D$ EC dynamics. In fig. 4.10a the final Poincaré sections used to make the diagram were projected onto the x axis and in fig. 4.10b the Poincaré sections were projected onto the y axis. In fig. 4.10a there are two red lines trisecting the diagram in the horizontal direction as well as a background of scattered points. The two red lines are asymptotically stable fixed points (attractors) in the Poincaré sections that exist for all A above $A \approx 0.3$. These fixed points in the Poincaré sections are located directly in-between the electrodes. In fig. 4.10b there is only one red line with the background of scattered points implying both fixed points are located at the same y for a given A. In fig. 4.10a it is also clear that the location of these fixed points increases in y as A is increased. The two fixed points are period-2 limit cycles. They do not contact the surface and they oscillate in both the x and y directions in an attempt to follow the curved electric field between two electrodes (field lines can be seen in fig. 2.3). Gravity provides a centripetal force for the curved oscillations. The particles oscillation height depends on the force of gravity, the time average force in y, and the inertial force from the particle following a curved path.

In fig. 4.10b the background of scattered points are seen to be restricted to a domain of y which depends on A. The scattered points are transient motion that takes a long time to completely die out for some initial conditions. For these parameters, as $t \to \infty$ all initial conditions are in the basin of attraction for one of the two attractors.

For $\beta = 0.05$ a strange attractor exists, shown for $A = 9.0$ projected onto the x and y phase planes in fig. 4.11 respectively. If a stable limit cycle can not exist because β is too small or A is too large then the only type of motion found is the strange attractor in fig. 4.11 or a qualitatively similar strange attractor. The strange attractor is robust for variations in A as it only grows (shrinks) in the y, $\dot{y}$ directions when A is increased (decreased). The largest Lyapunov exponent for $A = 9.0$ is 0.134 ± 0.003.

Even though independent variations of the damping are much more difficult to achieve experimentally we find that these variations produce slightly more interesting bifurcation diagrams. In fig. 4.12 we show x and y "bifurcation" diagrams for $A = 9.0$. In fig. 4.12a,b we show results for $\beta < 2.0$ and in fig. 4.12c,d we show results for $0.25 < \beta < 2.5$. Figure 4.12a starts with a background of scattered points coexisting with two fixed points between the electrodes which is maintained for $0.0 < \beta < 0.15$. For $\beta > 0.9$ the chaotic trajectory (fig. 4.11) drops out and only the stable fixed points exist until $\beta \approx 0.9$. For $0.9 < \beta < 1.1$ the fixed points quickly loose their stability to a brief period of what misleadingly appears as another chaotic regime (explanation below). For $\beta > 1.1$ two new stable fixed points are seen located in x at the position of the electrodes. In fig. 4.12b we only show the bifurcation diagram for $0.2 < \beta < 2.0$ in order to show the most important features. In this diagram a red line, representing the two initial stable fixed points at the same value of y, becomes unstable at $\beta \approx 0.9$. We then see more scattered points which are more localized in y than in x. Then two new fixed points appear out of the unstable region for $\beta > 1.1$. The two fixed points in y after $\beta \approx 1.1$ show that there are now four fixed points in the x, y plane. The two new fixed points located over each electrode represent a limit

cycle that oscillates almost entirely in y with a small x component oscillation as well. These are stable limit cycles of particles attesting to follow the field lines near the electrodes. The most notable feature of fig. 4.12b, however, is the apparent reverse bifurcation cascade beginning at $\beta = .29$ which we discuss in more detail at the end of this section.

The fixed points seen for $\beta < 0.9$ in fig. 4.12 are the Poincaré sections of the same type of stable limit cycle discussed for fig. 4.10. The instabilities arise at $\beta = 0.9$ because the particle can no longer maintain large oscillations that following the sharp curvature of the field directly between the electrodes. As the x component of their oscillations begins to damp out the time average force in x, which points towards the direction of constant potential (directly over the electrodes) begins to weaken the stability of the fixed points between the electrodes. The scattered points we see in fig. 4.12a for $\beta = 1.0$ are the result of the competing stabilities of the fixed points between the electrodes and the fixed points above the electrodes. This competition creates a regime where particles will oscillate about any point in x but only about specific values of y in an attempt to follow the local field oscillation. These fixed points in the Poincaré sections may be described as being asymptoticly stable in y and Lyapunov stable in x. Meaning that a particle oscillating at a some x will continue to oscillate about that location unless there is a small perturbation in x after which it will oscillate about its new perturbed location. By Contrast small perturbations in y of an oscillations will push the particle out of equilibrium and it will experience a restoring force back to its original position. The resulting attractor appears as a line in the Poincaré sections. As we continue to increase β past 1.0 the time average force in x begins to dominate particle behavior. The fixed points that become most

clear for $\beta > 1.1$ represents stable oscillations in y above an electrode. The particles settle at a height above the surface for which the time averaged force in y and g are balanced.

Figure 4.12c shows the only actual bifurcation sequence found for the $2D$ EC, but from fig. 4.12d we see that this is actually behavior for particles constrained to $1D$ motion in y directly above electrodes. For this range of β the time average force in x is not prevalent enough to prevent stable oscillations between the electrodes, as those are apparent in fig. 4.12c,d as well, but it is substantial enough to constrain the oscillations of particles near electrodes to motion directly above them. It is interesting to note the existence of such behavior in this model. We do not investigate it in any detail because observation of any such dynamical behavior in a stable reproducible way would be extremely difficult experimentally and has never been discussed in the literature.

4.5 Conclusion

We have studied the dynamics of a single particle in a 2-phase EC. We have separately considered the case of particle motion constrained to the surface of an EC for small interaction amplitude ($1D$ EC) and the case of particle motion above the surface when the interaction amplitude is sufficiently large to lift the particle off of the surface ($2D$ EC). We find a wide variety of possible stable limit cycles with different periodicities in the $1D$ EC and show the bifurcations of fixed points in the Poincaré sections for variations in A. For limit cycles in the $1D$ EC we calculate Floquet stability multipliers in order to analyze the transitions found in the bifurcation diagrams. We

show that in the $1D$ system it is possible to have different trajectories coexisting for the same values of A and β. In particular we find a chaotic trajectory that coexists with two asymptoticly stable propagating trajectories having $\pm\dot{x}$ velocities respectively. We also find that in the $1D$ EC a transition of a limit cycle in or out of stability can happen discontinuously over small variations in A. In general the number of these discontinuous trajectories is greater for smaller values of β. We find a very different picture in the $2D$ EC. Starting with the well known stable oscillations between two electrodes(23; 70; 82; 69; 59) we show how the height of this limit cycle depends on the interaction amplitude. In an interesting transition occurring for increasing values of β, the limit cycles looses its asymptotic stability in x and a line attractor in the Poincaré sections briefly describe particle behavior. Further increase of β leads to the asymptotic stability of $1D$ limit cycles in y located directly above the electrodes. In both the $2D$ and the $1D$ models, we find chaotic motion of particles for particular parameter values. However, the transition from stable limit cycles to chaos is fundamentally different in the two models. In the $1D$ EC a chaotic trajectory comes out of a period doubling cascade. In the $2D$ EC, the surface interferes with what would otherwise be a stable limit cycle and the result is chaotic motion.

By showing the general structure of particle dynamics for various values of the dimensionless parameters A and β, we develop a better understanding of how to induce and avoid certain types of particle behavior. We believe that the sensitivity of limit cycle periodicity on the interaction amplitude may be useful in particle sorting/separation applications. Particles with different charge-to-mass-ratios will fall into different regimes of the parameter space. Particles with charge-to-mass-ratios that place them in a regime of non-propagating stable motion (in either the $1D$ or

$2D$ EC) will be trapped by the EC. For example, a particle in the $1D$ EC could be trapped in the $\beta = 0.1$ and $0.0 < A < 0.26$ regime. The EC may be configured so that particles of a slightly different charge-to-mass-ratio exhibit chaotic behavior by falling into the $\beta = .1$, $0.27 < A < 0.33$ regime resulting in slow mitigation over time.

The 2-phase EC is an attractive candidate for many particle manipulation and control applications, especially for dust and particle mitigation(23). We have shown that there exists two dominate regimes of particle behavior in the $2D$ EC; one of which is stable oscillations, the other is chaotic. Therefore for EC mitigation applications it is necessary to understand the role of the surface as it is the primary instigator of non-stable particle trajectories. Mitigation efficiencies could be improved by an EC design in which most of the particles fall into chaotic motion. This can be done by tuning the EC parameters so that charge-to-mass-ratios of interest will exist in an area of the parameter space for which no stable motion is possible. For many real applications, we certainly would face a system of multiple particles. The analysis provided in this work is useful for a system of dilute particle density, for which the separation distance between particles is large enough that each particle's motion can be considered independent. While these results cannot be directly carried over to the case of more concentrated particle flows, they nevertheless provide and important step in understanding the dynamics of the 2-phase EC.

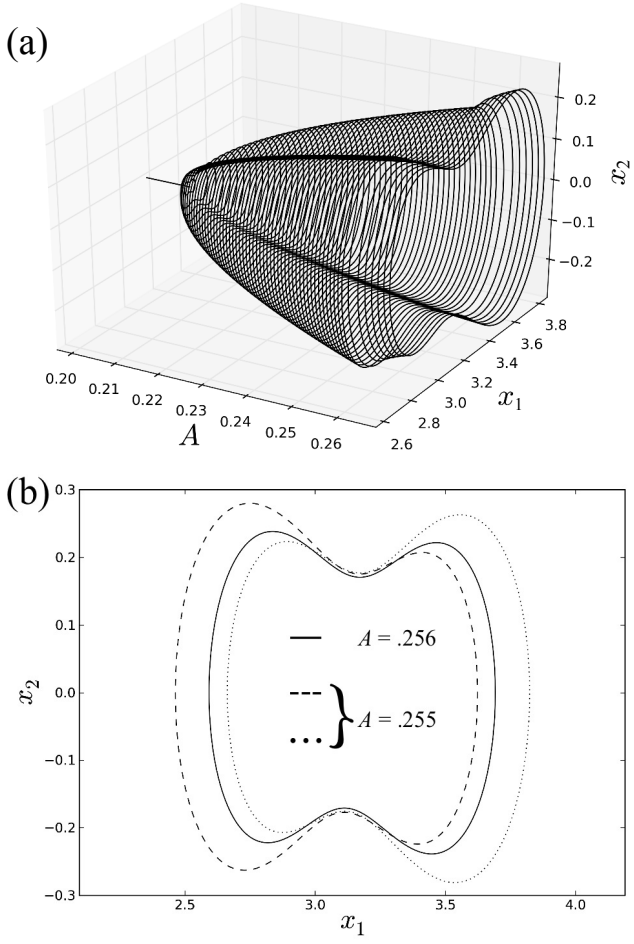

Figure 4.4: (a) projections of the full phase space onto the x_1, x_2 axes for a range of A that includes the first two bifurcations. The first being a supercritical flip bifurcation and the second being a cyclic fold bifurcation. (b) Solid line: Trajectory after supercritical flip but before cyclic fold. Dashed and doted lines: The two possible trajectories after cyclic fold.

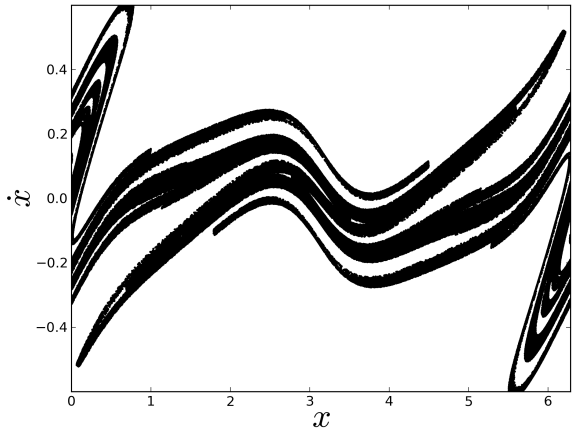

Figure 4.5: A Poincaré section of the strange attractor found when $A = 1.3$. The figure was made by letting a trajectory approach the attractor for a long time and then plotting successive Poincaré sections when it was assumed to be close if not in the attractor

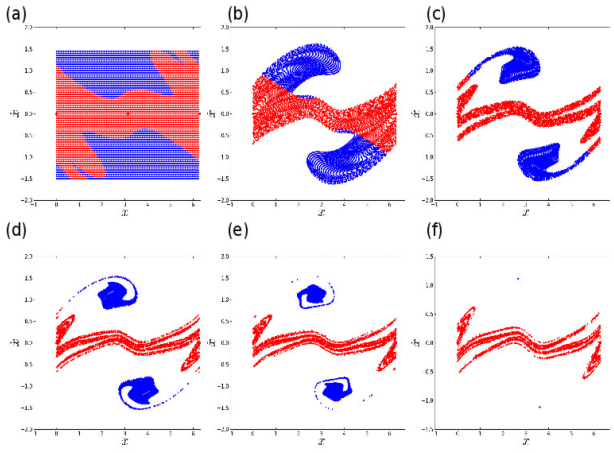

Figure 4.6: (a) Block $\boldsymbol{B}$ of initial conditions colored red if they are in the basin of attraction of the strange attractor and blue if they are in the basin of the coexisting fixed points. (b) $\boldsymbol{B}$ after time map $\boldsymbol{T}^1$. (c) $\boldsymbol{T}^2\boldsymbol{B}$. (d) $\boldsymbol{T}^3\boldsymbol{B}$. (e) $\boldsymbol{T}^4\boldsymbol{B}$. (f) $\boldsymbol{T}^{300}\boldsymbol{B}$.

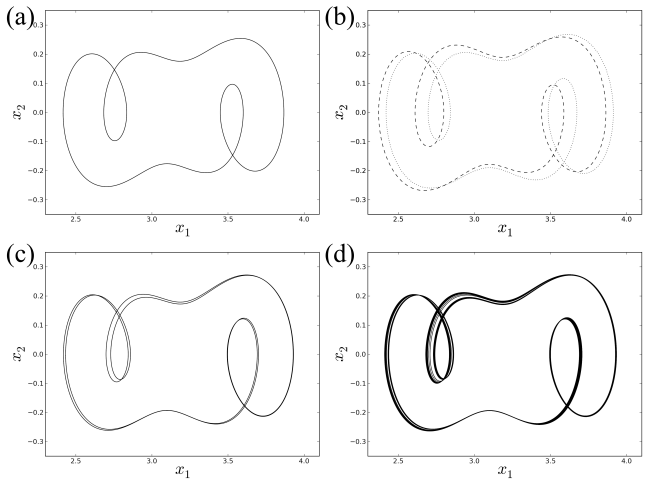

Figure 4.7: (a) A period-4 trajectory that creates the initial region VII (4.2) fixed points. (b) The two possible period-4 trajectories after a cyclic fold bifurcation distinguished by the dashed and doted lines. (c) After the doted line in (b) undergoes a supercritical flip and its period doubles. (d) The result of more period doubling bifurcations.

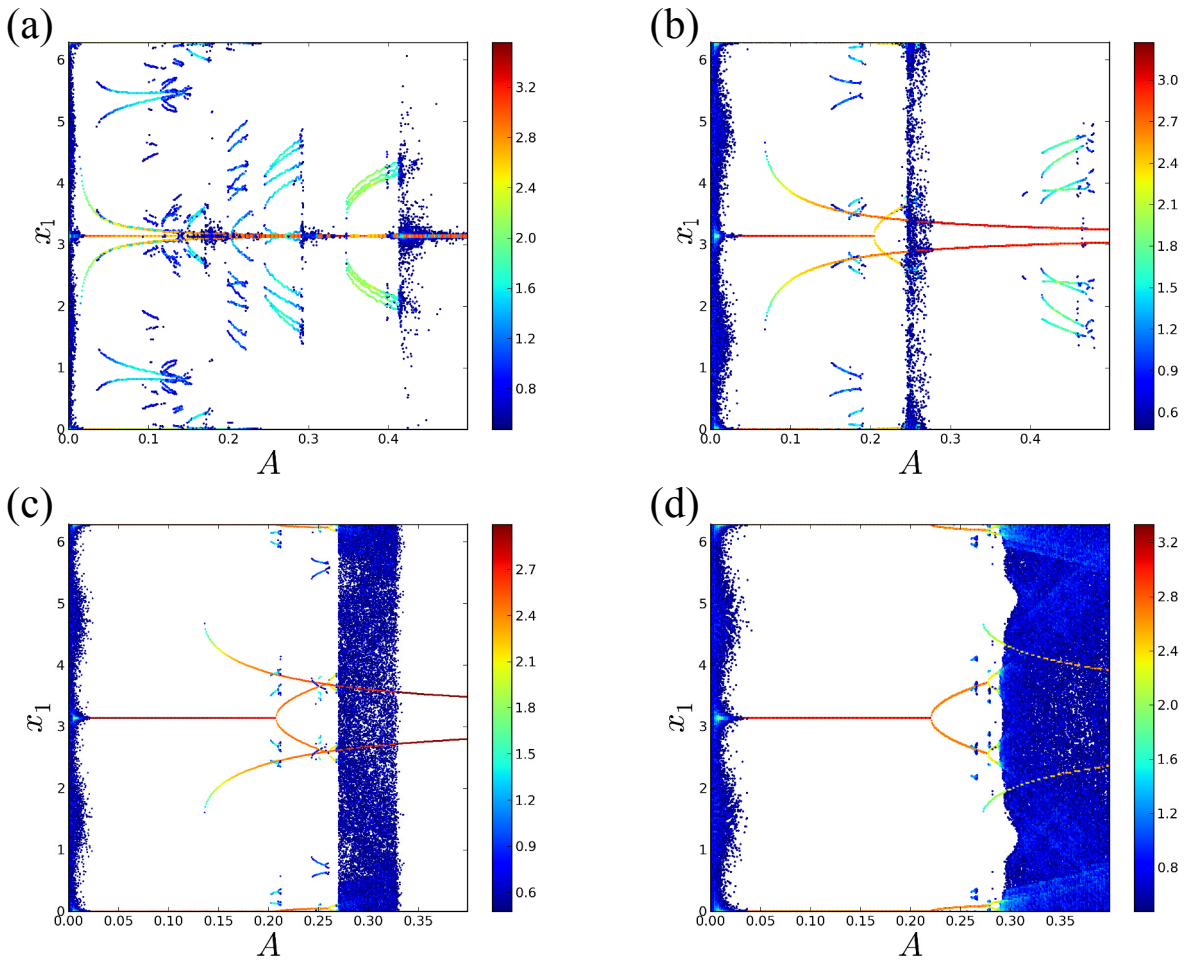

Figure 4.8: Bifurcation diagrams computed using the same methods as in fig. 4.2. (a) $\beta = 0.01$. *(b)* $\beta = 0.05$. *(c)* $\beta = 0.1$. *(d)* $\beta = 0.5$.

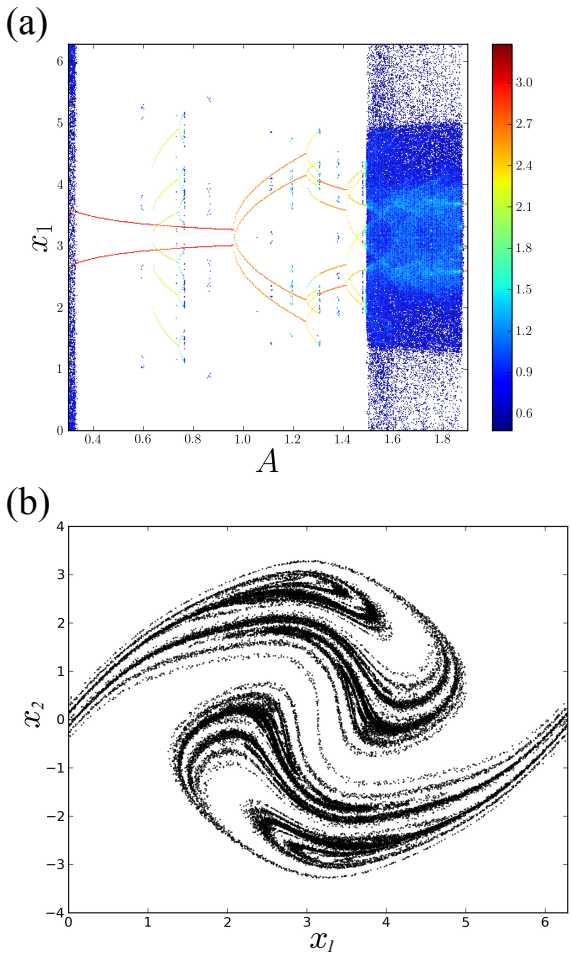

Figure 4.9: (a) bifurcation diagram for the second range of stable motion as well as a transition to a second chaotic regime. (b) The chaotic attractor found for $A = 1.7$.

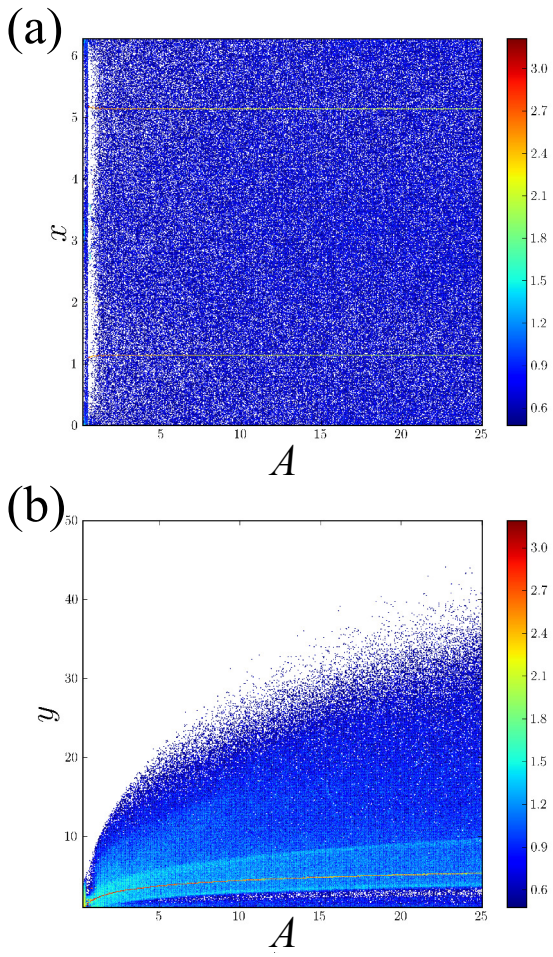

Figure 4.10: Bifurcation diagram for $\beta = 0.1$ made with same methods as 4.2 with projections of the final Poincaré section onto the (a) x axis and (b) the y axis.

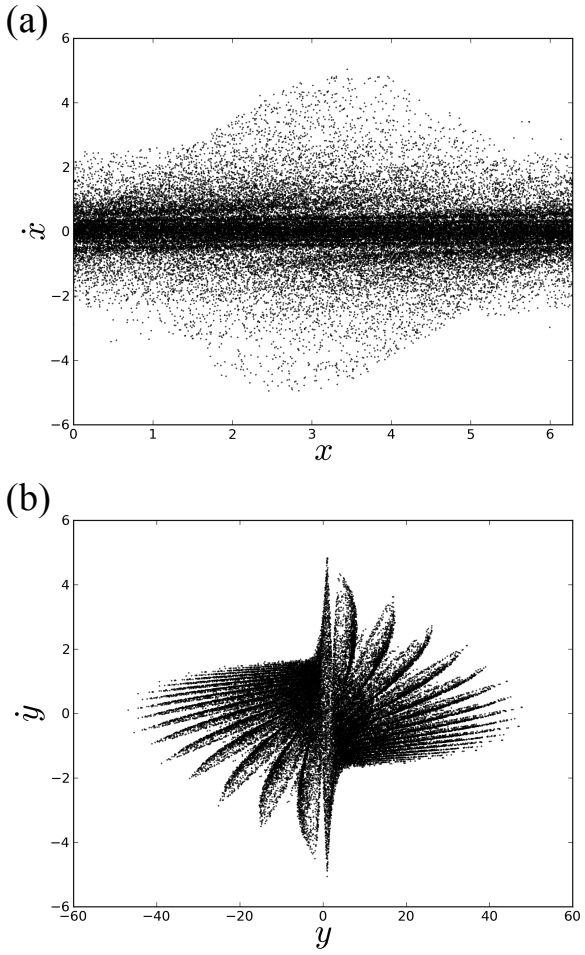

Figure 4.11: Poincaré section of the chaotic attractor found in the 2D EC phase space for $A = 9.0$ and $\beta = 0.05$ plotted onto the (a) $x, \dot{x}$ plane and (b) $y, \dot{y}$ plane where we have mapped Poincaré sections after odd numbered reflections from the surface to below the surface in order to see the structure of the strange attractor more clearly. Made with same method as 4.5.

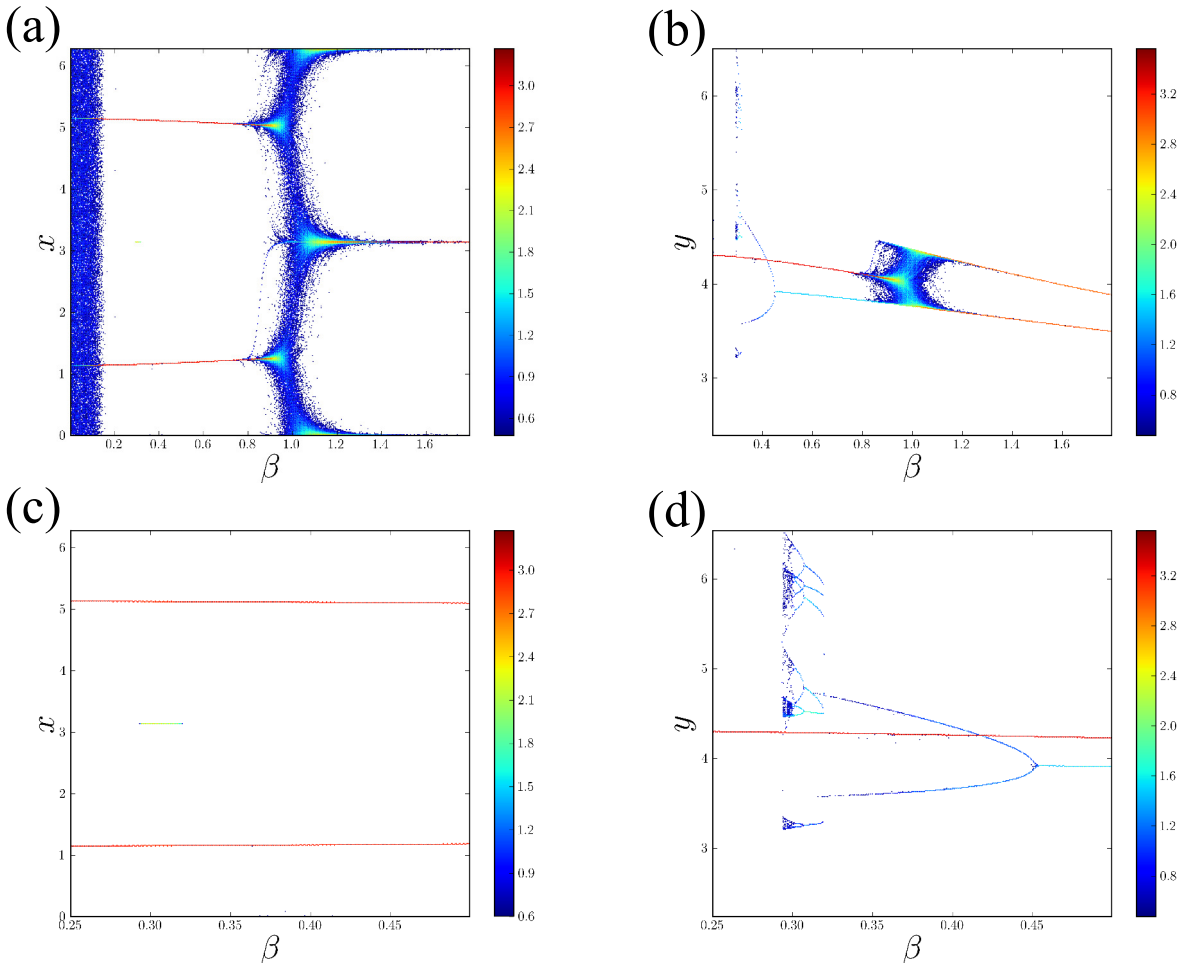

Figure 4.12: Bifurcation diagram for variation in β with $A = 9.0$. Final Poincaré sections projected on to (a) x axis $0.0 < \beta < 1.8$, (b) y axis $0.2 < \beta < 1.8$. In (c) (projections onto x axis) and (d) (projections onto y axis) we show bifurcation diagrams for $0.25 < \beta < 5$ to highlight the reverse bifurcation sequence.

Chapter 5

Dynamics of Multiple Particles with long-range interactions in a STP

5.1 Introduction

The interesting behavior of the Kapita pendulum, the stable inverted position, has enticed several researchers to study the nonlinear case both experimentally (85; 86; 87) and numerically (88; 89; 72; 90; 91; 92; 86). For systems composed of particles in a STP potential, only a small number of publications have examined the nonlinear multiple particle dynamics accounting for the multi-particle interactions. Some examples of papers treating this subject include a study of the motion of hydrophobic/hydrophilic particles on the surface of Faraday waves (4; 5), multiple charged particles in an STP potential generated by an electric curtain (83; 93; 94), and multiple particles in a periodically forced straining flow (95). These previous studies have considered very large numbers of particles and they have focused on the overall particle motion. In the current work, we instead examine the dynamics of a relatively

small number of particles in a STP potential using a dynamical systems point of view. Specifically, we seek to relate the nonlinear systems dynamics with multiple particles to the bifurcations and stability of single particles.

5.2 Methods

The current computational study examines a one-dimensional (1D) system with multiple particles interacting through a repulsive electrostatic $1/r$ potential in an external STP potential field. The STP potential is

$$\Phi = -A \cos x \cos t, \tag{5.1}$$

which produces equations of motion analogous to the parametrically driven pendulum in the horizontal plane. The coefficient A is the potential amplitude, and the distance coordinate x and time coordinate t are non-dimensionalized using the wavenumber k and the STP driving frequency ω, respectively.

The driving force ($F_\Phi = -\nabla\Phi$) has the form of a standing wave with oscillation amplitude A. The dimensionless wavelength λ and the oscillation period T are both equal to 2π. The system is assumed to be periodic over $n\lambda$, where n is an integer, so we can define the concentration σ as N/n where N is the number of particles in the simulation. For simplicity, all particles are assumed to carry the same charge and mass, where the non-dimensionalization is performed such that the dimensionless mass is equal to unity. Damping is proportional to particle velocity with a dimensionless damping coefficient β. In the current work, we focus on the effect of the parameter A, and therefore maintain constant values of the other dimensionless pa-

rameters - the damping parameter and the dimensionless particle charge. These latter two parameters are set equal to $\beta = 0.6$ and $q = 1$ throughout this chapter. These values for β and q are chosen because they are realistic for systems similar to those discussed in (83; 93; 94), after being dimensionalized.

The force on a particle located at x_i imposed by a particle located at x_j, denoted by F_{ij}, is calculated with periodic boundary conditions. To address the forces imposed by long range interactions, we consider an infinite sequence of image systems using Ewald summation method (96), giving

$$F_{ij} = \frac{q^2 r_{ij}}{\|r_{ij}\|^3} + q^2 \sum_{\nu=0}^{\infty} \frac{1}{(2\pi\nu - r_{ij})^2} - \frac{1}{(2\pi\nu + r_{ij})^2}, \tag{5.2}$$

where $r_{ij} = x_i - x_j$. The sum in (5.2) is convergent and may be written as a polygamma function $\psi^m(z)$ with series expansion

$$\psi^{(m)}(z) = (-1)^{m+1} m! \sum_{\nu=0}^{\infty} \frac{1}{(z+\nu)^{m+1}}. \tag{5.3}$$

Using (5.3), we can express F_{ij} as

$$\begin{aligned} F_{ij} = {} & \frac{q^2 r_{ij}}{\|r_{ij}\|^3} - \left(\frac{q^2}{n\lambda}\right)^2 \\ & \times \left(\psi^{(1)}(1 + r_{ij}/\lambda) - \psi^{(1)}(1 - r_{ij}/\lambda)\right) \end{aligned} \tag{5.4}$$

The equation of motion for the i^{th} particle is given by

$$\ddot{x}_i = -\beta \dot{x}_i + F_\Phi + \sum_{j \neq i}^{N} F_{ij} \tag{5.5}$$

where the second term on the RHS is due to the imposed STP potential field and the third term on the RHS is the particle interactions. An example of the system containing seven particles may be found in Fig. 5.1 (multimedia view).

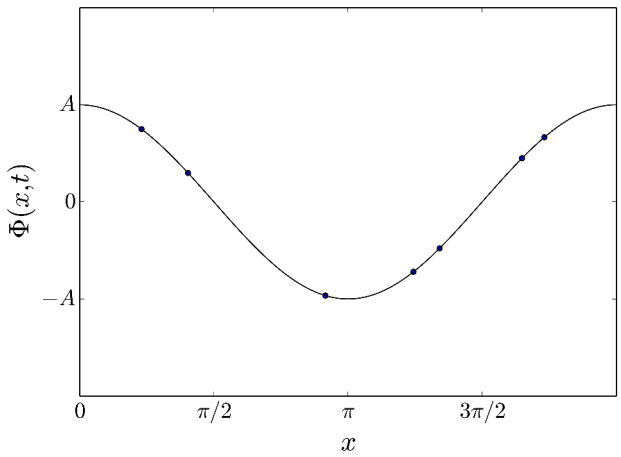

Figure 5.1: Example of the system with $N = 7$ and $A = 2.758$, depicted as particles on the surface of a standing wave (multimedia view).

5.2.1 The Phase Space

For N particles in an autonomous system, the degrees of freedom (or dimension) of the phase space is $2dN$, where d is the dimension of the physical system. In STP problems, there is an explicit time dependence in the potential and therefore the system is non-autonomous. Non-autonomous systems may be transformed into autonomous form by introducing an extra degree of freedom, which in a first-order system is given by $x_3 = t$. Though this seems to be a trivial representation of time, this autonomous formulation is necessary when distinguishing types of bifurcations. This augmented system thus has $2dN + 1$ degrees of freedom, which constitutes the "full phase space".

5.2.2 Poincaré Sections

The standard choice for making Poincaré sections in driven systems is a time map taken at the system driving period. Time maps are stroboscopic views of a trajectory expressed as $x(t = 2\pi n)$ when n is a positive integer. A Poincaré section includes any point where a continuous trajectory transversely intersects a subspace of the full phase space (37). Time maps, as defined above, will produce Poincaré sections with dimension one less than the dimension of the full phase space. In a time map, the path of a particle is always transverse to the $x - \dot{x}$ plane, and therefore a point of intersection of the trajectory with this plane is a convenient sub-space that satisfies the criterion necessary to be a Poincaré section.

5.2.3 Kinetic Energy Fluctuations

It is well known that as a system approaches a bifurcation point, it may take longer for transients of the relevant quantity to die out or for the system to recover from an external perturbation (97). This behavior is known as the critical slowing down phenomena. Most real systems are subject to some natural perturbations, and these perturbations can become particularly apparent near the bifurcation points. Measuring the increase of the variance in a physical quantity can therefore be used as a method to predict the presence of a bifurcation point (97). The model system considered here has no external perturbations, aside from computer round-off error. In the limit $t \to \infty$, the damped system would be expected to settle into an attractor, but the finite time of real simulations ensures the presence of small fluctuations in "residual" transients. In other words, multiple particle systems have a "large" num-

ber of degrees of freedom, therefore some small trace of the initial transient behavior (residual transients) will most likely be detectable. The amount of residual transients may be found in the kinetic energy fluctuations. It is known that the kinetic energy fluctuations may contain some information about the "effective number of degrees of freedom" (98). The more degrees of freedom, the more residual transients will be present. This correspondence between the effective degrees of freedom and the kinetic energy fluctuations is what makes the kinetic energy fluctuations an interesting quantity to examine.

The square of the deviation of the particle kinetic energy is given by $(\Delta KE)^2 \equiv \langle KE^2 \rangle - \langle KE \rangle^2$,

$$(\Delta KE)^2 = \frac{1}{4} \sum_{i,j}^{N} (\langle v_i^2 v_j^2 \rangle - \langle v_i^2 \rangle \langle v_j^2 \rangle), \tag{5.6}$$

and v_i, v_j denote the i^{th} and j^{th} particle velocities, respectively. The average is calculated as $\langle KE \rangle^2 = \frac{1}{4} \sum_{i,j}^{N} \langle v_i^2 \rangle \langle v_j^2 \rangle$. The normalized squared deviation of the kinetic energy is given by

$$\delta_{KE} \equiv \frac{\Delta KE}{\langle KE \rangle^2}.$$

5.3 Results

5.3.1 Single Particle Overview

The dynamics of a single particle immersed in the one-dimensional STP potential Φ, given by (1), are similar to the dynamics of the parametric pendulum. In this

chapter, we only discuss dynamics for the first bifurcation sequence leading to the chaotic regime, even though there are many consecutive regimes of stable limit cycles bifurcating into chaotic trajectories. In Fig. 5.2, the first bifurcation sequence is shown for an ensemble of initial conditions. Table 5.1 lists the type of bifurcations, the critical values of A at which each bifurcation occurs, and the period of the limit cycle following each bifurcation. The table is truncated after the 6^{th} bifurcation due to numerical resolution limitations for distinguishing bifurcation onset in a small volume of the phase space. For $0 < A < A_{c1}$, a particle will move toward and equilibrate at the antinodes of the potential $\Phi(x,t)$ (i.e., the maxima of $\cos x$). As A is increased, the fixed points in the Poincaré section bifurcate in a supercritical flip bifurcation leading to a period-2 limit cycle for $A_{c2} < A < A_{c3}$. This transition is not a Hopf bifurcation because the explicit time dependence in the equations of motion must be considered as a degree of freedom to the phase space. Consequently, what might appear as a fixed point in the $x - \dot{x}$ phase space in a bifurcation diagram is actually a period-1 trajectory in the full phase space. We prove this using Floquet theory, by numerically calculating the stability multipliers. Both of the two non-trivial stability multipliers have no imaginary component close to the bifurcation point. At the bifurcation, one stability multiplier becomes smaller than -1 while the other remains close to zero, indicating a period-doubling supercritical flip bifurcation. This stability multiplier passing through -1 is shown in Fig. 5.3a, where it is denoted with a Roman numeral I. The values of A for which the first six bifurcations occur, shown in Table 5.1, indicate a period-doubling cascade route to chaos. The computed values yield a Feigenbaum constant of 4.00 with an upper error bound of 6.00 and a lower bound of 2.89. The accepted value of 4.669 for period-doubling bifurcations (36) is within the

error bounds. The Feigenbaum constant $\mathcal{F}$ is evaluated with

$$\mathcal{F} = \lim_{n\to\infty} \frac{A_{cn-1} - A_{cn-2}}{A_{cn} - A_{cn-1}} \tag{5.7}$$

where A_{cn} is the n^{th} critical value of A for which a period-doubling bifurcation occurs. The two lines coming out of the chaotic region in Fig. 5.2 are each attractors representing stable propagating trajectories, one with a positive velocity and one with a negative velocity. These propagating trajectories travel across λ once per period of the driving potential field.

Table 5.1: Bifurcations

A_{cn}	Bifurcation	$A \pm 5e-5$	New Period
A_{c1}	Supercritical Flip	0.75365	2
A_{c2}	Cyclic Fold	0.91875	2
A_{c3}	Supercritical Flip	0.94985	4
A_{c4}	Supercritical Flip	0.95650	8
A_{c5}	Supercritical Flip	0.95790	16
A_{c6}	Supercritical Flip	0.95825	32

5.3.2 Kinetic Energy Fluctuations of One Particle

Before going to the multi-particle case, it is informative to compare the bifurcation diagram (Fig. 5.2) to the calculation of δ_{KE} for a single particle, which is shown in Fig. 5.3. We also show a Floquet stability analysis of the fixed point at $x = \pi$ through A_{c1} for comparison. Floquet stability analysis is a powerful tool in analyzing bifurcations, but it is not easily applied to multiple particle systems. It has been

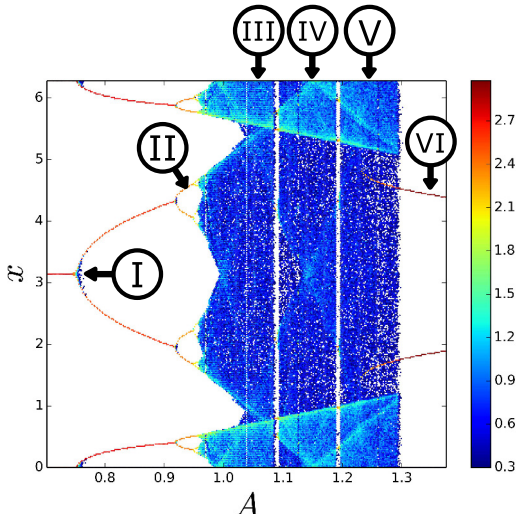

Figure 5.2: Bifurcation diagram formed by taking a two-dimensional histogram (300×300 *bins) of the final Poincaré section of 1830 trajectories with different initial conditions for 300 different values of A. The gray scale (color online) represents the base 10 logarithm of the number of particles in a bin. The Roman numerals are listed here for comparison with* δ_{KE} *shown in Fig. 5.3.*

applied to coupled Kapitza pendulums by (99). For a description of single particle stability analyses, we refer the reader to (72) and (100), which are both studies of similar systems and use the Floquet technique to study bifurcations. In Fig. 5.3a, the real and imaginary components of the stability multiplier that causes the bifurcation (one of the two complex Floquet stability multipliers λ_1 and λ_2) are plotted as A is increased through A_{c1}. In Fig. 5.3b, δ_{KE} is plotted as A is increased through the full range shown in the bifurcation diagram in Fig. 5.2.

In Fig. 5.2 and Fig. 5.3, the key regions associated with different system behaviors have been identified using Roman numerals. For small values of A, Fig. 5.3b shows a wide range of scattered points. However, the particle exhibits very little motion within this range of small A values. As A is increased, there exists a peak in the fluctuations near A_{c1}, which is a consequence of the critical slowing down phenomenon (region I).

As A is increased past A_{c1}, the fluctuation amplitude is relatively constant until A approaches A_{c2}, where a kink is observed (region II). When A is in the chaotic and near-chaotic regimes (regions III,IV,V), the fluctuations increase in amplitude and are irregular, as shown in the inset in the figure. The two regions where the fluctuation amplitude decreases markedly in this inset correspond to the two periodic windows seen in Fig. 5.2. At the end of the chaotic regime, there is a discontinuous jump in the fluctuations to a comparatively small and relatively constant value (region VI). This last section shows the transition to propagating trajectories, and we will see that this feature is present in all cases where this transition occurs. Under closer inspection, region VI overlaps with region V because, just as in the bifurcation diagram, the propagating trajectories exist simultaneously with the chaotic regime for a small range of A.

5.3.3 Integer Concentrations

The bifurcation diagrams for multiple interacting particles, with $N = 2, 3, 4, 5, 6, 7$, are shown in Fig. 5.4. The increased degrees of freedom that occur for $N > 1$ make it difficult to investigate an ensemble of initial conditions that exhaustively fill the phase space. We use random positions distributed with even probability across x (with $\dot{x}(0) = 0$) as initial conditions for each run to explore a set of possible initial conditions. The bifurcation plots are made by taking the last Poincaré section after 150 driving cycles of a simulation, projecting it onto the position axis, and then plotting the positions against the value of A used in that simulation. For very small A, the final Poincaré sections are scattered because, for these values, transients die out very slowly. For larger A, there are clearly defined points in the Poincaré sections

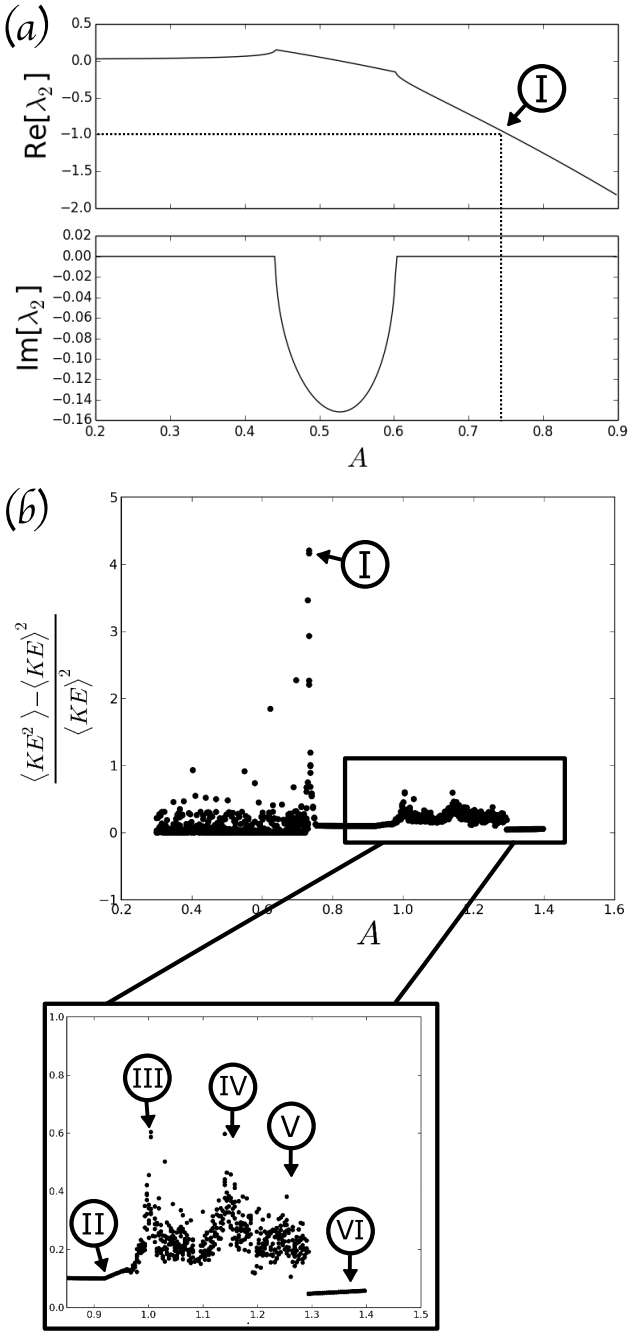

Figure 5.3: Single particle: (a) One of the two Floquet stability multipliers for the $x = \pi$ fixed point as a function of the potential oscillation amplitude as it is increased through the first bifurcation point. (b) Kinetic energy fluctuations. Roman numerals for comparison with the bifurcation diagram in Fig. 5.2

that denote limit cycles in the full phase space. For the rest of the chapter, the stable limit cycles in the Poincaré sections are referred to more generally as attractors. At first glance, Fig. 5.4 appears to indicate a larger number of particles for odd values of N than it does for even values of N. As A is further increased, a bifurcation occurs for all the cases shown, although it is difficult to see in Fig. 5.4(e). For other values of A, the diagrams in Fig. 5.4 appear as scattered points, implying either chaotic motion, high-period trajectories, or motion on a torus (after a Neimark bifurcation). Past this scattered regime, the system collapses into a new stable regime that is qualitatively similar to the propagating trajectories that occur after the chaotic regime in the single particle case.

The discrepancy between the number of possible attractors for odd and even values of N can be explained by considering the relationship between the number of particles and the number of antinodes in one period of the potential. For the trajectory $(x_1(t), ..., x_{2dN}(t))$, the number of attractors that are observed for values of A before the first bifurcation is equal to the number of particles when N is even and twice the number of particles when N is odd. In other words, there is one possible final state configuration of the whole system when N is even and two possible final state configurations of the system when N is odd. To see why this occurs, we examine in detail the cases of three and four particles per period. Figs. 5.5(a)(b) and (c)(d) show cartoons of the final particle configurations for cases $N = 4$ and $N = 3$, respectively. In these cartoons, the particle position in the periodic domain is drawn as an angle, so that motion of the particle in the x domain corresponds in the figure to rotation about a circle. The intersection points of the circle with a horizontal bisection line occurs at the antinodes of the potential Φ. In this figure, at least one particle can always

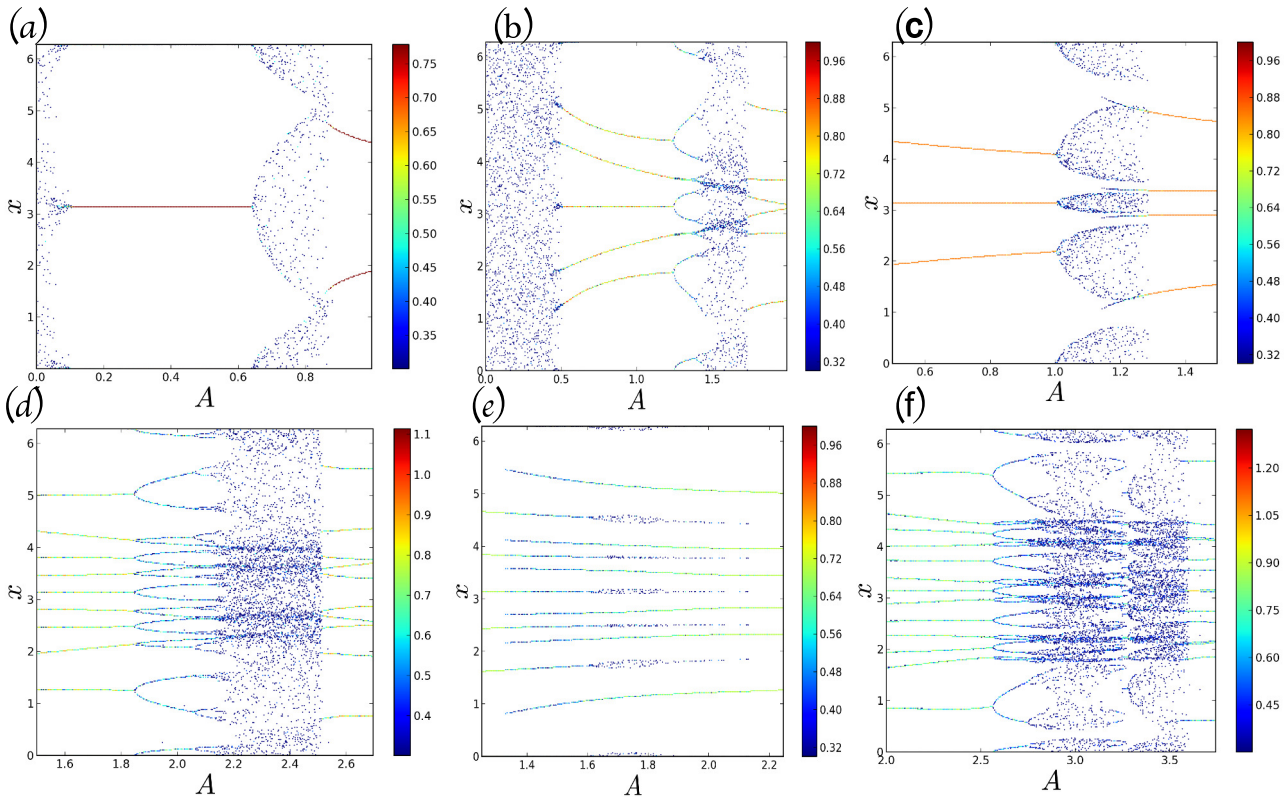

Figure 5.4: Multiple particle bifurcation diagrams made by: (1) initializing particles at random initial positions with $\dot{x}(0) = 0$, (2) projecting the Poincaré section onto the position axis after 150 cycles and plotting against the value of A, and (3) repeating the process for 400 values of A in the range of interest. The number of particles used in each bifurcation diagram is (a) $N = 2$, (b) $N = 3$, (c) $N = 4$, (d) $N = 5$, (e) $N = 6$, (f) $N = 7$. Note that the range of A values explored differs in each figure.

be found at the antinode of Φ. From the single particle case, we know the antinodes can act as attractors, where individual particles remain motionless in the $x - \dot{x}$ phase plane. In the case of four particles, shown in Fig. 5.5(a), two particles may occupy the antinodes of Φ and the other two particles oscillate about the nodes of Φ. One might imagine that a rotation of this configuration by $\pi/4$ (shown in Fig. 5.5(b)) might be a fixed point in the Poincaré section of the full phase space, and indeed it is, but it is not a stable configuration and, unless perfectly configured, it will collapse into the configuration shown in Fig. 5.5(a). For three particles, one particle sits at either antinode and the two remaining particles compete over the other antinode, as shown in Fig. 5.5(c) and (d). Which antinode a particle is attracted to depends on the initial conditions. In both the four and three particle cases, the particles at the antinodes are stationary.

Drawing lines between the adjacent average particle positions in the circular topology creates a regular convex polygon inscribing the circle. From our description of the particle behavior above, at least one vertex of the polygon must be at an antinode. For a regular polygon inscribing the circle with an even number of vertices, each antinode may touch a vertex and it is symmetric under all rotations obeying this rule. For a polygon with an odd number of vertices, however, only one vertex can occupy an antinode so that rotations by π/N flip the symmetry about a line vertically bisecting the circle. There are always two unique possible stable configurations when N is odd, but only one when N is even. This picture changes for even values of N when $N > 6$. For $N > 6$, the stable configuration no longer occurs for a pair of particles located at each antinode, but rather for pairs oscillating on either side of the antinodes much like what is shown in Fig. 5.5(b) but with an extra particle on the top and bottom

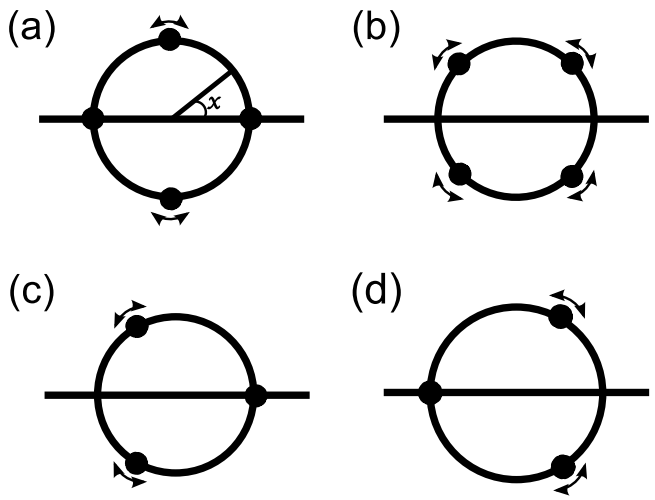

Figure 5.5: The position along the periodic domain is indicated by an angle around a circle. The black dots represent average particle positions before the first bifurcation. The line bisecting the circle passes through the two antinodes of the potential field. Part (a) shows the $N = 4$ stable configuration which is an asymptotically stable fixed point in the Poincaré sections of the full phase space. Part (b) is an $N = 4$ unstable configuration which is the unstable fixed point in the Poincaré sections of the full phase space. Parts (c) and (d) show two different possible stable configurations for $N = 3$, both of which are stable fixed points in the Poincaré sections of the full phase space.

of the circle.

In Fig. 5.6, the value of A at which the first bifurcation occurs is plotted as a function of N, with separate lines for N even (red squares) and N odd (blue triangles). A striking characteristic of Fig. 5.6 is that between $N = 6$ and $N = 8$, there is a cross-over point at which the even N line jumps upward and crosses through the odd N line. This sudden jump in the even N line between $N = 6$ and $N = 8$ occurs due to a change in type of first bifurcation. The first bifurcation when $N = 6$, as well as the first bifurcations for all lower even values of N, are Neimark bifurcations (a.k.a bifurcation to a torus) in which N stability multipliers cross the unit circle with nonzero imaginary components. Half of those stability multipliers ($N/2$) that cross the unit circle have positive imaginary components and the other half have the complementary negative imaginary components. For $N = 8$ and all higher even values of N, the first bifurcation becomes a cyclic fold bifurcation, although the bifurcations for odd values of N remain supercritical flip bifurcations.

We can qualitatively understand the transition which occurs when N is changed from six to eight in Fig. 5.6 by observing how the bifurcation diagrams, and therefore the stable attractors, depend on the particle number. In Fig. 5.4(e), after the first bifurcation, the particle motions are quenched by the presence of other attractors. For the sake of discussion we distinguish the two competing sets of attractors based on whether they are found at the far left or far right edges of the diagrams respectively. Comparing the cases of $N = 2$, $N = 4$ and $N = 6$ in Fig. 5.4 we see similar rightmost attractors that appear abruptly at different values of A in each case. As N (even) increases, the rightmost attractors increasingly impinge on the leftmost attractors. This impingement is responsible for the crossing of the lines in Fig. 5.6. When

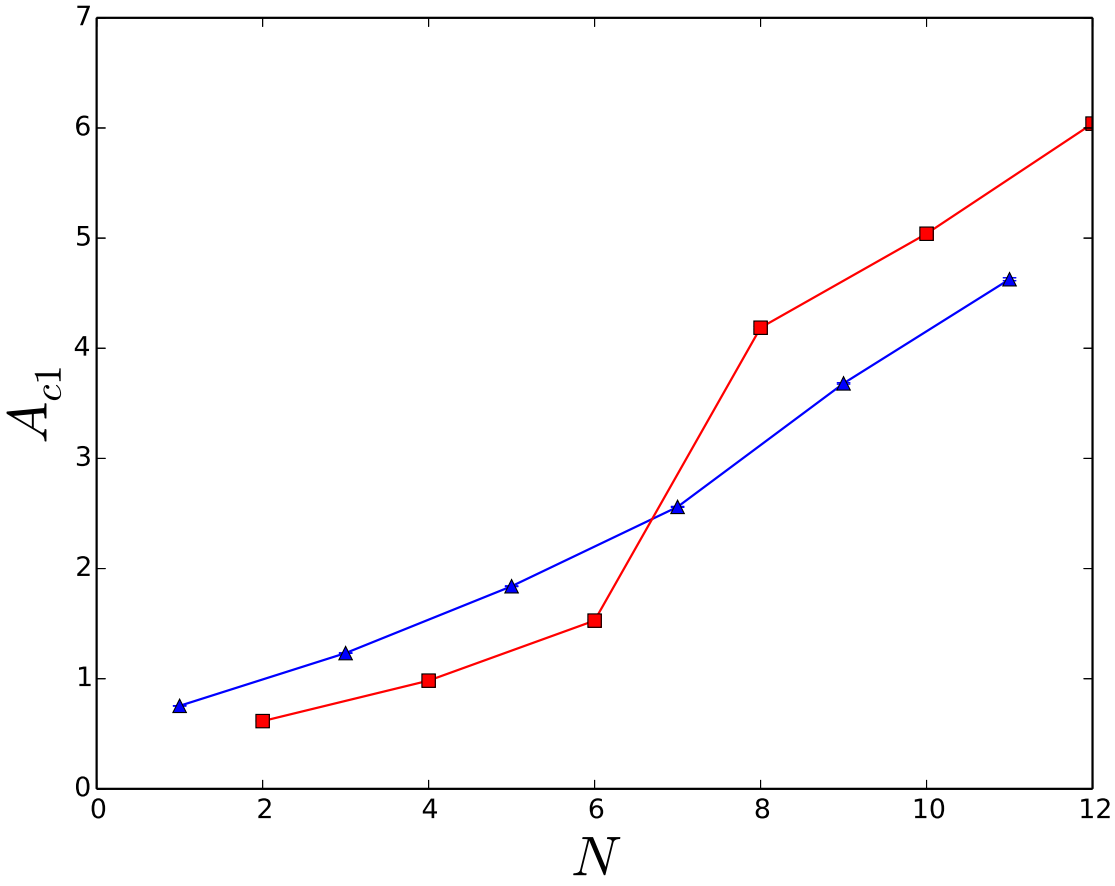

Figure 5.6: A plot of the value of A at which the system first bifurcates (A_{c1}) as a function of the number of particles in simulation (N). Even particle numbers are shown with red squares and odd particle numbers are shown with blue triangles (color online). A cross-over between the N odd and N even curves occurs between $N = 6$ and $N = 7$, which corresponds to the first bifurcation for the even value of N changing from a Neimark bifurcation to a cyclic fold bifurcation. The N odd bifurcations are all supercritical flip bifurcations for the values of N shown here. The upper (lower) error bound is the value of A which we are certain is after (before) the bifurcation. The error bounds are seen to be quite small in the Figure.

N increases from six to eight, the rightmost attractors extinguishes the left most attractors and becomes the first available attractors for $N \geq 8$ (even). These new first attractors, previously the rightmost, represents a fundamentally different type of limit cycle in the full phase space than what was previously first available. Therefore when this attractor first bifurcates, it falls outside of the original progression, causing the jump in A_{c1} as N is changed from six to eight shown in Fig. 5.6.

For all of the cases shown in Fig. 5.4, the system eventually collapses back into clearly defined attractors which have the form of "propagating" trajectories, as was also observed for the single particle case. These attractors display non-zero net particle motion of one particle when N is odd, but no net motion when N is even. The particles travel in either the $\pm x$ direction before a collision-like event. After the "collision", they travel in the opposite direction having exchanged some kinetic energy with the particle with which the collision occurred. When N is odd the transport of one particle occurs either in the $\pm x$ direction depending on the initial conditions. There is no possible counter-propagating particle pair for one of the particles with N odd.

In Fig. 5.7, the squared fractional deviation of the kinetic energy δ_{KE} is plotted for all of the bifurcation diagrams shown in Fig. 5.4. These plots all exhibit a discontinuity at the point corresponding to transition to a state with the propagating trajectories. The discontinuity is not as clear in Fig. 5.7(e) because (as can be observed in the corresponding bifurcation diagram Fig. 5.4(e), the propagating trajectory begins before the first bifurcation. In Fig. 5.7(e), the curve starting below and crossing at $A \approx 1.75$ indicates the values of δ_{KE} for the propagating trajectory.

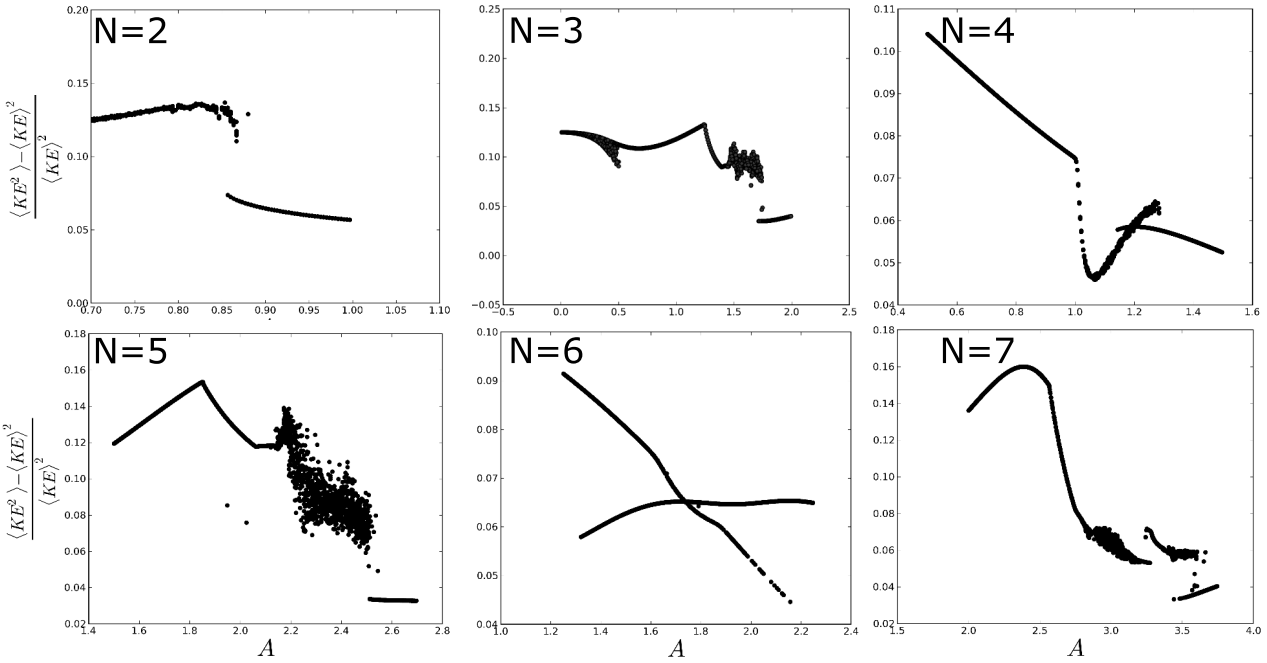

Figure 5.7: Kinetic energy fluctuations for various particle counts.

5.3.4 Scaling

When the periodicity of the system is increased ($n > 1$), two distinctly different possibilities exist. One possibility is an integer concentration, over a larger periodic system (e.g. $n = 2$ and $N = 4$: $\sigma = 2$). The second possibility is a fractional concentration (e.g. $n = 2$ and $N = 3$: $\sigma = 1.5$). When considering long-range particle interactions, it is reasonable to assume that increasing the system size might change the dynamics even if the concentration is held fixed. The first possibility above, results in system dynamics very similar to those discussed in this chapter, whereas the second possibility would result in a completely different symmetry of the system having very different dynamics. The effect of period number n on the system dynamics was examined in the current study by running simulations of equal

concentration over larger system sizes (i.e., large values of n). The system dynamics in these larger systems is observed to be qualitatively the same as for the smaller system sizes reported, although the exact values of A for which bifurcations occur is observed to change slightly. We find that for concentrations larger than two, the effect of scaling the system size while maintaining the concentration is negligible even when comparing critical A values.

5.4 Conclusion

We investigate the dynamics of multiple particles with long-range interactions in a STP system by examining Poincaré sections and fluctuations of the kinetic energy (δ_{KE}) for different numbers of particles. Our results are fundamentally interesting because of their importance in understanding complexity in time-dependent systems. The possible dynamics that exist in a wide range of different system configurations make the problem challenging, but even in the small area of the parameter space that we discuss, we have found a variety of interesting dynamics. For instance, it is shown that the particle number N influences the stability and the number of possible final states in a system having integer concentrations. The possible limit cycles of the system are shown to be sensitive to whether N is even or odd, and the influence of theÂ particle number on theÂ type of bifurcation is discussed. The squared fractional deviation kinetic energy is examined as a function of the potential amplitude ($\delta_{KE}(A)$), and it is found to exhibit interesting features at and near transition points. In particular, discontinuities in $\frac{d(\delta_{KE})}{dA}$ and δ_{KE} mark transitions between oscillatory and propagating modes, respectively. The measure δ_{KE} may be useful for future

experimental investigations of these systems.

Our work has demonstrated interesting and complex behaviors of multiple particles with the Coulomb interaction in a STP potential. In particular, the dynamics of the system is sensitive to particle concentration and the dynamics can be described by the squared fractional deviation of the particle kinetic energies. The latter is particularly valuable for studying bifurcations in real systems. For example, in the aforementioned studies of the motions of hydrophobic/hydrophilic particles on the surface of Faraday waves, the particles will interact due to capillary forces caused by their distortion of the local surface of the water, rather than through the Coulomb interaction, which leads to particle clustering (3). It may be convenient to study this type of behavior using the squared fractional deviation of the systems kinetic energy because this measure will decrease in the event of clustering as it measures the effective number of degrees of freedom (98).

Studies of multiple charged particles in a standing-wave electric curtain and in acoustic waves are also important areas of research for applications of dust-particle mitigation, e.g., from a solar panel (93). Charged particles interacting in standing-wave electric curtains and standing-wave acoustic fields exhibit complicated dynamics that may be illuminated by studying the squared fractional deviation of the particle kinetic energy. For example, in (101) it was observed that for charged particles in a standing-wave acoustic field, relative motion of smaller particles is faster than that of larger particles, so that the large particles act as collectors within some agglomeration volume. Any small particles present in the agglomeration volume are likely to aggregate to a larger particle, and this aggregation is desirable for applications such as cleaning particles from surfaces. A sweep of the acoustic driving parameters to

find the configuration for which maximal aggregations occurs could clearly be found and described in terms of the minimal squared fractional deviation of the particle kinetic energies, again due its measure of th effective number of degrees of freedom. In general, we hope our work may stimulate further research of STP systems with interacting particles and shed some light on their complicated and exciting dynamics.

Chapter 6

A Simple Model for Long-Range Interacting Pendula

6.1 Introduction

The challenges in understanding long-range systems drive the development of solvable models that could help better explain some of the aforementioned phenomena. Campa et al. (102) have recently published a collection of important solvable models. One particularly significant model, which is important to this paper, is the Hamiltonian Mean Field (HMF) XY spin model (42), often written in the form

$$H = \sum_{i=1}^{N} \frac{p_i^2}{2} + \frac{\gamma}{2N} \sum_{i,j=1}^{N} \left[1 - \cos\left(\theta_i - \theta_j\right)\right], \tag{6.1}$$

where θ_i is the angular position of the i^{th} particle (spin) and p_i is its conjugate angular momentum. The HMF model is generally used to describe two different classes of systems: 1) a mean field XY classical spin model, and 2) a one dimensional periodic

system of itinerant particles with long-range interactions. Though the connection between the HMF model and the second class of systems mentioned could be thought of as contrived given the simplifications under which the model is realized, it has been shown to produce useful insights into how non-neutral plasmas and self gravitating systems behave (42).

In this paper, we study the dynamics of an array of N pendulua with long-range interacting bobs. By considering long pendula with flat bobs undergoing small oscillations and having parallel planes of rotation, we produce a model related to the HMF model through a coordinate transformation. The transformation introduces a dependence on the indices of the particle labels. A cartoon of the physical picture is shown in Fig. 6.1. The index dependence in the Hamiltonian that we present will

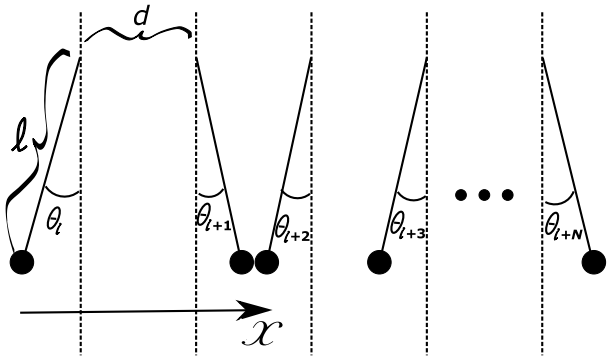

Figure 6.1: N pendulum system with parallel planes of rotation. The i^{th} pendulum angle at some time t is $\theta_i(t)$.

be described in detail in the next section but, as a prelude, it is a consequence of the pendulua pivots being slightly offset from one another and appears as a phase in the cosine term of the HMF model. It inspires the investigation of non-equilibrium "repulsive" behavior in the angle coordinate frame where we find an interesting quasistationary state when the angles of the pendula are initially ordered according to

their indices. We find the clustered positions in the usual HMF coordinate frame (biclusters), but in the angle coordinate frame clustering is only found for the initially ordered angles and, unlike the biclusters, these are clearly quasistationary states. A quasistationary state is defined as a dynamical state that can persist for a length of time which goes to infinity as the thermodynamic limit is approached (102). In addition to discussing the clustered angle states exhibited by the system, we also solve for the canonical partition function in the pendulum angle coordinate frame, finding that in equilibrium with a heat bath, the probability distributions of the angles can be described by the original HMF model. This finding is similar to the work done by (103) on a model sometimes called the HMF α-model. In the HMF α model, a $1/r_{ij}^{\alpha}$ dependence between the classical spins is introduced (102; 104; 105; 106), where r_{ij} is the distance between the i^{th} and j^{th} spins on a lattice. Though the physical motivations behind studying these various models can be very different, it is interesting that their equilibrium behavior is the same same or nearly the same. We believe that the work in this paper further suggests that the HMF model universally describes an entire class of long-range interacting systems in equilibrium.

6.2 The Model

6.2.1 Coordinates

In Fig. 6.1, we show an array of pendulua rotating in the same plane with bobs that interact through a long-range potential. If we consider the case where all the pendula only undergo small oscillations, we may write the horizontal location of the i^{th} particle,

x_i, as $x_i = id + \ell\theta_i$, where d is the distance between the pivots of neighboring pendula and ℓ is the length of each pendulum. The small θ regime makes the problem one dimensional in x. We choose periodic boundary conditions and rescale the system by $2\pi/Nd$ so that

$$x \to \frac{2\pi}{Nd}x \tag{6.2}$$

making the total system length a dimensionless 2π where N is the number of particles in one period. We will refer to a periodic space with length 2π as a unit circle. The position of the i^{th} particle (bob) is now

$$x_i = \frac{2\pi i}{N} + \frac{2\pi}{N}\frac{\ell}{d}\theta_i. \tag{6.3}$$

For reasonable choices of ℓ and d ($\ell/d << N$), the second term on the RHS is suitably small such that the Hamiltonian can be written with terms that are quadratic in θ. However, we are primarily interested in a regime where $\ell/d \to \infty$ as the thermodynamic limit is approached. Physically this corresponds to the small oscillations of very long pendula with suspension points that are close together compared to their lengths. In order to simplify the calculations that follow, we define ϕ_i to be the last term on the RHS of Eq. (6.3), namely $\phi_i \equiv 2\pi\ell\theta_i/Nd$. Given the choice of large ℓ/d, ϕ_i can take any value in the range $[0, 2\pi)$. This is only true because ℓ/d is large, *not* because the θ_is are. In terms of ϕ_i, the positions can be rewritten as

$$x_i = \frac{2\pi i}{N} + \phi_i. \tag{6.4}$$

6.2.2 Density Approximation

We have not yet explicitly stated the physical mechanism through which the bobs interact. Connecting the interactions with specific physical motivations is needed, but it should be discussed with some discretion because the development of the model leaves these motivations up to some interpretation. Imagine that the bobs all carry some charge. We will not distinguish between particles in any other way than their indices, so in the case where all carry the same charge, repulsive behavior is expected. On the other hand one could make the bobs attract one another, which could be thought of as the self-gravitating case. To be solvable, the model requires some simplifications. For the sake of brevity we will speak of the particle charge or mass density as the "density".

The approximation that we invoke is similar to that used when justifying the HMF model (Eq. (6.1)) to describe free particles in a one-dimensional ring (42; 45). The distribution of the bobs is such the mass density, $\rho(x)$, is given by

$$\rho(x) = \sum_{i=1}^{N} \delta(x - x_i) - \frac{1}{2\pi}. \tag{6.5}$$

The constant $1/2\pi$ subtracted from the delta function is necessary to produce a meaningful expression for the potential Φ and corresponds to including a neutralizing (of opposite sign) homogeneous background density. Restricting the problem further to that of solving Poisson's equation for a one-dimensional potential physically amounts to choosing large and flat bob geometries oriented with their smallest axis parallel to the x axis. Writing the delta function as a cosine Fourier series, Poisson's equation

becomes

$$\nabla^2\Phi(x) = \frac{\gamma}{\pi}\sum_{i=1}^{N}\sum_{n=1}^{\infty}\cos\left[n(x-x_i)\right]. \tag{6.6}$$

The parameter γ contains the particle (bob) charge or mass and becomes the interaction strength in the Hamiltonian. We can see that the zeroth-order term in the Fourier series canceled the constant neutralizing background that was superficially added.

The most important simplification in this paper is truncating the sum of the Fourier coefficients used to represent the delta function after the $n = 1$ coefficient. Antoni et al. defend the truncation by asserting that the "large scale collective properties" do not greatly change when higher order terms of the sum (including interactions at the smaller length scales) are included, and discuss the consequences of the approximation in some detail (42). The simplification also warrants a brief discussion of the way that it could be physically interpreted. The truncation of the sum is equivalent to smearing out the density of each particle over the system so that it is peaked at its given location, x_i, but also having a negative density peak on the opposite side of the unit circle. This could be thought of as doubling the number of particles and enforcing that each particle has a negative partner that always remains on the opposing side of the unit circle. After this doubling the masses are dispersed such that a pair's density is described by a cosine function with the positive peak centered at x_i.

6.2.3 Solving Poisson's Equation

Integrating Poisson's equation once, we obtain:

$$\nabla\Phi(x) = \frac{\gamma}{\pi}\sum_{i=1}^{N}\left\{\sin\left(x - x_i\right) + c_1\right\}. \tag{6.7}$$

In order to determine the constant c_1 from the integration, the physical picture should be examined. A sensible requirement is that when all of the bobs are hanging at their equilibrium positions, directly below their pivot (all $\phi_i = \theta_i = 0$), the net force experienced by any bob is zero. This is a valid requirement if the bobs are attractive or repulsive, the only difference being that the configuration would be unstable or stable, respectively. The force that the j^{th} particle experiences when ϕ_j and all ϕ_i are zero is given by

$$-\nabla\Phi\left(x_j\right) = -\frac{\gamma}{\pi}\sum_{i=1}^{N}\left\{\sin\left[\frac{2\pi(j-i)}{N}\right] + c_1\right\}. \tag{6.8}$$

The sum $\sum_i \sin\left[2\pi(j-i)/N\right]$ equals zero for any j, so c_1 must be zero. Integrating once more to obtain the potential yields

$$\Phi(x) = \frac{\gamma}{\pi}\sum_{i=1}^{N}\left[c_2 - \cos\left(x - \frac{2\pi i}{N} - \phi_i\right)\right]. \tag{6.9}$$

To determine c_2 we stipulate that if all $\phi_i = 0$, then $\Phi(0) = 0$. Inserting Eq. (6.3) (or Eq. (6.4)) for x_i yields

$$\Phi(0) = \frac{\gamma}{\pi}\sum_{i=1}^{N}\left[c_2 - \cos\left(\frac{2\pi i}{N}\right)\right]. \tag{6.10}$$

The sum over the cosine is zero, therefore $c_2 = 0$ and we can now write the potential energy of the j^{th} particle as

$$\Phi(x_j) = -\frac{\gamma}{\pi}\sum_{i=1}^{N}\cos\left[\frac{2\pi(j-i)}{N} + \phi_j - \phi_i\right]. \tag{6.11}$$

6.2.4 The Hamiltonian

The Hamiltonian can be written as

$$H = H_0 + H_I, \tag{6.12}$$

where H_0 is the kinetic energy piece

$$H_0 = \sum_{i=1}^{N}\frac{p_i^2}{2}, \tag{6.13}$$

and

$$H_I = -\frac{\gamma}{2N}\sum_{i,j=1}^{N}\cos\left[\frac{2\pi(i-j)}{N} + \phi_i - \phi_j\right] \tag{6.14}$$

is the interaction piece, so

$$H = \sum_{i=1}^{N}\frac{p_i^2}{2} - \frac{\gamma}{2N}\sum_{i,j=1}^{N}\cos\left[\frac{2\pi(i-j)}{N} + \phi_i - \phi_j\right]. \tag{6.15}$$

The mass of the bobs has been set to unity, γ is the interaction strength, a factor of $1/2$ accounts for the double counting, and the $1/\pi$ coefficient in the potential energy has been absorbed into γ. The factor of $1/N$ is a rescaling of the potential energy that ensures that as the thermodynamic limit is approached, the potential energy of

the system does not diverge. The $1/N$ scaling is known as the Kac prescription (44). The Kac serves to keep both the energy and entropy of a system proportional to the number of particles in the system, an important prerequisite for phase transitions (102).

6.2.5 Relationship to the HMF model and the Spin Interpretation

Due to the simple bijective relationship between x_i and ϕ_i one can simply solve the equations of motion for the HMF model and find the dynamics for ϕ_i via the coordinate transform $x_i \to \phi_i$. Previously it was mentioned that the HMF model is used to describe free particles on a ring with long-range repulsion or attraction, as well as describing a classical XY spin model. The θ_i played the role of either the position of the i^{th} particle on the ring or the orientation of the i^{th} spin. Therefore, it is interesting to speculate about the type of spin system the model describes in the ϕ_i picture. Thus far, the rescaled angle $\phi_i = 2\pi\ell\theta_i/Nd$ describes the distance of a pendulum bob from the point directly below its pivot, but it could also be interpreted as the orientation of spin. In the spin interpretation of Eq. (6.15), the potential energy of the i^{th} and j^{th} spin pair depend on both their relative orientation as well as the difference between their indices. In the following discussion it will sometimes be convenient to speak about ϕ_i in the spin language.

We will prove that in the ϕ picture, the system in equilibrium with a heat bath is equivalent to the HMF model (the x picture) in equilibrium with a heat bath by solving the partition function in the ϕ_i coordinate frame. In the process of simplifying

the Hamiltonian to solve for the partition function, we will find expressions of the form $\cos\phi_i$ and $\sin\phi_i$ which we talk about as the horizontal and vertical components of a magnetization $\vec{m}_i = (\cos\phi_i, \sin\phi_i)$. It could easily be stated that in the spin analogy, the ϕ_i are orientations of the spins, but we should make a more concrete connection between this idea and the original presentation of the model. We would like to remind the reader that even though the angles θ_i of the pendula are small, the long suspensions of the bobs (ℓ) allow ϕ_i to cover the entire system which, rescaled, has dimensionless length 2π. The system is also periodic, so the bobs can be thought of as moving on a unit circle where the position of the i^{th} bob is $x_i = 2\pi i/N + \phi_i$. In order to think of ϕ_i as the spin orientations, we start by considering each bob as living on its own individual unit circle. An example of these unit circles is shown in Fig. 6.2, a visual aid to the following. Imagine stacking horizontal circles in the vertical direction and rotating each by an angle $2\pi/N$ from the one below. The projection of these circles onto the horizontal plane would be the system viewed in x, i.e. the HMF model. If we twist the stack so there is no rotation between adjacent circles and then project onto the horizontal plane it creates the picture viewed in ϕ, where the pivot points are all aligned. The reason for this artificial construction of stacked circles is partly in order to pictorially depict the transformation between x and ϕ and partly to show how $\vec{m}_i$ (as defined) is just the orientation of the i^{th} spin in the ϕ picture. Said differently, each circle in the ϕ picture represents a spin with an orientation in the horizontal plane determined by ϕ_i; an infinite-range classical mean field spin model described by Eq. (6.15).

6.3 Equilibrium

In this section, we solve for the canonical partition function, in the ϕ coordinate frame using the Hamiltonian in Eq. (6.15) and show that, in equilibrium, the HMF model describes the angles of long pendula with long-range interacting bobs. In order to solve the configurational piece of the partition function the Hamiltonian must be modified. Using the cosine and sine sum and difference identities twice, the potential interaction piece of the Hamiltonian H_I can be written as

$$H_i = \frac{-\gamma}{2N}\sum_{i,j}\Bigg\{\cos\left[\frac{2\pi(i-j)}{N}\right][\cos\phi_i\cos\phi_j+\sin\phi_i\sin\phi_j] - \sin\left[\frac{2\pi(i-j)}{N}\right][\sin\phi_i\cos\phi_j-\cos\phi_i\sin\phi_j]\Bigg\}. \quad (6.16)$$

The coefficients in the Hamiltonian $\cos[2\pi(i-j)/N]$ and $\sin[2\pi(i-j)/N]$ should be thought of as matrices with components C_{ij} and S_{ij} respectively. The Hamiltonian can now be written in the form

$$\frac{\gamma}{2N}\sum_{i,j}(\cos\phi_i C_{ij}\cos\phi_j+\sin\phi_i C_{ij}\sin\phi_j - \sin\phi_i S_{ij}\cos\phi_j+\cos\phi_i S_{ij}\sin\phi_j), \quad (6.17)$$

which is suggestive because it can be regarded as the matrix equation

$$H_I = \frac{\gamma}{2N}\Bigg[(\cos\phi_1, \cos\phi_2, ..., \cos\phi_N)C \begin{pmatrix} \cos\phi_1 \\ \cos\phi_2 \\ \vdots \\ \cos\phi_N \end{pmatrix} + (\sin\phi_1, \sin\phi_2, ..., \sin\phi_N)C \begin{pmatrix} \sin\phi_1 \\ \sin\phi_2 \\ \vdots \\ \sin\phi_N \end{pmatrix} - (\sin\phi_1, \sin\phi_2, ..., \sin\phi_N)S \begin{pmatrix} \cos\phi_1 \\ \cos\phi_2 \\ \vdots \\ \cos\phi_N \end{pmatrix} + (\cos\phi_1, \cos\phi_2, ..., \cos\phi_N)S \begin{pmatrix} \sin\phi_1 \\ \sin\phi_2 \\ \vdots \\ \sin\phi_N \end{pmatrix}\Bigg]. \quad (6.18)$$

It is helpful to consider the particles positions on the unit circle with respect to their pivot (ϕ) as magnetizations. Defining

$$\vec{m}_i \equiv (\cos\phi_i, \sin\phi_i), \quad (6.19)$$

and with $m_\mu^T = (m_{0,\mu}, m_{1,\mu}, ..., m_{N-1,\mu})$ where μ holds the place of x or y, the Hamil-

tonian becomes

$$H_I = \frac{\gamma}{2N}(m_x^T C m_x + m_y^T C m_y - m_y^T S m_x + m_x^T S m_y). \tag{6.20}$$

A closer examination of the structure of the coefficient matrices C and S indicates that they take the special form of circulant matrices, and thus can be simultaneously diagonalized by a unitary matrix U. A circulant matrix has the form

$$\begin{pmatrix} a_1 & a_2 & a_3 & \dots & a_{N-1} & a_N \\ a_N & a_1 & a_2 & \dots & a_{N-2} & a_{N-1} \\ a_{N-1} & a_N & a_1 & \dots & a_{N-3} & a_{N-2} \\ \vdots & \vdots & \vdots & \ddots & \vdots & \vdots \\ a_3 & a_4 & a_5 & \dots & a_1 & a_2 \\ a_2 & a_3 & a_4 & \dots & a_N & a_1 \end{pmatrix}, \tag{6.21}$$

a special kind of Toeplitz matrix, where each subsequent row is a cyclic permutation of the row above or below it. Any matrix A with elements a_{ij} that can be written in terms of some function $f(i-j)$ is a circulant matrix. Because a circulant matrix is a normal matrix it can be diagonalized by a unitary matrix. We show that C and S are simultaneously diagonalizable by showing that they commute, i.e. $[C, S] = 0$ where $[C, S] = CS - SC$. Starting with the second term, $-SC = S^T C^T = (CS)^T$ which is found by arguing that C is symmetric since cosine is an even function and does not change under the exchange of i and j, whereas S is odd because sine is an odd function and does change sign under exchange of i and j. The commutation becomes $[C, S] = CS + (CS)^T$. Also, an odd function multiplied by an even function results in

an odd function so the entire matrix CS is odd. Therefore $(CS)^T = -CS$ bringing us to the final expression $[C, S] = CS - CS = 0$. We have shown that C and S can be simultaneously diagonalized by U. The matrix U is known for circulant matrices and is called the Fourier Matrix.

The matrices C and S can be rewritten as $C = U^\dagger D^C U$ and $S = U^\dagger D^S U$, where D^C and D^S are diagonal matrices with diagonal elements that are the eigenvalues of C and S, respectively, which we denote as λ_i^C and λ_i^S. From here on we label the indices i from 0 to $N-1$. It is worth pointing out that due to S being antisymmetric, U must be complex. Equation (6.22) becomes

$$H_I = \frac{\gamma}{2N}\Big(m_x^T U^\dagger D^C U m_x + m_y^T U^\dagger D^C U m_y - m_y^T U^\dagger D^S U m_x + m_x^T U^\dagger D^S U m_y\Big). \quad (6.22)$$

We will move back to the index notation using the following relations:

$$D^{C,S} = \lambda_i^{C,S}\delta_{ij}, \quad (6.23)$$

$$X_j \equiv \sum_{k=1}^{N} U_{jk} m_k^x, \quad (6.24)$$

and

$$Y_j \equiv \sum_{k=1}^{N} U_{jk} m_k^y., \quad (6.25)$$

where X is not to be confused with x. Using the Kronecker delta, we set all $i = j$ since these are the only nonzero terms. The Hamiltonian is now given by

$$H_i = \frac{-\gamma}{2N}\sum_{j=0}^{N-1}\Big(\|X_j\|^2\lambda_j^C + \|Y_j\|^2\lambda_j^C - Y_j^* X_j \lambda_j^S + X_j^* Y_j \lambda_j^S\Big), \quad (6.26)$$

with $\|X\| = XX^*$ and $\|Y\| = YY^*$. The inclusion of the eigenvalues λ^C and λ^S simplifies the Hamiltonian further. We will now solve for λ^C and λ^S. Looking at the form of a circulant matrix shown in Eq. (6.21) reminds us that the elements of a circulant matrix can be defined with a single label. We write the single labeled elements of the cosine and sine matrices respectively as

$$c_l = \cos\frac{2\pi l}{N}, \tag{6.27}$$

and

$$s_l = \sin\frac{2\pi l}{N}, \tag{6.28}$$

where $l = 0, 1, 2, ..., N-1$. The eigenvalues, λ^A, of a $N \times N$ circulant matrix A can be written in terms of the single label elements a_l. The j^{th} eigenvalue of A is known to be $\lambda_j^A = \sum_{l=0}^{N-1} a_l \exp(2\pi i l j/N)$, where i is $\sqrt{-1}$ (not an index) and $l = 0, 1, 2, ..., N-1$. Therefore,

$$\lambda_j^C = \sum_{l=0}^{N-1} \cos\left(\frac{2\pi l}{N}\right) e^{2\pi i l j/N}, \tag{6.29}$$

and

$$\lambda_j^S = \sum_{l=0}^{N-1} \sin\left(\frac{2\pi l}{N}\right) e^{2\pi i l j/N}. \tag{6.30}$$

Writing cosine and sine in their exponential forms gives

$$\lambda_j^C = \frac{1}{2}\sum_{l=0}^{N-1}\left[e^{i2\pi l(j+1)/N} + e^{i2\pi l(j-1)/N}\right], \tag{6.31}$$

$$\lambda_j^S = \frac{-i}{2}\sum_{l=0}^{N-1}\left[e^{i2\pi l(j+1)/N} + e^{i2\pi l(j-1)/N}\right], \tag{6.32}$$

The above representations of the eigenvalues show that C and S each have only two

non-zero eigenvalues corresponding to $j = 1, N-1$ given by $\lambda_1^C = \lambda_{N-1}^C = N/2$ and $\lambda_1^S = (\lambda_{N-1}^S)^* = iN/2$. The Hamiltonian simplifies greatly to

$$H_I = \frac{\gamma}{2} - \left(\|X_1 + iY_1\|^2 + \|X_{N-1} - iY_{N-1}\|^2 \right). \tag{6.33}$$

The representation of H_I in Eq. (6.33) must be further modified before the partition function can be found. We do this by splitting the Fourier matrix U into its real and imaginary components, a_{ik} and b_{ik}, given by

$$a_{ik} \equiv \frac{1}{\sqrt{N}} \cos\left(\frac{2\pi ik}{N}\right), \tag{6.34}$$

and

$$b_{ik} \equiv \frac{1}{\sqrt{N}} \sin\left(\frac{2\pi ik}{N}\right). \tag{6.35}$$

This was done to write the absolute squares in Eq. (6.33) in terms of the squares of a_{ik} and b_{ik}. By noticing that $a_{1k} = a_{(N-1)k}$ and $b_{1k} = -b_{(N-1)k}$ we write the configurational partition function as

$$Z_I = A \int d^N \phi e^{\frac{\beta\gamma}{2}\left(\sum_k \left[a_{1k} m_k^x - b_{1k} m_k^y\right]\right)^2} e^{\frac{\beta\gamma}{2}\left(\sum_k \left[b_{1k} m_k^x + a_{1k} m_k^y\right]\right)^2}, \tag{6.36}$$

where $\beta = 1/k_B T$.

The Hubbard-Stratonovich transformation is now applied twice, once to each quadratic quantity in the partition function. The integration variables introduced through this transformation are z_1 and z_2 with subscripts for first and second quadratic

quantities, respectively. After after switching the order of integration, we find

$$Z_I = \frac{A}{2\pi\beta\gamma}\int_{-\infty}^{\infty} dz_1 dz_2 e^{-(z_1^2+z_2^2)/2\beta\gamma}\prod_k \times \int_{-\pi}^{\pi} d\phi_k e^{(z_1 a_{1k}+z_2 b_{1k})\cos\phi_k+(z_2 a_{1k}-z_1 b_{1k})\sin\phi_k}. \quad (6.37)$$

The integration can be performed using the identity

$$\int_{-\pi}^{\pi} d\phi e^{\xi\cos\phi+\eta\sin\phi} = 2\pi I_0\left(\sqrt{\xi^2+\eta^2}\right) \quad (6.38)$$

where

$$\xi^2+\eta^2 = (z_1 a_{1k}+z_2 b_{1k})^2 + (z_2 a_{1k}-z_1 b_{1k})^2 \quad (6.39)$$

which simplifies when a and b are included to

$$\left[z_1\frac{1}{\sqrt{N}}\cos\left(\frac{2\pi k}{N}\right)+z_2\frac{1}{\sqrt{N}}\sin\left(\frac{2\pi k}{N}\right)\right]^2 + \left[z_2\frac{1}{\sqrt{N}}\cos\left(\frac{2\pi k}{N}\right)-z_1\frac{1}{\sqrt{N}}\sin\left(\frac{2\pi k}{N}\right)\right]^2 = \frac{1}{N}(z_1^2+z_2^2) \quad (6.40)$$

It is convenient to make a change to polar coordinates by introducing $z=\sqrt{z_1^2+z_2^2}$, following which the partition function can be written as

$$Z_I = \frac{A}{\beta\gamma}\int_{-\infty}^{\infty} dz e^{-z/2\beta\gamma}\prod_k 2\pi I_0\left(\frac{\sqrt{z}}{\sqrt{N}}\right). \quad (6.41)$$

Equation (6.41) is recognized to be an intermediate step of the solution to the canonical partition function for the HMF model. From here we jump to the main results, the details of which are included in the HMF literature (42; 45; 102) .

The integration over z in Eq. (6.41) can be preformed using the saddle point approximation. The rescaled free energy per particle follows as

$$-\beta F = -\frac{\beta}{2} + \inf_{z}\left[\frac{-z^2}{2\beta} + \ln 2\pi I_0(z)\right] \tag{6.42}$$

The expression above permits a convenient path to finding the phase transition. Solving for the minimum values of z in order to satisfy the last term in Eq. (6.42) results in the equation

$$\frac{z}{\beta} - \frac{I_1(z)}{I_0(z)} = 0, \tag{6.43}$$

which can be solved self consistently for z and represented graphically for different values of β as in Fig. 6.3. The reader will see that after β is increased passed the critical value ($\beta = 2$) there are two well-defined solutions.

The Hubbard-Stratonovich transformation decouples spin-spin (squared terms in the Hamiltonian) contributions to the partition function at the price of needing to create a linear interaction between each spin with an auxiliary field z (107). Again, a more detailed procedure can be found in (42; 45; 102) where discussion of the internal energy in the equilibrium state is followed by non-equilibrium behavior of the system prepared in microcanonical ensembles. Here we will simply touch on the most important point of the equilibrium behavior, being that for $\beta < 2$ the system is paramagnetic but for $\beta \geq 2$ a pitchfork bifurcation occurs resulting in two stable solutions. At this point there is a discontinuity in the free energy, a second order phase transition occurs and the system can maintain finite magnetization. In this case, the order parameter is the total magnetization $\vec{M} = \frac{1}{N}\sum_{j=1}^{N}\vec{m}_i$ where $\vec{m}_i$ was defined to be $(\cos\phi_i, \sin\phi_i)$.

Showing that the canonical partition function in the ϕ coordinate frame model and the HMF model are equivalent necessitates a more detailed discussion of the equilibrum behaviors in the ϕ frame. Campa et al. (102), in their review of the HMF model, rigorously show ensemble equivalence between the canonical and microcanoical ensemble of the HMF model. In light of this fact, a large N microcanonical simulation should be able to produce equilibrium behavior like the phase transition mentioned above. The temperature in a numerical simulation of a system with many particles would be "set" through a choice of the initial momenta distribution. In this type of simulation, it is common practice to compute the order parameter and free energy (38; 108; 42), begging the question: does a large microcaonical simulation of Eq. (6.15) approximate the expected equilibrium behavior? Also, since the index-dependent model in equilibrium with a heat bath can be described by the HMF model, would the dynamics of such a simulation qualitatively resemble those in the HMF model? The answer to both of these questions is *no* if one were to find the equations of motions in ϕ_i for some large N and then compare them to an HMF model or the x coordinate frame. As stated, this discrepancy may appear to detract from our result. Indeed, it uncovers a conceptual omission in the model, but it is one whose rectification gives insight into the models ensemble equivalence property of the model, or lack thereof. The omission was in the arbitrary scaling of x which we will now rectify.

We introduce the parameter L which generalizes the scaling in Eq. (6.2) to

$$x \to \frac{2\pi L}{Nd} x, \tag{6.44}$$

making the position of the i^{th} particle

$$x_i = \frac{2\pi L i}{N} + \frac{2\pi L}{N}\frac{\ell}{d}\theta_i. \tag{6.45}$$

and changing the definition of ϕ_i to $\phi_i \equiv 2\pi L\ell\theta_i/Nd$. It can be shown that the introduction of L only changes the final result of the partition function by a constant factor of L due to the enlarged limits of integration. Numerically, we find is that if $L >> 1$, then the simulations in ϕ closely reproduce the dynamics of HMF model simulations (dynamics in x). Therefore, for large L the mirocanonical simulations can approximate equilibrium and the answers to the previous questions - does a large microcaonical simulation of Eq. (6.15) approximate the expected equilibrium behavior, and since the index-dependent model in equilibrium with a heat bath can be described by the HMF model, would the dynamics of such a simulation qualitatively resemble those in the HMF model? - becomes *yes*. Alternatively, the coordinate frame inequivelence is most extreme for small L. These numerical results were found using initial conditions that are randomly distributed ϕ_i about the domain $[-L\pi, L\pi)$. It should be stated that for the rest of this paper we work with $L = 1$ becuase we are inetersed in cases where the ϕ coordinate frame is markedly differnet than the x coordinate frame.

6.4 Non-Equilibrium Results

For a system of pendula, it is interesting to study an initial configuration where all pendula are set to random small displacements from $\phi_i = 0$. Specifically we initialize the i^{th} pendulum angle, ϕ_i, randomly in the range $[-\pi/N, \pi/N)$. In x the indices

are ordered in x such that $x_1 < x_2 < x_3 < ... < x_N$ and the i^{th} bob is randomly distributed in the range $[2\pi i/N - \pi/N, 2\pi i/N + \pi/N)$. It is possible to make some general statements about the dynamics of this configuration in x using the equations of motion. Expressing the Hamiltonian with terms that are quadratic in ϕ yields

$$H_I = \frac{\gamma}{2N}\sum_{ij}\left\{\sin\left[\frac{2\pi(i-j)}{N}\right](\phi_i - \phi_j) \right. \\ \left. - \cos\left[\frac{2\pi(i-j)}{N}\right]\left(1 - \frac{\phi_j^2}{2} - \frac{\phi_i^2}{2} + \phi_i\phi_j\right)\right\}. \quad (6.46)$$

With this expression, the equations of motion for the i^{th} particle can be written as

$$\ddot{\phi}_i = \dot{p}_i = \frac{\partial H}{\partial \phi_i}, \quad (6.47)$$

from which we obtain

$$\ddot{\phi}_i = \frac{-\gamma}{2N}\sum_j\left\{\cos\left[\frac{2\pi(i-j)}{N}\right](\phi_j - \phi_i) + \sin\left[\frac{2\pi(i-j)}{N}\right]\right\}. \quad (6.48)$$

In the above equation, the last term and the $\cos[2\pi(i-j)/N]\phi_i$ term sum to zero, leading to

$$\ddot{\phi}_i = \frac{-\gamma}{2N}\sum_j \cos\left[\frac{2\pi(i-j)}{N}\right]\phi_j. \quad (6.49)$$

Using the difference formula, we write the acceleration as

$$\ddot{\phi}_i = \frac{-\gamma}{2}\left[\cos\left(\frac{2\pi i}{N}\right)\langle\mu_1\rangle + \sin\left(\frac{2\pi i}{N}\right)\langle\mu_2\rangle\right], \quad (6.50)$$

where $\mu_1 = \phi_j \cos(2\pi i/N)$ and $\mu_2 = \phi_j \sin(2\pi i/N)$. The mass (moment of inertia) has been set to unity so the above expression is the force as a function of index, $\ddot{\phi}_i = F(i)$. If $\langle\mu_1\rangle$ and $\langle\mu_2\rangle$ are known, then the initial dynamics of the system are elucidated by Eq. (6.50), but in the case of randomly initialized ϕ_i the $\langle\mu_1\rangle$ and $\langle\mu_2\rangle$ are also random and can be different from one another in both magnitude and sign. However, a general description of the results can be given without exactly knowing these coefficients. Equation (6.50) shows that the initial force on a given particle depends on its position because the indices are ordered in x. In the continuum (thermodynamic limit), the force takes the form

$$F(x) \equiv \frac{-\gamma}{2} \left(\langle\mu_1\rangle \cos x + \langle\mu_2\rangle \sin x \right). \tag{6.51}$$

Therefore $\langle\mu_1\rangle$ and $\langle\mu_2\rangle$ partly play the role of the amplitude of this force as a function of x, but also can shift the $\cos x + \sin x$ spatial dependence, which is periodic over the system length. In Fig. 6.4, we show a fit of the force as a function of x using Eq. (6.51) as well as the actual force calculated for an example set of initial conditions. The domain in Fig. 6.4 can be split into two pieces (independent of μ)- one where the particles experience a positive force, the other in which the particles experience a negative force. As time is increased, the movements of the particles evolve the coefficients $\langle\mu_1\rangle$ and $\langle\mu_2\rangle$ in such a way that the magnitude of the force decreases to zero for all particles and then switches sign complementary to the original force. This results in a standing compression wave of the particles with a wavelength 2π. The compression wave is not stable and eventually two clusters form about each node. These two clusters are often referred to as a "bicluster", or the antiferromagnetic state in the HMF model, and have been explained by Barré et al. by analysing

the Vlasov equation. They find that the initial compression wave (referred to by a different name) creates an effective double-well potential giving rise to the bicluster (48). The question of the bicluster stability has not yet been definitely answered, but for a detailed discussion we refer the reader to Leyvraz et al. (109). Given the simple mapping between the ϕ and x coordinate frames, we should also be able to show the initial form of the force in x as well. As presented in Eq. (6.15), the Hamiltonian in the x coordinate frame only differs from the HMF model by a constant $\gamma/2$. In x, H_I is

$$H_I = \frac{\gamma}{2N} \sum_{i,j=1}^{N} \cos\left(x_i - x_j\right). \tag{6.52}$$

Using the difference identity, we find the equations of motion for the i^{th} particle to be

$$\ddot{x}_i \frac{-\gamma}{2N} \left(-\sin x_i \sum_j \cos x_j + \cos x_i \sum_j \sin x_j \right). \tag{6.53}$$

The sums over cosine and sine of x_j play the same role as $\langle \mu_1 \rangle$ and $\langle \mu_2 \rangle$, and the force at a given position x_i is clearly of the same form as that shown in Eq. (6.50).

Depending on $\langle \mu_1 \rangle$ and $\langle \mu_2 \rangle$, all ϕ_i oscillate about zero with amplitudes and phases that depend on their location x_i as discussed above. As the clustering in x begins, the ϕ_i begin to spread out over the full domain $[0, 2\pi)$ and continue to do so until it is covered. The more interesting case in ϕ is when all ϕ_i are initially randomly distributed in ranges that depend on their index, specifically when ϕ_i are chosen in the ranges. $[2\pi i/N - \pi/N, 2\pi i/N + \pi/N)$ so that $\phi_1 < \phi_2 < \phi_3 < ... < \phi_N$. It should be noted that in this new configuration the dynamics in x are nearly identical to the configuration previously discussed for ordered x_i. The dynamics in ϕ differ *drastically* between the two cases though. In this ordered angle case, we find some interesting

grouping of the scaled angles.

Initially the bobs oscillate with an amplitude that depends sinusoidally on their position in ϕ, similar to the previous discussion in the x picture but with four nodes where the ϕ_i remain relatively stationary. Once again this behavior could be thought of as a standing compression wave, but in ϕ_i it has a wave length of π whereas in the x picture it had a wavelength of 2π. As the system evolves, all ϕ_i slowly begin to shift towards the nodes of this standing wave until there are four clusters of the angles. After some time, the angles begin to re-distribute themselves randomly about the domain. The distribution of ϕ_i in these three regimes is summarized in three histograms shown in Fig. 6.5. Aside from the number of clusters, there are two primary differences between the clustering in ϕ and the clustering in x: (i) The clustering in ϕ *only* occurs when the angles are ordered in the method described above, whereas the dynamics in x look identical regardless of the distribution in x, presuming it is somewhat homogeneous about the domain. (ii) The clustering in ϕ is a quasistationary state whereas the clustering in x exists for much longer times regardless of the system size. Since the clustering in ϕ is quasistationary, a properly prepared system could exist in the clustered angle state for an arbitrarily long time but only for large N. We can view the effect of increasing N and therefore the lifetimes of the clustered states by observing the order of the particle index as a function of time. In Fig. 6.6(a)-(c), we show that as N is increased, the time it takes for particles to fully mix increases. This is shown by plotting the indices on a color scale from 0 (blue) to $N-1$ (red) along the horizontal axis as time is increased along the vertical axis. In Fig. 6.6(d), we show how the ordering of the particles changes at the very beginning of clustering for $N = 100$. Figure. 6.6 also shows that the compression

wave is not quasistationary since it quickly reduces to the clustered state regardless of N.

6.5 Conclusion

Though the application of statistical mechanics and thermodynamics to systems with long-range interactions may not always be appropriate, we find that the canonical partition function improves our understanding of a system of pendula with long-range interacting bobs. Solving for the canonical partition function of the Hamiltonian in Eq. (6.15), we show that the equilibrium behavior in the ϕ coordinate frame is equivalent to the x coordinate frame, i.e. the HMF model. As we have argued that the Hamiltonian in Eq. (6.15) describes the behavior of the angles of repulsive or attracting pendulum bobs (see Fig. 6.1), then the proven equivalence of the canonical partition function of Eq. (6.15) and the Hamiltonian mean field model suggests that the Hamiltonian mean field model sufficiently describes the angles of a system of pendula in equilibrium. Ensemble equivalence between the microcanonical ensemble and the canonical ensemble is known for the Hamiltonian mean field model model (102) and because of this, the microcanonical simulations could be used to approximate equilibrium behavior. We find numerically that in the case of large system lengths, L, the dynamics of the system in ϕ resemble the dynamics of the Hamiltonian mean field model, equivalently the behavior of the system in x. Therefore for large system sizes of long pendula in equilibrium, the HMF model describes their dynamics and statistics.

In this paper we also briefly discuss two particular sets of non-equilibrium results.

In one case, the system is initialized with small ϕ_i so that x_i are distributed relatively evenly throughout the x domain. This initial configuration essentially gives rise to the "repulsive" low temperature HMF model which exhibits interesting non-equilibrium behavior and is described in great detail by (110; 48). In the second case in which ϕ_i are ordered by index in ϕ. We show that in the ordered ϕ_i case there is a compression wave in ϕ, followed by clustering, and finally a mixed index state displaying no apparent order or structure. This is in contrast to the dynamics produced by a randomly distributed set of initial ϕ_i which begins and then remains in a random disordered state. The clustering that can occur in ϕ is different than the clustering in x because it only occurs when the angles are initially ordered and because it is quasistationary; the lifetime increases with the number of particles in the system.

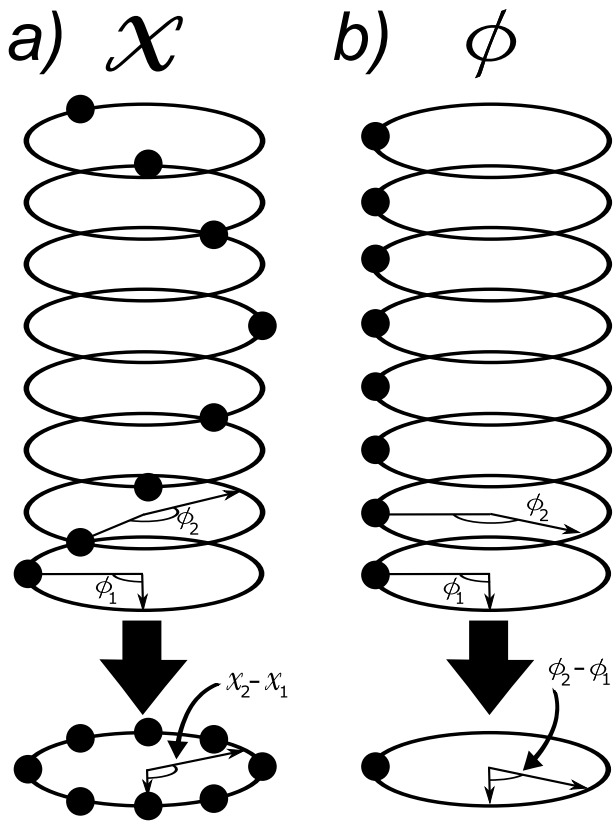

Figure 6.2: Example of a system of $N = 8$ particles when viewed as individual spins in the a) x coordinate frame, and b) the ϕ coordinate frame. a) In the x coordinate frame the direction of the i^{th} spin given by the angle x_i is expressed as $x_i = 2\pi i/N + \phi_i$. Alternatively, x_i could be thought of as the position of i^{th} particle on the unit circle, shown at the bottom of the figure as the projection of all positions onto the horizontal plane. The black circles on the rings in the figure mark the location of the pendulum pivots at $2\pi i/N$ in x. b) Twisting the column of rings in a) such that the pivots are aligned transforms the system into the ϕ_i coordinate frame. In this picture, the direction of the i^{th} spin is just given by the angle ϕ_i.

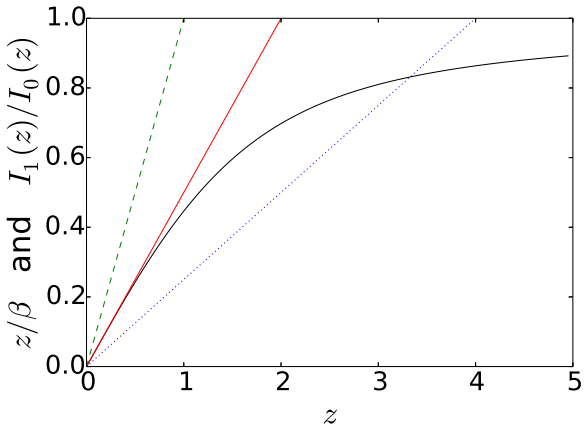

Figure 6.3: The solid (black) curve is the fraction of modified Bessel functions $I_1(z)/I_0(z)$, dashed (green) is z/β for $\beta = 1$, solid (red) line is z/β for beta $= 2$, dotted (blue) is z/β for $\beta = 4$, all as a function of z. (blue) line is z/β for $\beta = 4$. The values $\beta = 1, 2, 4$ correspond to the pre-phase transition, critical, and post-phase transition values in that order.

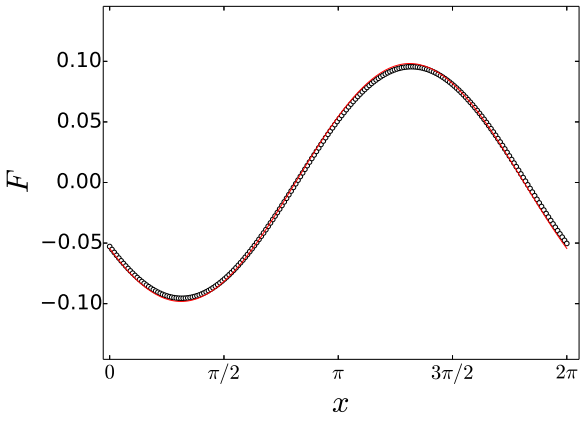

Figure 6.4: Numerical (blue) and theoretical (red) value of the $t = 0$ force felt by each particle as a function of its position. This configuration was made with $N = 200$ and $\gamma = 10$. The initial ϕ_i used for the numerical calculation were chosen randomly in the range $[0, 2\pi/N)$ which was restricted to positive values so that the sign of the initial $\langle\mu_1\rangle$ and $\langle\mu_2\rangle$ were known to be positive. This is not significantly different than when the range of ϕ_i is centred about 0. The theoretical curve is fitted using Eq. (6.51) with $\langle\mu_1\rangle = 0.0109$ and $\langle\mu_2\rangle = 0.0163$.

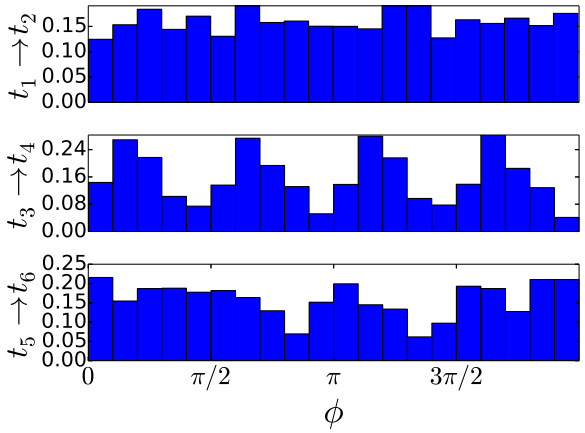

Figure 6.5: These three histograms are made by binning ϕ_i of 50 particles over three different periods of time with $\gamma = 10$. Going from top to bottom each period of time belongs to the dynamical regime of: standing "compression wave" in ϕ_i from initial configuration of $\phi_i \in [i - 2\pi/N, i + 2\pi/N)$, clustered motion about the four initial nodes of the compression wave, ϕ_i disordered final state. Specifically the values of t are: $t_1 = 0$, $t_2 = 50$, $t_3 = 100$, $t_4 = 200$, $t_5 = 7,000$, $t_6 = 7,200$.

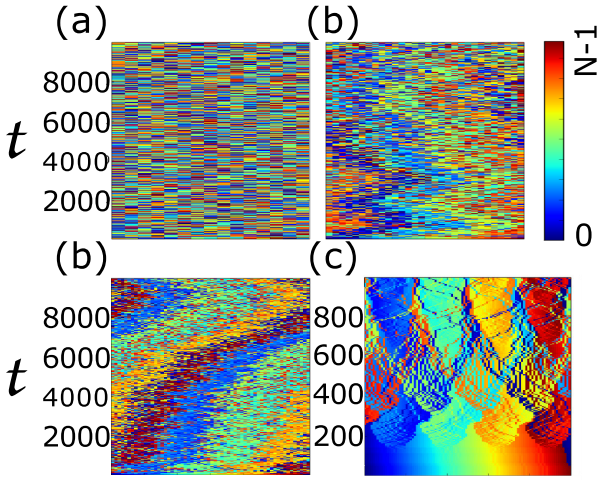

Figure 6.6: Each particle is colored from blue, representing the smallest index, to red, representing the largest index. The order of the particles indices at a given moment in time is plotted along the horizontal axis. Time increases along the vertical axis.(a) $N = 15$. (b) $N = 30$. (c) $N = 60$. (d) $N = 100$, where a smaller range of time is shown in order to see the mixing of the indices as the angles begin to cluster.

Chapter 7

Conclusions and Future Work

7.1 Conclusions

Since we have concluded each separate chapter that contains results individually, here we will not make any remarks regarding the specific of bodies of work. Instead, let us make some general comments on the importance of the systems that we have studied and what should be done to study them further. After reading the preceding chapters the reader may be left feeling that more must be done to bridge the gap between the fields of statistical mechanics and dynamical systems, and the study of statistical mechanics as applied to long-range interactions. After all, statistical mechanics has proven to be one of the most successful theories in describing the macroscopic properties of systems with many interacting bodies. In the case of deterministic (not Brownian) driven dissipative and long-range interacting systems, statistical mechanics can fail due to issues with ergodicity. The future work we are most concerned with therefore involves finding a deeper connection between ergodicity and these troublesome systems, hoping that it might lead to a generalized theory

of statistical mechanics which can handle them.

Let us elaborate on the current understanding of ergodicity and where the problems arise in treating driven dissipative and long-range interacting systems. Ergodicity can be clearly defined. Detailed mathematical definitions may be found in various places including books devoted to this singular topic (111; 112). However, if you ask the simple question of whether or not a given system is ergodic, the answer is determined (or can be in some cases) in a rather crude way. If the time average of a physical quantity of the system is equivalent to the full phase space average (different trajectories in phase space) of the same quantity than your system can be said to be ergodic. Otherwise it is not. If it is not ergodic, then there are additional conserved quantities that allow you to divide up the phase space.

The method of comparing the time average to the phase average allows one to determine ergodicity, but does it offer any promising generalizations? Phrased slightly differently, does the way in which ergodicity is determined give insight into how one might generalize the tools of statistical mechanics to include some systems that are not ergodic in the usual definition? We think it should be possible to make such a generalization for a driven dissipative system with long-range interactions, at least for the particular case of the chaotic regime after transients have died out.

Some driven dissipative systems are not so different from those which are treated in standard statistical mechanics text books, except for the fact that the random (chaotic) motion is restricted to a particular volume of the phase space. This restricted volume is likely defined by a stranger attractor. A class of dynamical systems known to satisfy Smale's axiom A can be approximated with a specific type of stretching and folding map known as an Anosov map. What does this mean to us? These systems are

important because Ruelle and Brown (113) have proven an ergodic theorem for strange attractors which satisfy Smale's axiom A. Therefore, if one can construct a driven dissipative system containing a finite number of long-range interacting particles that satisfies the correct stretching and folding of the phase space. In the thermodynamic limit, things are more challenging. However, if we are focused on periodic systems we might be able to dress the interactions of the particles, as we have done in chapter 5 where the coulomb force went to a polygamma function, to treat an infinite system with a finite number of particles per spatial period.

The discussion of ergodicity for strange attractors that can be approximated by an Anosov map is extremely mathematical and may not be applicable to many systems. It is somewhat unfortunate that the properties of strange attractors, such as the amount of the phase space it occupies and its Lyapunov spectrum, are often determined numerically, even when an approximate analytical treatment exists. The reason numerics are often the preferred approach in a preliminary study is in part because they are easier, but it is also partly because it takes time and is not always possible to determine a systems mathematical class. Since we are not sure if the proposal in the last paragraph is even possible, we will speculate a little further. Gilmore and Lefranc (35) have condensed the classification of chaotic systems into topological groups making an infinite number of dynamical systems classifiable by discrete quantities relating to the topology of stretching and folding mechanisms. Indeed topology is an important concept in Axiom A but Gilmore and Lefranc's book presents a slightly different prospective. Their classifications are relatively intuitive and can even determine a topological class from experimental data. Given their elegant classifications of chaos, and therefore the phase space "randomness", it seems

feasible that understanding a strange attractor's topological class might be used to find an ergodic theory for it.

One last point must be addressed. In most cases, a large number of degrees of freedom makes a system thermalize in a normal way. Driven dissipative or not, with many particles there might be a natural approach to an ergodic state through collisions. No extra theorizing would be needed. The value in exploring a generalized theory comes from interactions which are long-range and therefore don't thermalize normally, sometimes even spontaneously creating coherent structures (114). Though Gilmore and Lefrank's work is primarily on low dimensional systems they also comment on the possibility of discrete classifications in higher dimensions if the system exhibits specific stretching and folding properties. Even though they often break the standard definitions of ergodicity, a long-range interacting system could settle into chaotic motion that is described by a high dimensional strange attractor. In this case, these ideas could lead to the appropriate generalizations of statistical mechanics. Even if such work could only be done on the simplest "toy" models, it could produce valuable insight into the physics of these pathological systems.

Appendix A

Appendicies

A.1 Solving for the Electric Potential of a 2-Phase Electric Curtain

We can greatly simplify the problem of solving for the potential of an infinite series of parallel electrodes of infinite long length by rotating our coordinate system onto the complex plane and then making an appropriate conformal transformation. Here we use a similar procedure to that used by Masuda and Kamimura (70) to solve for the electric potential and field of the 2-phase EC.

We start by defining the plane of the electrodes to be the x, z plane. The electrodes are infinitely long running parallel to the z-axis and are spaced evenly along the x-axis. The y-axis is perpendicular to the plane of the electrodes. We define the wavelength to be the space between adjacent electrodes 1 and 3 as shown in fig. A1.1 (a) and label them from 1-3 respectively. The electric potential applied to the adjacent electrodes are 180 degrees out of phase so we express the charge per unit length on each electrode

as

$$Q_n = Q\cos\omega t - (n-1)\pi \tag{A.1}$$

where n denotes the electrode of interest; i.e. $n = 1, 2, 3, ...\infty$. We choose to solve for the potential in the complex plane u, iv. The mapping is accomplished through the conformal transformation:

$$e^{(y+ix)2\pi/\lambda} = u + iv \tag{A.2}$$

introduced by Masuda and Kamimura (70). In fig. A1.2 we see that we can map an infinite set of electrodes onto a unit circle containing only 2 points because electrodes 1, 3, 5... map to the same location. It is also true that the electrodes 4, 6, 8... would map to electrode 2 on u and indeed all electrodes on x map to the two points on the u-axis. We can now solve for the electric potential in the u, v plane and map our result back onto the x, y plane. Since the electrodes are infinitely long, we may express a two dimensional electric potential produced by the two neighboring electrodes as,

$$\Phi(u, v) = \sum_{n=1}^{2} \frac{-Q_n}{2\pi\epsilon_0} \ln r_n, \tag{A.3}$$

where n denotes the n^{th} electrode, Q_n is given by Eq. (A.1) and r_n is the distance between the point of interest (u, v) of the field coordinates and the source coordinates (u', v') of the n^{th} electrode:

$$r_n = \sqrt{(u - u'_n)^2 + (v - v'_n)^2} \tag{A.4}$$

Using Eq. (A.4) we can express u and v in terms of x and y and find the corresponding electric potential in the x, y plane: $u = \mathrm{Re}[e^{k(y+ix)}]$, $v = \mathrm{Im}[e^{k(y+ix)}]$. We find that $r_n = \sqrt{2e^{ky}(\cosh ky - \cos k(x - x'_n))}$. The potential can now be expressed in terms of only x, and y as

$$\Phi(x,y) = \sum_{n=1}^{2} \frac{-Q}{4\pi\epsilon_0} \cos(\omega t - (n-1)\pi)) \{\ln 2 + ky + \ln(\cosh ky - \cos k(x - x'_n))\} \tag{A.5}$$

We can simplify this equation further by substituting in $x'_n = \frac{(n-1)\lambda}{2}$ and noticing that $\sum_{n-1}^{2} \cos(\omega t - (n-1)\pi) = 0$ and only $\ln(\cosh ky - \cos k(x - x'_n))$ in $\{\ \}$ survives, thus

$$\Phi(x,y) = \frac{-Q}{4\pi\epsilon_0} \cos\omega t \ln \frac{\cosh ky + \cos kx}{\cosh ky - \cos kx} \tag{A.6}$$

Since $\vec{E} = -\nabla\Phi$, we obtained Eq. (4.2) and Eq. (4.2).

A.2 Floquet Stability Program

```
import numpy
import matplotlib as mpl
import os
from scipy.integrate import odeint


class One_Particle_Ensble_Sin1D(object):
    def __init__(self,A,beta,dt):
        self.A = A
        print('self.A is: ' + str(self.A))
        self.beta = beta
        print('self.beta is: '+str(self.beta))
        self.num_cell = 1.0
        # d here is the length of the system
```

```
15          self.d = self.num_cell*2.0*np.pi
16          print('slef.d: ' +str(self.d))
17          # right now "As" is only different from "A"
18          # because of different particle "densities". The reason I
19          # have stated it like this is because particles with
20          # different charges would then need the qq
21          # factor to actually be q[i]*q[j].
22          self.As = A
23          self.dt = dt
24          self.sol = np.array([])
25
26      # Define a function that grabs the matrix elements of the Jacobian,
27      # set_sol must have already
28      # been done for this to work
29      def set_sol(self,sol):
30          self.sol=sol
31          # To get the solution at a particular time we need the index
32          # that is associated with that
33          # time. We get this by taking the time value wanted and
34          # dividing by dt. In order for this to work
35          # with single (non array values) of time we need a self.dt.
36
37      # The Jacobian
38      def J(self,which_M,t):
39          x1 = self.sol[int(t/self.dt)-1,2]
40          y =  self.sol[int(t/self.dt)-1,3]
41          # define the matrix elements of the time dependent Jacobian
42          M11 = 0.0
43          M12 = 1.0
44          M21 = self.A*np.cos(x1)*np.cos(t)
45          M22 = -self.beta
46
47          if (which_M == "M11"):
48              return M11
49          if (which_M == "M12"):
50              return M12
51          if (which_M == "M21"):
52              return M21
53          if (which_M == "M22"):
54              return M22
55
56      def mw(self,warr,t):
57          dotW11 = warr[2]
58          dotW12 = warr[3]
59          dotW21 = warr[0]*self.J("M21",t)+warr[2]*(-self.beta)
60          dotW22 = warr[1]*self.J("M21",t)+warr[3]*(-self.beta)
61          return [dotW11,dotW12,dotW21,dotW22]
62
```

```
63      # The first order system of equations
64      def f(self,xarr,t):
65          x0dot = self.A*np.sin(xarr[2])*np.cos(t) - self.beta*xarr[0]
66          x1dot = 0.0
67          x2dot = xarr[0]
68          x3dot = 0.0
69          return [x0dot,x1dot,x2dot,x3dot]
70
71  def not_close(first_pnt,curnt_pnt,thresh):
72      """
73      This functions looks to see weather or not the
74      current point is in the threshold radius of the first
75      point. Returns True if NOT in threshold radius.
76      Returns False if we found our guy.
77      """
78      rf = np.array([first_pnt[0] , first_pnt[2]])
79      rs = np.array([curnt_pnt[0] , curnt_pnt[2]])
80      diff = rf-rs
81      r = np.sqrt(diff[0]**2+diff[1]**2)
82      #print("r is: "+str(r))
83
84      if (r>thresh):
85          return True
86      else:
87          return False
88
89
90  def find_one_full_closed(sol,thresh,dt):
91      """
92       This function finds a single loop of the limit cycle.
93       Since the limit cycle might be periodic over more than
94       one period this function returns the solution of
95       just that loop AND the periodicity of the loop.
96       Must pass it the threshold value. If it cant find a
97       trajectory where the beginning and end of the
98       lie within this threshold value than it quits and prints an error.
99       The threshold number "thresh" is a distance in the phase plane.
100     """
101     not_found = False
102     # Work our way backwards from last time value to find last period
103
104     # First find last mod 2*pi position.
105     loc = len(sol[:,2])
106     while ((loc*dt)%(2*np.pi)>dt):
107         loc-=1
108     first_loc = loc
109     first_pnt = sol[first_loc,:]
110     loc-=1
```

```
111     # Now find the next point where the orbit closes (going backward).
112     # Orbits should have trajectories in multiples of 2*pi so only check those
113     while ((loc*dt)%(2*np.pi)>dt):
114         loc-=1
115 
116     currnt_pnt = sol[loc,:]
117 
118     # for "slow" trajectories the point after the first may be within the
119     # threshold value. This is not bad as it means the time step is
120     # definitely small enough, but is messes up the next loop.
121     # To fix this problem we will subtract more than one from the
122     # "loc" variable. Not to much though, otherwise we risk crossing
123     # some 2*pi barrier...probably not, but be safe. The original
124     # "loc-=1" is commented out for comparison.
125     # loc -= 1
126     # Increase by pi/4 to avoid finding a close point it
127     # time that is in threshold value.
128     loc -= int(np.pi/4.0/dt)
129     while (not_close(first_pnt,currnt_pnt,thresh)):
130         if (loc == 0):
131             not_found = True
132             raise Exception("Point in threshold not found!!")
133             #break
134         while ((loc*dt)%(2*np.pi)>dt):
135             loc-=1
136         currnt_pnt = sol[loc,:]
137         secnd_loc = loc
138         loc-=1
139 
140     secnd_pnt = currnt_pnt
141 
142     if not_found:
143         final = find_one_full_closed(sol,thresh*2,dt)
144     else:
145         final = sol[secnd_loc:first_loc+1,:]
146 
147     return final
148 
149 def main():
150     # Set this to true if you want an image of the loops in 3D for different
151     # values of the varied parameter.
152     loops = False
153     # Set this to true if you want to make a movie of the stability
154     # multipliers in the complex plane?
155     mk_stab_mov = True
156 
157     # Are we looking for the first bifurcation?
158     first_bif_only = True
```

```
159
160     if loops:
161         fig3d = mpl.figure
162         d3ax = fig.add_subplot(111,projection='3d')
163
164     # Make the directory that will store the loop images.
165     os.mkdir('LoopImgs')
166     # Make a directory for the stability multiplier images
167     # --> this will be a movie as a function of A.
168     if mk_stab_mov: os.mkdir('StabMovie')
169
170     # This variable is required so we don't print the A value of
171     # the bifurcation point more than once.
172     found_bif = False
173
174     # Make a file to store q (periodicity) for different parameter values.
175     q_file = open("qdata.txt","w")
176     # Make a file to store stability multipliers for different parameter values.
177     eig_file  = open("data.txt","w")
178     eig_file.write("eig1   eig2   A\n")
179
180     # Time step size. In actuality odeint uses many more time steps but
181     # only returns information in increments of dt.
182     dt = .001
183     # Total number of iterations to perform
184     totIter = 50000
185     totTime = totIter*dt
186     time = np.arange(0.0,totTime,dt)
187
188     beta = .6
189
190     # Whats the periodicity of the system.
191     # x = n*pi/k (n must be an even number). modNum = 2*np.pi/k
192     modNum = 2.0*np.pi
193
194     # initial conditions
195     initx = np.pi
196     inity = 0.0
197     initvx = 0.0
198     initvy = 0.0
199
200     # Initial driving amplitude.
201     A_start = 0.2
202     A = A_start
203     # Final driving amplitude.
204     A_max = .9
205     # Increment to increase driving amplitude in.
206     A_step = .002
```

```
207
208     count = 0
209
210     # Make arrays to keep eigenvalues.
211     # There will be two eigenvalues so lets have two separate
212     # arrays for them
213     eigs1 = np.array([])
214     eigs2 = np.array([])
215
216     # Make the file to write final positions of the particle to
217     final = open("final_position.txt","w")
218     final.write("Last position of orbit,   A\n")
219     x0 = np.array([initvx,initvy,initx,inity])
220
221     # Keep track of the previous period of the trajectory so we can compare
222     # and find when the bifurcation occurs.
223     previous_q = 0.0
224     while A < A_max:
225         # Initial conditions vector is x0.
226         # Remember the set up is: [xdot,ydot,x,y]
227
228         apx = One_Particle_Ensble_Sin1D(A,beta,dt)
229         # Find the numerical solution for the setup "apx", initial conditions "x0",
230         # and time array, "time".
231         sol = odeint(apx.f,x0,time)
232         print("x0")
233         print(x0)
234
235         # Impose periodic boundary conditions.
236         sol[:,2]=sol[:,2]%(2*np.pi)
237
238         # "thresh" is distance in the phase place,
239         # specifically the size of a circle that we look in to
240         # determine if a periodic trajectory has gone a full cycle.
241         thresh = .00005
242
243         # Changes depending on whether or not you are looking
244         # for the first bifurcation at x=pi or
245         # other ones. x=pi bifurcation is special
246         # because it is exact and stationary in time.
247         if first_bif_only:
248             loop = np.zeros([int(2.0*np.pi/dt),4])
249         else:
250             loop = find_one_full_closed(sol,thresh,dt)
251
252         loop[:,2]+=np.pi
253
254         if "stop" in loop:
```

```
255             break
256
257         loop_t = np.arange(0.0,(len(loop))*dt,dt)
258
259         if loops :
260             d3ax.plot(np.zeros(len(loop))+A,loop[:,2],loop[:,0],color="Black")
261
262         fig = mpl.figure()
263         ax = fig.add_subplot(111)
264         #ax.scatter([0.0,np.pi,2.0*np.pi],[0.0,0.0,0.0],color="Red")
265         #ax.plot(loop[:,2],loop[:,0],":",color="Black")
266         ax.plot(loop[:,2],loop[:,0],color="Black")
267         ax.set_xlabel("$x_1$",fontsize=25)
268         ax.set_ylabel("$x_2$",fontsize=25)
269         #ax.set_xlim([np.pi-np.pi/3.0,np.pi+np.pi/3.0])
270         #ax.set_ylim([-.3,.3])
271         fig.tight_layout()
272         fig.savefig("LoopImgs/"+str(A)+".png",dpi = 300,transparent=True)
273         #os.system("open LoopImgs/" +str(A)+".png")
274         mpl.close(fig)
275
276         apx.set_sol(loop)
277
278         apx.set_sol(loop)
279
280         # Solution matrix at t=0 (identity matrix).
281         w0 = np.array([1.0,0.0,0.0,1.0])
282         # Integrate to find the linearized map
283         w_of_t = odeint(apx.mw,w0,loop_t,hmax=dt,hmin=dt)
284         #w_of_t = odeint(apx.mw,w0,loop_t)
285
286         # Periodicity of the current limit cycle.
287         current_q = loop_t[-1]/(2.0*np.pi)
288         # Print the period of the orbit we are working on
289         print("q: " + str(current_q))
290         q_file.write(str(loop_t[-1]/(2.0*np.pi))+" "+str(A)+"\n")
291
292         # If the period has changed print the best
293         # guess of the value of A for which it occured
294         if current_q > (previous_q+1.0):
295             print("bifurcation point. A = " +str(A))
296
297         # reset the previous period for a new comparison.
298         previous_q=current_q
299
300         # make the matrix form of w_of_t
301         matrix = w_of_t[-1,:].reshape(2,2)
302
```

```
303         # use linalg to get the eigenvalues of the
304         # W(t=q) (solution matrix at the end of the
305         # trajectories cycle) where q is the period time of the orbit
306         vals,vect = numpy.linalg.eig(matrix)
307 
308         if((abs(vals[0])<=1.0) and (not found_bif)):
309             print("this is the bifurcation point (l1)")
310             print(A)
311             found_bif = True
312         if(abs(vals[1])<=1.0 and (not found_bif)):
313             print("this is the bifurcation point (l2)")
314             print(A)
315             found_bif = True
316 
317         eigs1 = np.append(eigs1,vals[0])
318         eigs2 = np.append(eigs2,vals[1])
319 
320         eig_file.write(str(vals[0])+" "+str(vals[1])+" "+str(A)+"\n")
321 
322         # Update everything for next run.
323         count+=1
324         x0 = loop[-1,:]
325         final.write(str(x0)[1:-1]+" "+str(A) +"\n")
326         A += A_step
327         print("A: "+str(A))
328 
329     # Arrays for plots
330     theta = np.arange(0,10,.05)
331     A_arr = np.arange(A_start,A,A_step)
332 
333     print('we are above')
334     while len(A_arr)>len([k.real for k in eigs1]):
335         A_arr = A_arr[:-1]
336     while len(A_arr)<len([k.real for k in eigs1]):
337         A_arr = np.append(A_arr,A_arr[-1]+A_step)
338     print('we are below')
339 
340     fig1 = mpl.figure()
341     ax1 = fig1.add_subplot(111)
342     ax1.plot(np.cos(theta),np.sin(theta))
343     ax1.plot([k.real for k in eigs1],[l.imag for l in eigs1])
344     ax1.set_xlabel("Re[$\lambda_1$]",fontsize=25)
345     ax1.set_ylabel("Im[$\lambda_1$]",fontsize=25)
346     fig1.tight_layout()
347     fig1.savefig("eig1.png")
348     os.system("open eig1.png")
349 
350     fig2 = mpl.figure()
```

```
351     ax2 = fig2.add_subplot(111)
352     ax2.plot(np.cos(theta),np.sin(theta))
353     ax2.plot([k.real for k in eigs2],[l.imag for l in eigs2])
354     ax2.set_xlabel("Re[$\lambda_2$]",fontsize=25)
355     ax2.set_ylabel("Im[$\lambda_2$]",fontsize=25)
356     fig2.tight_layout()
357     fig2.savefig("eig2.png")
358     os.system("open eig2.png")
359 
360     fig3, ax3 = mpl.subplots(2,sharex=True)
361     ax3[0].plot(A_arr,[k.real for k in eigs1],color='k')
362     ax3[1].plot(A_arr,[k.imag for k in eigs1],color='k')
363     ax3[0].set_ylabel("Re[$\lambda_1$]",fontsize = 25)
364     ax3[1].set_ylabel("Im[$\lambda_1$]",fontsize = 25)
365     ax3[1].set_xlabel("$A$",fontsize = 25)
366     fig3.tight_layout()
367     fig3.savefig("A_vs_eig1.png")
368     os.system("open A_vs_eig1.png")
369 
370     fig4, ax4 = mpl.subplots(2,sharex=True)
371     ax4[0].plot(A_arr,[k.real for k in eigs2], color = 'k')
372     ax4[1].plot(A_arr,[k.imag for k in eigs2], color = 'k')
373     ax4[0].set_ylabel("Re[$\lambda_2$]",fontsize = 25)
374     ax4[1].set_ylabel("Im[$\lambda_2$]",fontsize = 25)
375     ax4[1].set_xlabel("$A$",fontsize = 25)
376     fig4.tight_layout()
377     fig4.savefig("A_vs_eig2.png")
378     os.system("open A_vs_eig2.png")
379 
380     eig_file.close()
381 
382     final.close()
383 
384     # Uncomment this if you want a text file with the
385     # information of the system you just did a run
386     # of.
387     ## make text file with all extra information
388     #outFile = open("info.dat","w")
389     #outFile.write("Info \n coefficient: " + str(coef) \
390     #        + "\nwave number: " +str(k)\
391     #        + "\nomega: " + str(w)\
392     #        + "\ndamping: " + str(damp)\
393     #        + "\ng: " + str(g)\
394     #        + "\ntime step: " + str(dt)\
395     #        + "\ntotal time: " + str(dt*totIter)\
396     #        + "\ntotal iterations: " + str(totIter)\
397     #        + "\nInitial Conditions: \n" +
398     #        "initial x: " +str(initx) \
```

```
399     #        +"\ninitial y: " +str(inity) \
400     #        +"\ninitial vx: " +str(initvx)\
401     #        +"\ninitial vy: " +str(initvy) )
402     #outFile.close()
403
404
405     if loops:
406         line = np.arange(start_A-.01,start_A,A_step)
407         pi_line = np.zeros(len(line))+np.pi
408         z_line = np.zeros(len(line))
409         d3ax.plot(line,pi_line,z_line,color="Black")
410         d3ax.set_xlabel("$A$",fontsize=25)
411         d3ax.set_ylabel("$x_1$",fontsize=25)
412         d3ax.set_zlabel("$x_2$",fontsize=25)
413         d3fig.tight_layout()
414         d3fig.savefig("loops.png",dpi=300)
415
416     if mk_stab_mov:
417         for i in range(len(eigs1)):
418             s_fig = mpl.figure()
419             s_ax = s_fig.add_subplot(111)
420             s_ax.plot(np.cos(theta),np.sin(theta))
421             s_ax.scatter(eigs1[i].real,eigs1[i].imag,c='r',s=20)
422             s_ax.scatter(eigs2[i].real,eigs2[i].imag,c='b',s=20)
423             s_ax.set_xlabel("Re[$\lambda$]",fontsize=25)
424             s_ax.set_ylabel("Im[$\lambda$]",fontsize=25)
425             s_fig.tight_layout()
426             s_fig.savefig("%(num)0.5d_stbl.png"%{"num":i})
427             mpl.close(s_fig)
428
429
430
431 if __name__ == '__main__':
432     main()
```

Bibliography

[1] T. Simpson, J. Liu, and A. Gavrielides. Period-doubling cascades and chaos in a semiconductor laser with optical injection. *Physical Review A*, 51(5):4181–4185, 1995.

[2] P. Olbrich, J. Karch, E. L. Ivchenko, J. Kamann, B. MĂ¤rz, M. Fehrenbacher, D. Weiss, and S. D. Ganichev. Classical ratchet effects in heterostructures with a lateral periodic potential. *Physical Review B*, 83(16):165320, 2011.

[3] N. Francois, H. Xia, H. Punzmann, and M. Shats. Inverse energy cascade and emergence of large coherent vortices in turbulence driven by faraday waves. *Physical Review Letters*, 110:194501, 2013.

[4] P. Denissenko, G. Falkovich, and S. Lukaschuk. How waves affect the distribution of particles that float on a liquid surface. *Physical Review Letters*, 97:244501, 2006.

[5] G. Falkovich, A. Weinberg, P. Denissenko, and S. Lukaschuk. Floater clustering in a standing wave. *Nature: Brief Communications*, 435:1045, 2005.

[6] Erez Boukobza, Michael G. Moore, Doron Cohen, and Amichay Vardi. Nonlinear phase dynamics in a driven bosonic josephson junction. *physical review letters*, 104:240402, 2010.

[7] Iwo Bialynicki-Birula, Maciej Kaliński, and J. H. Eberly. Lagrange equilibrium points in celestial mechanics and nonspreading wave packets for strongly driven rydberg electrons. *Phys. Rev. Lett.*, 73:1777–1780, Sep 1994.

[8] J. H. Eberly and K. C. Kulander. Atomic stabilization by super-intense lasers. *Science*, 262(5137):1229–1233, 1993.

[9] M. Pont and M. Gavrila. Stabilization of atomic hydrogen in superintense, high-

frequency laser fields of circular polarization. *Phys. Rev. Lett.*, 65:2362–2365, Nov 1990.

[10] Jakub Zakrzewski, Dominique Delande, and Andreas Buchleitner. Nonspreading electronic wave packets and conductance fluctuations. *Phys. Rev. Lett.*, 75:4015–4018, Nov 1995.

[11] P. Bak, C. Tang, and K. Wisenfeld. Self-organized criticality: An explanation of 1/f noise. *Physics Review Letters*, 59:381, 1987.

[12] P. Bak, K. Chen, and M. Creutz. Self-organized criticality in the game of life. *Nature*, 342:780, 1989.

[13] Erik Andreas Martens, Shashi Thutupalli, Antoine Fourriere, and Oskar Hallatchek. Chimera states in mechanical oscillator networks. *Proceedings of the National Academy of Sciences of the United States of America*, 110(26):10563–10567, 2013.

[14] Mikhail I. Rabinovich, Pablo Varona, Allen I. Selverston, and Henry D. I. Abarbanel. Dynamical principles in neuroscience. *Rev. Mod. Phys.*, 78:1213–1265, Nov 2006.

[15] A. J. Rimberg, T. R. Ho, Ç. Kurdak, John Clarke, K. L. Campman, and A. C. Gossard. Dissipation-driven superconductor-insulator transition in a two-dimensional josephson-junction array. *Phys. Rev. Lett.*, 78:2632–2635, Mar 1997.

[16] R Mankowsky, A Subedi, M Forst, S O Mariager, M Chollet, H T Lemke, J S Robinson, J M Glownia, M P Minitti, A Frano, M Fechner, N A Spaldin, T Loew, B Keimer, A Georges, and A Cavalleri. Nonlinear lattice dynamics as a basis for enhanced superconductivity in YBa2Cu3O6.5 . *Nature*, 516(7529):71–73, December 2014.

[17] Marin Bukov, Luca D'Alessio, and Anatoli Polkovnikov. Universal High-Frequency Behavior of Periodically Driven Systems: from Dynamical Stabilization to Floquet Engineering. *arXiv*, page 35, July 2014.

[18] S Inouye, MR Andrews, and J Stenger. Observation of feshbach resonances in a bose-einstein condensate. *Nature*, 392(March):151–154, 1998.

[19] D O'dell, S Giovanazzi, G Kurizki, and VM Akulin. Bose-Einstein Condensates with 1/r Interatomic Attraction : Electromagnetically Induced "Gravity". *Physical Review Letters*, pages 5687–5690, 2000.

[20] Peter Leonidovich Kapitza. Dynamical stability of a pendulum when its point of suspension vibrates. *Zhurnal Eksperimental'noi i Teoreticheskoi Fiziki*, 21:588, 1951.

[21] Peter Leonidovich Kapitza. Pendulum with a vibrating suspension. *Uspekhi Fizicheskikh Nauk*, 44:7, 1951.

[22] Wolfgang Paul. Electromagnetic traps for charged and neutral particles. *Rev. Mod. Phys.*, 62:531–540, Jul 1990.

[23] M.K. Mazumder, R. Sharma, A.S. Biris, J. Zhang, C. Calle, and M. Zahn. Self-cleaning transparent dust shields for protecting solar panels and other devices. *Particulate Science and Technology*, 25:5–20, May 2007.

[24] S. Lefschetx. *Differential Equations Geometric Theory*. Dover Publications, New York, second edition, 1977.

[25] N. W. McLachlan. *Theory and Application of Mathieu Functions*. Oxford University Press, London, first edition, 1947.

[26] T. Pradhan and A. V. Khare. Plane pendulum in quantum mechanics. *American Journal of Physics*, 41:59–66, 1973.

[27] D. Leibfried, R. Blatt, C. Monroe, and D. Wineland. Quantum dynamics of single trapped ions. *Reviews of Modern Physics*, 75:282–322, 2003.

[28] L. Ruby. Applications of the mathieu equation. *American Journal of Physics*, 64(1):39–44, 1996.

[29] Emile Mathieu. MĂŠmoire sur le mouvement vibratoire d'une membrane de forme elliptique. *Journal de MathĂŠmatiques Pures et AppliquĂŠes*, pages 137–203, 1868.

[30] J. Gutiérrez-Vega, S. Chávez-Cerda, and Ramón Rodríguez-Dagnino. Free oscillations in an elliptic membrane. *Revista Mexicana de Fisica*, 45:613–622, 1999.

[31] S. Blanes, F. Casas, J.a. Oteo, and J. Ros. The Magnus expansion and some of its applications. *Physics Reports*, 470(5-6):151–238, January 2009.

[32] Luca DÁlessio and Anatoli Polkovnikov. Many-body energy localization transition in periodically driven systems. *Annals of Physics*, 333:19–33, 2013.

[33] Anatoli Polkovnikov. Phase space representation of quantum dynamics. *Annals of Physics*, 325(8):1790–1852, 2010.

[34] Anatoli Polkovnikov. Quantum ergodicity fundamentals and applications. 2013.

[35] Robert Gilmore and Marc Lefranc. *The Topology of Chaos*. Wiley, 2002.

[36] J. Thompson and H. Stewart. *Nonlinear Dynamics and Chaos*. Wiley, New York, second edition, 2002.

[37] J. Guckenheimer. *Nonlinear Oscillations, Dynamical Systems, and Bifurcations of Vector Fields*. Springer-Verlag, New York, 1983.

[38] Thierry Dauxois, Stefano Ruffo, Ennio Arimondo, and Martin Wilkens. Dynamics and thermodynamics of systems with long-range interactions: An introduction. In Thierry Dauxois, Stefano Ruffo, Ennio Arimondo, and Martin Wilkens, editors, *Dynamics and Thermodynamics of Systems with Long-Range Interactions*, volume 602 of *Lecture Notes in Physics*, pages 1–19. Springer Berlin Heidelberg, 2002.

[39] M. Kac, G. E. Uhlenbeck, and P. C. Hemmer. On the van der waals theory of the vapor-liquid equilibrium. i. discussion of a one-dimensional model. *Journal of Mathematical Physics*, 4(2):216–228, 1963.

[40] Clément Sire and Pierre-Henri Chavanis. Thermodynamics and collapse of self-gravitating Brownian particles in D dimensions. *Physical Review E*, 66(4):046133, October 2002.

[41] Andrea Antoniazzi, Duccio Fanelli, Julien Barré, Pierre-Henri Chavanis, Thierry Dauxois, and Stefano Ruffo. Maximum entropy principle explains quasistationary states in systems with long-range interactions: The example of the Hamiltonian mean-field model. *Physical Review E*, 75(1):011112, January 2007.

[42] Mickael Antoni and Stefano Ruffo. Clustering and relaxation in hamiltonian long-range dynamics. *Physical Review E*, 52(3), 1995.

[43] Mark Kac. On the partition function of a one-dimensional gas. *Physics of Fluids (1958-1988)*, 2(1):8–12, 1959.

[44] Tarcísio N. Teles, Fernanda P. Da C. Benetti, Renato Pakter, and Yan Levin. Nonequilibrium Phase Transitions in Systems with Long-Range Interactions. *Physical Review Letters*, 109(23):230601, December 2012.

[45] Yan Levin, Renato Pakter, Felipe B. Rizzato, TarcĂsio N. Teles, and Fernanda P.C. Benetti. Nonequilibrium statistical mechanics of systems with long-range interactions. *Physics Reports*, 535(1):1 – 60, 2014. Nonequilibrium statistical mechanics of systems with long-range interactions.

[46] P. H. Chavanis. Phase Transitions in Self-Gravitating Systems. *International Journal of Modern Physics B*, 20(22):3113–3198, September 2006.

[47] R. Bachelard, T. Dauxois, G. De Ninno, S. Ruffo, and F. Staniscia. Vlasov equation for long-range interactions on a lattice. *Physical Review E*, 83(6):061132, June 2011.

[48] Julien BarrĂŠ, Thierry Dauxois, and Stefano Ruffo. Clustering in a model with repulsive long-range interactions. *Physica A: Statistical Mechanics and its Applications*, 295(1):254–260, 2001. Proceedings of the IUPAP International Conference on New Trends in the Fractal Aspects of Complex Systems.

[49] Michael Joyce, Jules Morand, François Sicard, and Pascal Viot. Scaling Quasistationary States in Long-Range Systems with Dissipation. *Physical Review Letters*, 112(7):070602, February 2014.

[50] T. N. Teles, Y. Levin, and R. Pakter. Statistical mechanics of 1D self-gravitating systems: the core-halo distribution. *Monthly Notices of the Royal Astronomical Society: Letters*, 417(1):L21–L25, October 2011.

[51] Fred W. Schmidlin. A new non-levitated mode of traveling wave toner transport. *IEEE Transactions on Industry Applications*, 27:480–487, 1991.

[52] Senichi Masuda. Booth for electrostatic powder painting with contact type electric field curtain, April 1974.

[53] Senichi Masuda, Masao Washizu, and Ichiro Kawabata. Movement of blood cells in liquid by nonuniform traveling field. *IEEE Transactions on Industry Applications*, 24:217–222, Mar/Apr 1988.

[54] Louis C. Weiss and Devron P. Thibodeaux. Separation of seed by-products by and ac electric field. *JAOCS*, 61(5):886–890, May 1984.

[55] Fred W. Schmidlin. Dovelopment apparatus, March 1987.

[56] H. Kawamoto. Some techniques on electrostatic separation of particle size ustilizing electrostatic traveling-wave field. *Journal of Electrostatics*, 66:220–228, 2008.

[57] H. Kawamoto, K. Seki, and N. Kuromiya. Mechanism of travelling-wave transport of particles. *Journal of Physics D: Applied Physics*, 39:1249–1256, 2006.

[58] G. Liu and J.S. Marshall. Effect of particle adhesion and interactions on motion by traveling waves on an electric curtain. *Journal of Electrostatics*, 68:179–189, 2010.

[59] G. Liu and J. Marshall. Particle transport by standing waves on an electric curtain. *Journal of Electrostatics*, 68:289–298, 2010.

[60] Zygmunt Dudzicz. Recording of dust particle oscillation path inside electric curtain by laser diode apparatus. *Optica Applicata*, 35:907–912, 2005.

[61] Fred W. Schmidlin. Modes of traveling wave particle transport and their applications. *Journal of Electrostatics*, 34:225–244, 1995.

[62] James M. Hemstreet. Velocity distribution on the masuda panel. *Journal of Electrostatics*, 17:245–254, 1985.

[63] James M. Hemstreet. Three-phase velocity distribution of lycopodium particles on the masuda panel. *Journal of Electrostatics*, 27:237–247, Mar 1991.

[64] Jennifer Chesnutt and Jeffrey Marshall. Simulation of particle separation on an inclined electric curtain. *IEEE Transactions on Industry Applications*, 49(3):1104–1112, 2013.

[65] C. I. Calle, J. L. McFall, C. R. Buhler, S. J. Snyder, E. E. Arens, A. Chen, M. L.

Ritz, J. S. Clements, C. R. Fortier, and S. Trigwell. Dust particle removal by electrostatic and dielectrophoretic forces with applications to NASA exploration missions. *Proceedings ESA Annual Meeting on Electrostatics*, pages 1–14, 2008.

[66] B. L. Schrunk, D. G.and Sharpe, B. L. Cooper, and M. Thangavelu. *The moon: resources, future, development and colonization*. Praxis Publishing Ltd. Chichester, 1999.

[67] Yanzhen Zhang, Thomas Pähtz, Yonghong Liu, Xiaolong Wang, Rui Zhang, Yang Shen, Renjie Ji, and Baoping Cai. Electric field and humidity trigger contact electrification. *Phys. Rev. X*, 5:011002, Jan 2015.

[68] Peter Young. but were afraid to ask. 2013.

[69] P. Atten, H.L. Pang, and J.L. Reboud. Study of dust removal by standing wave electric curtain for application to solar cells on mars. *IEEE Transactions on Industry Applications*, 45:75–86, 2009.

[70] R.A. Sims, A.S. Biris, J.D. Wilson, C.U. Yurteri, M.K. Mazumder, C.I. Calle, and C.R. Buhler. Development of a transparent self-cleaning dust shield for solar panels. *Proceedings ESA-IEEE Joint Meeting on Electrostatics*, page 814, 2003.

[71] Senichi Masuda and Tsutomu Kamimura. Approximate methods for calculating a non-uniform travelling field. *Journal of Electrostatics*, 1:351–370, Janurary 1975.

[72] S.Y. Kim and B. Hu. Bifurcations and transitions to chaos in an inverted pendulum. *Physical Review E*, 58(3):3028–3035, 1998.

[73] E. Butikov. An improved criterion for kapitza's pendulum stability. *Journal of Physics A: Mathematical and Theoretical*, 44:295292, 2011.

[74] J Starrett and R. Tagg. Control of a chaotic parametrically driven pendulum. *Physical Review Letters*, 74(11):1974–1977, 1995.

[75] A.K. Johnson and J.A. Rabchuk. A bead on a hoop rotating about a horizontal axis: A one-dimensional ponder motive trap. *American Journal of Physics*, 77(11):1039–1048, 2009.

[76] M. Abramowitz and I. A. Stegun. *Handbook of Mathematical Functions*. Dover Publications, New York, second edition, 1965.

[77] N.V. Brillianttov and T.Poschell. Rolling as a continuing collision. *The European Physical Journal B*, 12:299–301, 1999.

[78] P. Morse and K. Feshbach. *Methods of Theoretical Physics*. McGraw-Hill Book Company, New York, 1953.

[79] H. Gunderson, H. Rigas, and F. S. VanVleck. A technique for determining stability regions for the damped mathieu equation. *SIAM Journal of Applied Mathematics*, 26(2):345–349, March 1974.

[80] J. Wu and W. L. Nyborg. Ultrasound, cavitation bubbles and their interaction with cells, invited review paper. *Advanced Drug Delivery Reviews*, 60:1103–1116, 2008.

[81] K. T. Alligood, T. D. Sauer, and J. A. Yorke. *Chaos - an introduction to dynamical systems*. Springer, New York, 1996.

[82] Zygmunt Dudzicz. Electrodynamics of charged dust particles and repulsion force within plane-type electric curtain. *Journal of Electrostatics*, 51-52:111–116, 2001.

[83] S. Masuda, K. Fujibayashi, K. Ishida, and H. Inaba. Confinement and transportation of charged aerosol clouds via electric curtain. *Electrical Engineering in Japan*, 92:43, 1972.

[84] C. I. Calle, M. K. Mazumder, C. D. Immer, C. R. Buhler, J. S. Clements, P. Lundeen, A. Chen, and J.G. Mantovani. Controlled particle removal from surfaces by electrodynamic methods for terrestrial, lunar and martian environmental conditions. *Journal of Physics: Conference Series*, 142:012073, 2008.

[85] John Starrett and Randall Tagg. Control of a chaotic parametrically driven pendulum. *Physical Review Letters*, 74(11):1974–1977, 1994.

[86] R. Chacon and L. Marcheggiani. Controlling spatiotemporal chaos in chains of dissipative kapitza pendula. *Physical Review E*, 82:016201, 2010.

[87] Dario Maravall, Changjiu Zhou, and Javier Alonso. Hybrid fuzzy control of the inverted pendulum via vertical forces. *International Journal of Intelligent Systems*, 20(2):195–211, 2005.

[88] James A. Blackburn. Stability and hopf bifurcations in an inverted pendulum. *American Journal of Physics*, 60:903, 1992.

[89] W. Szemplinska-Stupnicka, E. Tyrkiel, and A. Zubrzycki. The global bifurcations that lead to transient tumbling chaos in a parametrically driven pendulum. *International Journal of Bifurcation and Chaos*, 10(9):2161–2175, 2000.

[90] M. V. Bartuccelli, G. Gentile, and K. V. Georgiou. On the dynamics of a vertically driven damped planar pendulum. *The Royal Society*, 457(2016):3007–3022, 2001.

[91] Eugene Butikov. Subharmonic resonances of the parametrically driven pendulum. *Journal of Physics A: Mathematical and General*, 35(30):6209, 2002.

[92] R. W. Leven and B. P. Koch. Chaotic behaviour of a parametrically excited damped pendulum. *Physics Letters*, 86A(2):71, 1981.

[93] G. Liu and J. Marshall. Particle transport by standing waves on an electric curtain. *Journal of Electrostatics*, 68:289–298, 2010.

[94] J.K.R Chesnutt and J. S. Marshall. Simulation of particle separation on an inclined electric curtain. *IEEE Transactions on Industry Applications*, 49(3):1104–1112, 2013.

[95] J. S. Marshall. Particle clustering in periodically forced straining flows. *Journal of Fluid Mechanics*, 624:69, March 2009.

[96] Paul Gibbon and Godehard Sutmann. Long-range interactions in many-particle simulation. *Quantum Simulations of Complex Many-Body Systems: From Theory to Alogorithms*, 10:467–506, 2002.

[97] Marten Scheffer, Jordi Bascompte, William A. Brock, Victor Brovkin, Stephen R. Carpenter, Vasilis Dakos, Hermann Held, Egbert H. Van Nes, Max Rietkerk, and George Sugihara. Early-warning signals for critical transitions. *Nature*, 461(7260):53–59, 2009.

[98] Fabio Cecconi, Fabiana Diotallevi, Umberto Marini Bettolo Marconi, and Andrea Puglisi. Fluid-like behavior of a one-dimensional granular gas. *Journal of Chemical Physics*, 120(1):35–42, Jan 2004.

[99] Sang-Yoon Kim and Bambi Hu. Critical behavior of period doublings in coupled inverted pendulums. *Phys. Rev. E*, 58:7231–7242, Dec 1998.

[100] Owen D. Myers, Junru Wu, and Jeffrey S. Marshall. Nonlinear dynamics of particles excited by an electric curtain. *Journal of Applied Physics*, 114(15):– , 2013.

[101] D. Chen and J. Wu. Dislodgement and removal of dust-particles from a surface by a technique combining acoustic standing wave and airflow. *Journal of the Acoustical Society of America*, 127:45–50, 2010.

[102] Alessandro Campa, Thierry Dauxois, and Stefano Ruffo. Statistical mechanics and dynamics of solvable models with long-range interactions. *Physics Reports*, 480(3-6):57–159, September 2009.

[103] Alessandro Campa, Andrea Giansanti, and Daniele Moroni. Canonical solution of a system of long-range interacting rotators on a lattice. *Phys. Rev. E*, 62:303–306, Jul 2000.

[104] Alessandro Campa, Andrea Giansanti, and Daniele Moroni. Canonical solution of classical magnetic models with long-range couplings. *Journal of Physics A: Mathematical and General*, 36(25):6897–6921, June 2003.

[105] Celia Anteneodo and Constantino Tsallis. Breakdown of exponential sensitivity to initial conditions: Role of the range of interactions. *Phys. Rev. Lett.*, 80:5313–5316, Jun 1998.

[106] Francisco Tamarit and Celia Anteneodo. Rotators with long-range interactions: Connection with the mean-field approximation. *Phys. Rev. Lett.*, 84:208–211, Jan 2000.

[107] A. Altland and B. Simons. *Condensed Matter Field Theory*. Cambridge University Press, 2006.

[108] G. Miritello, a. Pluchino, and a. Rapisarda. Phase transitions and chaos in long-range models of coupled oscillators. *EPL (Europhysics Letters)*, 85(1):10007,

January 2009.

[109] F Leyvraz, M-C Firpo, and S Ruffo. Inhomogeneous quasi-stationary states in a mean-field model with repulsive cosine interactions. *Journal of Physics A: Mathematical and General*, 35(20):4413, 2002.

[110] T Dauxois, P Holdsworth, and S Ruffo. Violation of ensemble equivalence in the antiferromagnetic mean-field XY model. *The European Physical Journal B- ...*, 16:659–667, 2000.

[111] Peter Walters. *An Introduction to Ergodic Theory*. Springer, New York, 1982.

[112] William Parry. *Topics in Ergodic Theory*. Cambridge University Press, New York, 1981.

[113] Rufus Bowen and David Ruelle. The ergodic theory of axiom a flows. *Inventiones math*, 29:181–202, 1975.

[114] J. Barré, F. Bouchet, T. Dauxois, and S. Ruffo. Birth and long-time stabilization of out-of-equilibrium coherent structures. *The European Physical Journal B - Condensed Matter*, 29(4):577–591, October 2002.